ON THE CIRCULATION AND FRESHWATER DYNAMICS OF THE HUDSON BAY COMPLEX

by

Natasha Ridenour

A thesis submitted in partial fulfillment of the requirements for the degree of

Doctor of Philosophy

Department of Earth and Atmospheric Sciences
University of Alberta

Abstract

The Hudson Bay Complex (HBC), which includes Hudson, James, and Ungava Bays, Foxe Basin, and Hudson Strait, is currently undergoing change from two anthropogenic sources; industry and global warming. The communities surrounding this region use the sea for travel, hunting, and social connections, year round. Changes in the food chain and ice conditions thus impact the daily lives of the locals. The HBC also has a large drainage basin, receiving about 900 km^3 of freshwater annually, making it an ideal location for the production of hydroelectricity. This riverine water traverses Hudson Bay and is advected to the North Atlantic via Hudson Strait, the main pathway for exchange between the HBC and the global ocean. Hudson Strait is also the third largest source of advected freshwater to the Labrador Sea after Fram and Davis Straits.

However, our understanding of the role of riverine water in the bay is limited, and downstream effects of changes in river discharge is presently unknown. Additionally, knowledge of circulation in areas, such as Hudson Strait, is limited to a few observational datasets. These datasets focus mostly on the southern side of the strait which contains fresh eastward flow, and while valuable, there are no recent published data for the north side of the strait containing westward flowing waters entering the bay.

I begin by presenting the first multi-year freshwater budget for the HBC. Using four model simulations and three river discharge datasets, I show that river discharge impacts freshwater fluxes out of the region on timescales longer than a year. Decreased river discharge and seasonality led to reduced freshwater and volume exchange within the HBC and to the North Atlantic. Model resolution had minimal impact on freshwater and volume fluxes in areas with simple flow dynamics. I also provide estimates of the Ekman, mean, and turbulent

components of freshwater exchange between the interior and boundary regions of the bay. The mean and Ekman components import freshwater to the interior in spring and summer, and export it in the fall. Residence times of discharge in the HBC are calculated using an offline Lagrangian passive tracer tool, with an upper limit of 32 years.

Using the highest resolution model simulation available at the time, I revisited the summer circulation pattern in Hudson Bay, which historically was thought to be cyclonic. Using satellite altimetry data along with model output, I showed that in summer, steric height gradients due to increased river discharge in summer, generate small scale features, including anticyclonic geostrophic flow in eastern Hudson Bay. Given this result, I present a revised summer surface flow pattern for Hudson Bay.

Finally, to increase our understanding of flow and water exchange in Hudson Strait, I present the first year long observed measurements of flow on the northern side of Hudson Strait. Mooring data show a saline, weakly stratified inflow with reduced seasonality on the northern side compared to the southern side of the strait, which contains the fresh, discharge laden outflow. Source waters are from the Baffin Island Current, comprised mainly of Arctic water, with small contributions from Transitional Water and West Greenland Irminger Water.

Preface

Chapter 3 has been published as:

Ridenour, N.A., X. Hu, S. Jafarikhasragh, J.C. Landy, J.V. Lukovich, T.A. Stadnyk, K. Sydor, P.G. Myers, and D.G. Barber. 2019a. *Sensitivity of freshwater dynamics to ocean model resolution and river discharge forcing in the Hudson Bay Complex.* Journal of Marine Systems 196: 48–64. doi: 10.1016/j.jmarsys.2019.04.002

I did the analysis, the majority of the model evaluation, runoff remapping, writing, and ran two of the four experiments. X. Hu ran the remaining two experiments, taught and guided me how to remap the runoff, and provided assistance on some calculations. S. Jafarikhasragh provided the spatial sea surface temperature plots. Sea ice thickness data was provided by J.C. Landy along with input regarding the data. J.V. Lukovich provided the ice drift vector plots along with some writing on the plots. T.A. Stadnyk provided two HYPE river discharge datasets. P.G. Myers provided advice, guidance, and, along with K. Sydor, D.G. Barber, and all co-authors, provided manuscript edits.

Chapter 4 has been published as:

Ridenour, N.A., X. Hu, K. Sydor, P.G. Myers, and D.G. Barber. 2019b. *Revisiting the circulation of Hudson Bay: Evidence for a seasonal pattern.* Geophysical Research Letters 46: 3891–3899. doi: 10.1029/2019GL082344

I performed the analysis. X. Hu ran the simulation used in the paper. P.G. Myers provided advice, guidance, and, along with K. Sydor, D.G. Barber, and X. Hu, provided manuscript edits.

Acknowledgments

I'm not sure I would have completed this thesis without the support and guidance from my main supervisor, Dr. Paul Myers. I've been able to travel, go places I never thought I would go, and do things I never thought I would do. I've also had the opportunity to work with some amazing scientists. All of these things are because of Paul, and for that I am truly grateful.

To my co-supervisor, Dr. David Barber, who provided feedback and support throughout my project, which has taught me the value of collaboration, not only between scientists, but also between academia and industry. I have learned so much from being a part of this project.

Thank you to Dr. Fiammetta Straneo, who taught me so much about observations (almost everything I know!) during my time at Scripps. And to Jamie Holte who helped me a tonne with various analyses and detiding.

To the lab: Xianmin, Nathan, Clark, Juliana, Andrew, Charlène, Yarisbel, Laura, Laura, Inge, Alain, David, Ujjwal, Amanda, Liam, Ran, and Yiran, thank you for being the most amazing support network and friends one could ask for during all the good and bad days of research. From bouncing ideas off of each other, help with technical issues (Xianmin, Nathan, Clark), proof reading (Nathan), reviewing manuscripts with a fine toothed comb (Xianmin), and discussions of random topics to lunch breaks that we still need to get better at taking.

To my friends who kept me sane, Alison, Ian, Steve, and Rajpreet. From RuPaul nights, to cornmazes, to long distance skypes, thank you for taking my mind off school, and providing the laughs and support when I needed them the most.

To Dale and Diane, for being my family in Edmonton, providing delicious food, and for letting me hide out in the basement with internet for my defense.

Thank you to my parents for always supporting and encouraging me, even if you suggest

that I work on my thesis on Christmas day, and any other holiday or day off... To my sisters, Christine and Desirae, who don't really understand how I made it this far (or what I do), but think some of my pictures are cool...

To Marcus who was always there to listen to my frustrations and celebrate my achievements (and fall asleep during my presentations). And to Dominik and Torin, who gifted me time management (finally!), the ability to extreme multitask, and to remind me daily of the world I want them to grow up in and to lead by example in the hopes of making a difference.

Contents

List of Tables

List of Figures

Chapter 1

Introduction

1.1 The Hudson Bay Complex

The Hudson Bay Complex (HBC) is a large inland sea in eastern Canada, spanning over 20° of latitude and includes Foxe Basin, Hudson Strait and Ungava Bay, and Hudson and James Bays (Figure 1.1). The HBC is connected to the Arctic Ocean and the Canadian Arctic Archipelago via Fury and Hecla Strait in the north, and to the North Atlantic in the east via Hudson Strait. Hudson Strait is the main source of oceanic water to the HBC region, and is also one of the three main gateways where oceanic freshwater is imported into the North Atlantic, potentially impacting deep water formation in the Labrador and Nordic Seas (Aagaard and Carmack, 1989; Bamber et al., 2012; Yang et al., 2016). The freshwater from Hudson Strait is primarily riverine sourced water. The HBC is the outlet for the Hudson Bay watershed, that extends from the Rocky Mountains to Labrador, North Dakota to northern Baffin Island, and receives nearly 1000 km^3 of discharge per year (Déry et al., 2018, 2009; Holmes et al., 2012; Shiklomanov and Shiklomanov, 2003).

The HBC is under the influence of polar air masses, leading to complete ice cover in winter, and ice free summers. This feature is important to the everyday lives of the locals who live there. Along the coast, there are roughly 30,000 people who call this area home, with the communities depending both on the resupply ships as well as on traditional hunting practices and knowledge. The shipping season is limited to the ice free time of year, so in winter, when there is complete ice cover, the locals depend on landfast ice and traditional knowledge for

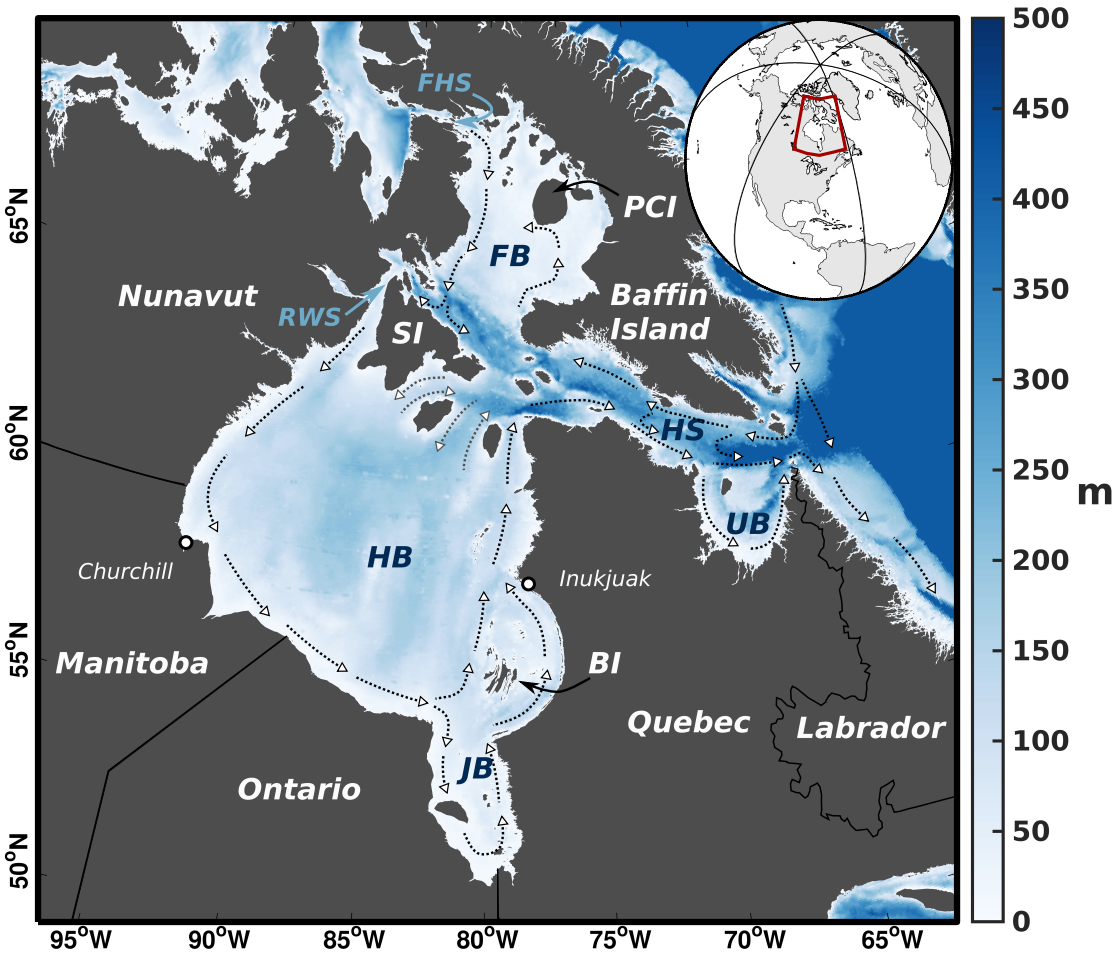

Figure 1.1: Map of the Hudson Bay Complex. Where FB, HS, UB, HB, and JB are Foxe Basin, Hudson Strait, Ungava Bay, Hudson Bay, and James Bay respectively. Finally, FHS, RWS, BI, PCI, and SI show the locations of Fury and Hecla Strait, Roes Welcome Sound, Belcher Islands, Prince Charles Island, and Southampton Island respectively. Black dotted arrows show known circulation, while grey arrows show speculated circulation. Circulation between Foxe Basin, Hudson Bay, and Hudson Strait is not shown due to lack of agreement in the available literature.

their food. However, throughout the year, the Indigenous communities depend on the Hudson Bay system not only for food, but also for maintaining cultural and social connections, as well as trade and transport (Babb et al., 2019). Climate change in this region is leading to unsafe ice conditions for on-ice travel, hunting, and watercraft, as well as changing migration routes of food sources on land (Babb et al., 2019). However, as the length of the ice free season increases, human activity is also increasing, along with the risk of marine accidents. As noted earlier, many rivers drain into the region, not only bringing their own pollution from

upstream (Gaden et al., 2019), but also attracting the hydroelectric industry. The impacts of this industry on the region are still unknown, as the volume of river water flowing into the ocean is modified temporally and spatially.

1.2 Anthropogenic Impacts

Presently, nearly half of the river discharge entering Hudson Bay is regulated (Déry et al., 2018). Regulation modifies the seasonal cycle of the river, increasing discharge in the winter, when electricity demands are higher, and reducing the flow in summer (Déry et al., 2018). These developments tend to decrease the variability seen in the river's seasonal cycle. For naturally flowing rivers, flow is low between January and April. Once snow begins to melt in mid-April, river flow increases dramatically (also called the spring freshet), with a maximum flow rate in May. The flow rate slowly decreases to winter values over the summer and fall. Regulated rivers, on the other hand, have smaller spring freshets, lower flow rates in the summer, and higher flow rates in the winter due to larger demands for electricity (Déry et al., 2011). Additionally, some rivers have been diverted to larger rivers with hydroelectric facilities, changing the spatial distribution of river discharge around the HBC as well.

Given these changes in river discharge, one might ask "how does this impact the ocean?". Few studies have looked into this question, with one study finding an increase in sea ice concentration and thickness when rivers are regulated (Saucier and Dionne, 1998), while another study found very little change in sea ice or freshwater storage, but noted increased river discharge meant increased fluxes leaving the region (Brown et al., 2019). Neither study investigated changes in circulation within their respective regions. And while both studies focused on regional scales, changes on smaller scales (meters to kilometers) have so far been overlooked, but noted by local Inuit on the Belcher Islands (Heath and Sanikiluaq, 2014).

However, the hydroelectric industry is not the only anthropogenic impact on river discharge or on the HBC. Increasing air temperatures due to global warming are also expected to lead to an intensified hydrological cycle as well as earlier spring freshets (Déry et al., 2011; Zhang et al., 2012). Since 1964, there has been no significant trend in discharge, due to the decreasing trend from 1964–1988, and increasing trend from 1989–2013 (Déry et al., 2016).

The driving mechanisms behind this variability are presently unknown (Déry et al., 2009). However, since the 1990s, the total Canadian discharge has increased by 18% (Déry et al., 2016). Speculation suggests this is due to a number of factors, including the negative Arctic Oscillation and increased moisture transport towards the poles (Déry et al., 2018). Model studies have projected an increase in HBC streamflow with a global temperature increase of 1.5°C, however, temperature increases beyond that, even 2.0°C, indicate that in summer, streamflow decreases due to higher evaporation rates and lower precipitation (MacDonald et al., 2018). Present day monitoring must continue in order to determine changes occurring in Canadian rivers, as too many factors make it difficult to determine what is leading to the current increase in river discharge that is being observed (Déry et al., 2016).

Increased air temperatures in the HBC region also have been shown to increase the length of the ice free season, directly impacting the locals as well as the shipping industry. The ice free season has increased about 3 weeks in Hudson Bay, breaking up 2 weeks earlier and freezing up 1 week later (Castro de la Guardia et al., 2017; Gagnon and Gough, 2005; Galbraith and Larouche, 2011; Hochheim and Barber, 2014). These changes have been linked to increasing air temperatures, with one study finding for every 1°C temperature increase in fall there is a reduction of 14–15% sea ice during freeze up (Hochheim and Barber, 2014). Modelling studies have projected by mid 21^{st} century, the ice free season will have lengthened by 7 to 9 weeks, with sea ice in southern Hudson Bay and James Bay undergoing the largest changes (Joly et al., 2011). Changes this large will have severe consequences for the polar bear population, particularly in western Hudson Bay (Castro de la Guardia et al., 2013).

1.3 Freshwater Sources

1.3.1 Sea ice

Sea ice and river discharge are the two main sources of freshwater (low salinity water) to the bay (Prinsenberg, 1988; Ridenour et al., 2019a). Thus any changes may have an impact on the circulation and other oceanographic processes in the region. Continental air masses lead to a complete cryogenic cycle in the HBC. Ice melt begins in May in James Bay, with ice free conditions usually achieved by September in Foxe Basin (Prinsenberg, 1986b). Ice drift

is largest in the shoulder seasons, as high ice concentrations and coastlines prevent large ice speeds in winter (Landy et al., 2017). During the melt season, ocean currents export ice out of Hudson Bay in the northeastern corner, while winds push the mobile ice pack to the southern Hudson Bay coast, causing it to be one of the last regions to melt (Wang et al., 1994a).

Freeze up begins in northern Foxe Basin in mid-October, moving southwards (Prinsenberg, 1986b). Complete ice cover in the HBC has usually occurred by mid-December (Markham, 1986). In Hudson Bay, sea ice distribution is asymmetrical due to the prevailing winds and underlying ocean currents, with thicker ice in the east, and thinner ice in the west (Gagnon and Gough, 2006; Kirillov et al., 2020; Landy et al., 2017). The northwestern polynya along the coast of Nunavut and northern Manitoba is known as an 'ice factory', whereby ice is thermodynamically grown, and then moved eastward by currents and winds. In southern and eastern Hudson Bay, ice is compacted together, leading to dynamic ice growth (Kirillov et al., 2020; Landy et al., 2017).

Ice thickness data from satellites have only recently been presented for the HBC, allowing for a more accurate estimate of the freshwater contained in sea ice. Landy et al. (2017) estimated 1253 km^3 of freshwater was contained in April sea ice in the HBC. Estimates from recent modelling studies also show comparable estimates (Ridenour et al., 2019a). Note, that on a seasonal time scale, freshwater contained and released in the sea ice is large, however, the net freshwater flux is small, especially compared to river discharge (Prinsenberg, 1988; Ridenour et al., 2019a; St-Laurent et al., 2012).

1.3.2 River Discharge

Once river discharge enters the ocean, the main question is "where does it go?". Both numerical ocean models and chemical tracers have been used to answer this question. The majority of river inflow found in the interior region was imported by Ekman transport (an oceanic response to wind forcing). Summertime anticyclonic wind stress leads to freshwater transport directed into the bay, while cyclonic wind stress during fall results in freshwater transport from the interior to the boundary current. Seasonally, the interior receives a quarter of the annual riverine water from the boundary (St-Laurent et al., 2011). With the reversal of wind stress to cyclonic in fall and winter, freshwater is released to the boundary (Ridenour et al.,

2019b; St-Laurent et al., 2011).

Using chemical tracers, such as chromophoric dissolved organic matter (CDOM) or $\delta^{18}O$, one can also determine the source of the water, if from sea ice or continental runoff. Coastal waters contain primarily freshwater from riverine sources, while sea ice melt is distributed more evenly around the bay, with higher concentrations in the south due to the southward ice drift (Granskog et al., 2011, 2007). Riverine water has also been detected in low concentrations at depth in the interior as well, due to dense water formation, for which a residence time of 4–14 years has been estimated for these deep Hudson Bay waters (Granskog et al., 2011; Pett et al., 1982).

1.4 General Circulation in the HBC

Flow from the Arctic Ocean enters Foxe Basin through Fury and Hecla Strait. Flow is small through this strait with a summer volume flux of 100 mSv (1 mSv = 1000 m^3/s; Sadler, 1982) and a winter volume flux of 40 mSv (Barber, 1965). Year-round observations have never been captured. These waters join the cyclonic flow in Foxe Basin, flowing southward along the western coast (Defossez et al., 2012; Prinsenberg, 1986b). At Southampton Island, flow splits, with some waters flowing westward to Roes Welcome Sound, and the remainder flowing eastward, between Southampton and Baffin Islands, where the estimated volume flux is 56 mSv (Defossez et al., 2012). Inflowing waters to Foxe Basin are thought to flow along the Baffin Island coast until Prince Charles Island, where waters flow westward to join the southbound Arctic flow on the western side of the basin (Defossez et al., 2012).

Flow through Roes Welcome Sound enters Hudson Bay in the northwest corner, which helps drive the mean cyclonic flow in the bay, along with wind forcing and buoyant forcing from river discharge along the coast (Dunbar, 1982; Hachey, 1935; Prinsenberg, 1986a; Wang et al., 1994c). Flow exits the bay in the northeastern corner. This effectively separates the bay into a fast moving boundary current and a stagnant interior, though exchange between the two regions has been found (St-Laurent et al., 2011). Some studies have put the stability of the cyclonic circulation into question, after showing that the spring freshet in James Bay explains nearly half of the variability in fall sea surface height at Churchill, suggesting that

some water from James Bay must flow westward (Gough et al., 2005). Unfortunately, current observations were not available to confirm this result.

Some coastal flow in Hudson Bay flows into James Bay, which also has flow that circulates cyclonically (Prinsenberg, 1986a). Waters exiting Hudson Bay between Southampton Island and Quebec join the eastward flowing Hudson Strait outflow. Volume estimates from St-Laurent et al. (2011) state that about 607 and 743 km^3/yr of volume and freshwater flow through this gateway respectively, though current reversals have been noted in the past (Granskog et al., 2011; St-Laurent et al., 2012). The currents in this region are largely influenced by the wind, while in data presented by Prinsenberg (1986a), surface flow was directed north while deeper flow between Mansel Island and Quebec was directed southward into Hudson Bay.

Flow along the southern side of Hudson Strait flows eastward, and is characterized by a baroclinic, low salinity current (Drinkwater, 1988; Straneo and Saucier, 2008a). Seasonality in this flow is largely driven by the seasonal cycle of river waters from Hudson and James Bays, with the bulk of freshwater passing through Hudson Strait between October and December (Straneo and Saucier, 2008a). This flow, that contains mainly riverine waters from Hudson and James Bays, is the third largest oceanic source of freshwater to the Labrador Sea, providing the Labrador Current with 15% of its volume and 50% of its freshwater (Straneo and Saucier, 2008a). Low salinity anticyclonic eddies add high frequency variability to the flow. These eddies, generated by storms in Hudson Bay, carry 40% of the volume and 50% of the freshwater in the outflow (Sutherland et al., 2011). Hudson Strait outflow then flows along the Labrador coast to Newfoundland (Florindo-López et al., 2020; Myers et al., 1990; Sutcliffe Jr. et al., 1983), however, farther afield, pathways and the role of Hudson Strait outflow in the North Atlantic is unknown.

On the northern side of Hudson Strait is the inflow, sourced from waters in the Labrador Sea and the Baffin Island Current (Drinkwater, 1988). Year-round observations of the Hudson Strait inflow have yet to be published, thus most of what we know stems from eight weeks of observations in the early 1980s (Drinkwater, 1988). The inflow is a broader, more saline flow, having weaker stratification compared to the outflow on the southern side of the strait (Drinkwater, 1988; Straneo and Saucier, 2008a). Volume transport in the inflow was estimated

to be 0.82 Sv (Drinkwater, 1988), with speculation suggesting that about 25% of Davis Strait outflow feeds the Hudson Strait inflow (Straneo and Saucier, 2008a). Some waters from the inflow are recirculated to the outflow in the cross strait flow that has been noted as far west as Big Island (Drinkwater, 1988; LeBlond et al., 1981). The remaining waters flow westward where their fate is unclear. Studies have suggested that Hudson Strait inflow flows only into Foxe Basin (Drinkwater, 1986; Prinsenberg, 1986a,b), while others say that it flows only into Hudson Bay (Jones and Anderson, 1994). Defossez et al. (2012) determined that Hudson Strait surface waters do not flow into Foxe Basin, however, at depth, warmer waters from either Hudson Bay or Hudson Strait were found. Yet a more recent modelling study indicates that Hudson Strait inflow enters both Hudson Bay and Foxe Basin (Florindo-López et al., 2020; Tao and Myers, to be submitted). Ergo there is no consensus on the fate of the Hudson Strait inflow. The pathways of both the outflow from Foxe Basin and outflow near Southampton Island in northwestern Hudson Bay are also unclear.

1.5 Thesis Objectives

Much of the work in this thesis is part of a larger collaborative project called BaySys. The goal of the project is to separate the impact of regulation of freshwater from changes expected in the HBC due to climate change. The objectives of the BaySys modelling team include using a numerical ocean model to simulate future climate scenarios in the HBC, while also supporting and working with the observational teams, in order to create an observational–modelling framework to improve our understanding of processes occurring in all systems within the HBC. With this in mind, the first part of this thesis (Chapter 3) uses a regional ocean model to evaluate the sensitivity of the HBC to changes in river discharge forcing. This accomplished several goals:

1. The model was evaluated with available observations to ensure that the model was appropriate for the next step of the project.

2. A multi-year freshwater budget of the HBC region, as well as its subregions, was calculated. This provided a first time look at the freshwater budget in some regions, such as Foxe Basin.

3. Changes in river discharge forcing were used to evaluate the sensitivity of the region, which helped to answer the question "how does river discharge impact oceanic circulation in the HBC?"

The results from the first part of the thesis meant that future climate model simulations for the BaySys project could begin. These results also provided present day estimates of the freshwater budget for this region.

The second part of the thesis (Chapter 4) was motivated by some observations noted in Chapter 3. Earlier studies have found that the year-round circulation in Hudson Bay is stably cyclonic. However, exchange between the interior and boundary regions of the bay, as well as anticyclonic flow patterns in some months, indicated that a seasonal flow pattern might be present. Therefore, the focus of Chapter 4 is on seasonal flow patterns within Hudson Bay and the processes involved.

The third and final component to this thesis focuses on Hudson Strait. As mentioned earlier, year-round observations have been presented for the Hudson Strait outflow, yet no observations for the Hudson Strait inflow have been published. This final chapter presents the first year-round observations of the Hudson Strait inflow. Seasonal variability of inflow properties is shown, and potential source waters that feed the inflow, and pathways within the HBC are discussed.

This thesis is organized with a detailed description of the ocean model used in Chapters 3 and 4 following this introduction. Results chapters (3, 4, and 5) are written with their own introduction, methods, results, and discussion sections. A conclusion to the thesis is the final chapter (Chapter 6).

Bibliography

Aagaard, K. and Carmack, E. C. (1989). The role of sea ice and other fresh water in the Arctic circulation. *Journal of Geophysical Research: Oceans*, 94(C10):14485–14498.

Babb, D., Andrews, J., Dawson, J., Landry, D., Mussells, O., and Weber, M. (2019). Transportation and community use of the marine enviroment. In Kuzyk, Z. and L.M. Candlish, L. E., editors, *From Science to Policy in the Greater Hudson Bay Marine Region: An Integrated Regional Impact Study (IRIS) of Climate Change and Modernization*, pages 341–377.

Bamber, J., van den Broeke, M., Ettema, J., Lenaerts, J., and Rignot, E. (2012). Recent large increases in freshwater fluxes from Greenland into the North Atlantic. *Geophysical Research Letters*, 39(19).

Barber, F. G. (1965). Current Observations in Fury and Hecla Strait. *Journal of the Fisheries Research Board of Canada*, 22(1):225–229.

Brown, N. J., Nilsson, J., and Pemberton, P. (2019). Arctic Ocean Freshwater Dynamics: Transient Response to Increasing River Runoff and Precipitation. *Journal of Geophysical Research: Oceans*, 124(7):5205–5219.

Castro de la Guardia, L., Derocher, A. E., Myers, P. G., Terwisscha van Scheltinga, A. D., and Lunn, N. J. (2013). Future sea ice conditions in Western Hudson Bay and consequences for polar bears in the 21st century. *Global Change Biology*, 19(9):2675–2687.

Castro de la Guardia, L., Myers, P. G., Derocher, A. E., Lunn, N. J., and Terwisscha van Scheltinga, A. D. (2017). Sea ice cycle in western Hudson Bay, Canada, from a polar bear perspective. *Marine Ecology Progress Series*, 564:225–233.

Defossez, M., Saucier, F., Myers, P., Caya, D., and Dumais, J. (2012). Comparing Winter and Summer Simulated Estuarine Circulations in Foxe Basin, Canada. *Atmosphere-Ocean*, 50(3):386 – 401.

Déry, S. J., Hernández-Henríquez, M. A., Burford, J. E., and Wood, E. F. (2009). Observational evidence of an intensifying hydrological cycle in northern Canada. *Geophysical Research Letters*, 36(13).

Déry, S. J., Mlynowski, T. J., Hernández-Henríquez, M. A., and Straneo, F. (2011). Interannual variability and interdecadal trends in Hudson Bay streamflow. *Journal of Marine Systems*, 88:341 – 351.

Déry, S. J., Stadnyk, T. A., MacDonald, M. K., and Gauli-Sharma, B. (2016). Recent trends and variability in river discharge across northern Canada. *Hydrology and Earth System Sciences*, 20(12):4801 – 4818.

Déry, S. J., Stadnyk, T. A., MacDonald, M. K., Koenig, K. A., and Guay, C. (2018). Flow alteration impacts on Hudson Bay river discharge. *Hydrological Processes*, 32(24):3576–3587.

Drinkwater, K. (1986). Chapter 13 Physical Oceanography of Hudson Strait and Ungava Bay. In Martini, I., editor, *Canadian Inland Seas*, volume 44 of *Elsevier Oceanography Series*, pages 237–264. Elsevier.

Drinkwater, K. F. (1988). On the Mean and Tidal Currents in Hudson Strait. *Atmosphere–Ocean*, 26(2):252 – 266.

Dunbar, M. (1982). Oceanographic research in Hudson and James Bays. *Le Naturaliste Canadien*, 109(4):677 – 683.

Florindo-López, C., Bacon, S., Aksenov, Y., Chafik, L., Colbourne, E., and Holliday, N. P. (2020). Arctic Ocean and Hudson Bay Freshwater Exports: New Estimates from 7 Decades of Hydrographic Surveys on the Labrador Shelf. *Journal of Climate*.

Gaden, A., Chételat, J., Heath, J., Kuzyk, Z., Stern, G., and Wang, F. (2019). Contaminant cycling, ecosystem pathways, and wildlif trends in a changing climate. In Kuzyk, Z. and L.M. Candlish, L. E., editors, *From Science to Policy in the Greater Hudson Bay Marine Region: An Integrated Regional Impact Study (IRIS) of Climate Change and Modernization*, pages 311–339.

Gagnon, A. S. and Gough, W. A. (2005). Trends in the Dates of Ice Freeze-up and Breakup over Hudson Bay, Canada. *Arctic*, 58(4):370–382.

Gagnon, A. S. and Gough, W. A. (2006). East-west asymmetry in long-term trends of landfast ice thickness in the Hudson Bay region, Canada. *Climate Research*, 32:177–186.

Galbraith, P. S. and Larouche, P. (2011). Reprint of "Sea-surface temperature in Hudson Bay and Hudson Strait in relation to air temperature and ice cover breakup, 1985–2009". *Journal of Marine Systems*, 88(The Hudson Bay System):463 – 475.

Gough, W. A., Robinson, C., and Hosseinian, R. (2005). The Influence of James Bay River Discharge on Churchill, Manitoba Sea Level. *Polar Geography*, 29(3):213–223.

Granskog, M. A., Kuzyk, Z. Z. A., Azetsu-Scott, K., and Macdonald, R. W. (2011). Distributions of runoff, sea-ice melt and brine using δ^{18}O and salinity data — A new view on freshwater cycling in Hudson Bay. *Journal of Marine Systems*, 88:362 – 374.

Granskog, M. A., Macdonald, R. W., Mundy, C.-J., and Barber, D. G. (2007). Distribution, characteristics and potential impacts of chromophoric dissolved organic matter (CDOM) in Hudson Strait and Hudson Bay, Canada. *Continental Shelf Research*, 27(15):2032 – 2050.

Hachey, H. B. (1935). Circulation of Hudson Bay water as indicated by drift bottles. *Science*, 82:275 – 276.

Heath, J. and Sanikiluaq, C. (2014). People of a feather. film. Arctic Eider Society.

Hochheim, K. P. and Barber, D. G. (2014). An Update on the Ice Climatology of the Hudson Bay System. *Arctic, Antarctic, and Alpine Research*, 46(1):66–83.

Holmes, R. M., McClelland, J. W., Peterson, B. J., Tank, S. E., Bulygina, E., Eglinton, T. I., Gordeev, V. V., Gurtovaya, T. Y., Raymond, P. A., Repeta, D. J., Staples, R., Striegl, R. G., Zhulidov, A. V., and Zimov, S. A. (2012). Seasonal and Annual Fluxes of Nutrients and Organic Matter from Large Rivers to the Arctic Ocean and Surrounding Seas. *Estuaries and Coasts*, 35(2):369–382.

Joly, S., Senneville, S., Caya, D., and Saucier, F. (2011). Sensitivity of Hudson Bay Sea ice and ocean climate to atmospheric temperature forcing. *Climate Dynamics*, 36(9/10):1835 – 1849.

Jones, E. P. and Anderson, L. G. (1994). Northern Hudson Bay and Foxe Basin: Water masses, circulation and productivity. *Atmosphere-Ocean*, 32(2):361–374.

Kirillov, S., Babb, D., Dmitrenko, I., Landy, J., Lukovich, J., Ehn, J., Sydor, K., Barber, D., and Stroeve, J. (2020). Atmospheric Forcing Drives the Winter Sea Ice Thickness Asymmetry of Hudson Bay. *Journal of Geophysical Research: Oceans*, 125(2).

Landy, J. C., Ehn, J. K., Babb, D. G., Thériault, N., and Barber, D. G. (2017). Sea ice thickness in the Eastern Canadian Arctic: Hudson Bay Complex & Baffin Bay. *Remote Sensing of Environment*, 200(Supplement C):281 – 294.

LeBlond, P. H., Osborn, T., Hodgins, D., Goodman, R., and Metge, M. (1981). Surface circulation in the Western Labrador Sea. *Deep Sea Research Part A. Oceanographic Research Papers*, 28(7):683 – 693.

MacDonald, M. K., Stadnyk, T. A., Déry, S. J., Braun, M., Gustafsson, D., Isberg, K., and Arheimer, B. (2018). Impacts of 1.5 and 2.0°C Warming on Pan-Arctic River Discharge Into the Hudson Bay Complex Through 2070. *Geophysical Research Letters*, 45(15):7561–7570.

Markham, W. (1986). Chapter 6 The Ice Cover. In Martini, I., editor, *Canadian Inland Seas*, volume 44 of *Elsevier Oceanography Series*, pages 101 – 116. Elsevier.

Myers, R. A., Akenhead, S. A., and Drinkwater, K. (1990). The influence of Hudson Bay runoff and ice–melt on the salinity of the inner Newfoundland Shelf. *Atmosphere-Ocean*, 28(2):241–256.

Pett, R., Roff, J., and I.P., M. (1982). Some observations and deductions concerning the deep waters of Hudson Bay. *Naturaliste Canadien*, pages 767–774.

Prinsenberg, S. (1986a). Chapter 10 The Circulation Pattern and Current Structure of Hudson Bay. In Martini, I., editor, *Canadian Inland Seas*, volume 44 of *Elsevier Oceanography Series*, pages 187 – 204. Elsevier.

Prinsenberg, S. (1986b). Chapter 12 On the Physical Oceanography of Foxe Basin. In Martini, I., editor, *Canadian Inland Seas*, volume 44 of *Elsevier Oceanography Series*, pages 217 – 236. Elsevier.

Prinsenberg, S. (1988). Ice-Cover and Ice-Ridge Contributions to the Freshwater Contents of Hudson Bay and Foxe Basin. *Arctic*, 41(1):6–11.

Ridenour, N. A., Hu, X., Jafarikhasragh, S., Landy, J. C., Lukovich, J. V., Stadnyk, T. A., Sydor, K., Myers, P. G., and Barber, D. G. (2019a). Sensitivity of freshwater dynamics to ocean model resolution and river discharge forcing in the Hudson Bay Complex. *Journal of Marine Systems*, 196:48 – 64.

Ridenour, N. A., Hu, X., Sydor, K., Myers, P. G., and Barber, D. G. (2019b). Revisiting the Circulation of Hudson Bay: Evidence for a Seasonal Pattern. *Geophysical Research Letters*, 46(7):3891–3899.

Sadler, H. E. (1982). Water flow into Foxe Basin through Fury and Hecla Strait. *Naturaliste Canadien*, pages 701 – 707.

Saucier, F. and Dionne, J. (1998). A 3-D coupled ice-ocean model applied to Hudson Bay, Canada: The seasonal cycle and time-dependent climate response to atmospheric forcing and runoff. *Journal Of Geophysical Research–Oceans*, 103(C12):27689 – 27705.

Shiklomanov, I. A. and Shiklomanov, A. I. (2003). Climatic Change and the Dynamics of River Runoff into the Arctic Ocean. *Water Resources*, 30(6):593–601.

St-Laurent, P., Straneo, F., and Barber, D. G. (2012). A conceptual model of an Arctic sea. *Journal of Geophysical Research: Oceans*, 117(C6).

St-Laurent, P., Straneo, F., Dumais, J.-F., and Barber, D. G. (2011). What is the fate of the river waters of Hudson Bay? *Journal of Marine Systems*, 88:352 – 361.

Straneo, F. and Saucier, F. J. (2008). The Arctic–Subarctic Exchange Through Hudson Strait. In Dickson, R. R., Meincke, J., and Rhines, P., editors, *Arctic–Subarctic Ocean Fluxes: Defining the Role of the Northern Seas in Climate*, pages 249–261. Springer Netherlands, Dordrecht.

Sutcliffe Jr., W. H., Loucks, R. H., Drinkwater, K. F., and Coote, A. R. (1983). Nutrient Flux onto the Labrador Shelf from Hudson Strait and its Biological Consequences. *Canadian Journal of Fisheries and Aquatic Sciences*, 40(10):1692–1701.

Sutherland, D. A., Straneo, F., Lentz, S. J., and Saint-Laurent, P. (2011). Observations of fresh, anticyclonic eddies in the Hudson Strait outflow. *Journal of Marine Systems*, 88(The Hudson Bay System):375 – 384.

Tao, R. and Myers, P. (to be submitted). Modelling the Advection of Pollutants in the Hudson Bay Complex. *Journal of Marine Systems*.

Wang, J., Mysak, L., and Ingram, R. (1994a). A numerical-simulation of sea-ice cover in Hudson Bay. *Journal of Physical Oceanography*, 24(12):2515 – 2533.

Wang, J., Mysak, L. A., and Ingram, R. G. (1994b). A Three-Dimensional Numerical Simulation of Hudson Bay Summer Ocean Circulation: Topographic Gyres, Separations, and Coastal Jets. *Journal of Physical Oceanography*, 24(12):2496–2514.

Yang, Q., Dixon, T. H., Myers, P. G., Bonin, J., Chambers, D., van den Broeke, M. R., Ribergaard, M. H., and Mortensen, J. (2016). Recent increases in Arctic freshwater flux affects Labrador Sea convection and Atlantic overturning circulation. *Nature Communications*, 7(1).

Zhang, X., He, J., Zhang, J., Polyakov, I., Gerdes, R., Inoue, J., and Wu, P. (2012). Enhanced poleward moisture transport and amplified northern high-latitude wetting trend. *Nature Climate Change*, 3(1):47 – 51.

Chapter 2

Model Description

Nucleus for European Modelling of the Ocean (NEMO) is a numerical coupled ice-ocean model that is used for forecasting and studying processes in the ocean and climate system. The time scale can range from minutes to tens of years, while the spatial range varies from kilometers to the entire globe. NEMO consists of five components, the blue ocean (ocean dynamics and thermodynamics), white ocean (sea ice dynamics and thermodynamics), and green ocean (biogeochemical dynamics) which make up the model, with two additional numerical tools: a two-way nesting tool which allows for higher resolution regions within a coarser grid, and an assimilation tool allowing for reforecasts and model constraining. The official NEMO website, `http://www.nemo-ocean.eu/`, contains NEMO documentation, announcements, and updates. The focus of this chapter will be on the blue and white oceans, which are the two model components that I have used in this thesis.

2.1 The Blue Ocean

The ocean component in the NEMO framework is described by the primitive equations in a curvilinear coordinate system (Madec et al., 1998; Madec and the NEMO team, 2008). The model uses six assumptions:

Spherical earth approximation

Earth's gravity is simplified with the vertical gravity vector directed to Earth's center. In the model, gravitational acceleration, g, is 9.8 m s^{-2} and is a constant.

Thin-shell approximation

Given Earth's radius of 6400 km, and a mean ocean depth of 4 km with a maximum of 10 km, the depth of the ocean is small in comparison. Therefore, the distance from the centre of Earth to a given location in the ocean is assumed constant (Earth's radius).

Turbulent closure hypothesis

When describing turbulence, there are more unknown variables (that do not have an equation defining it) than equations, meaning we do not have a closed set of equations (Stull, 1988). To overcome this problem, the effect of small-scale processes/turbulence on the mean flow are described as large scale features.

Boussinesq approximation

Variations in density are neglected with the exception of its contribution to the buoyancy force.

Hydrostatic approximation

The vertical momentum equation can be reduced to the hydrostatic balance as oceanic flow in the horizontal is faster and on a much larger scale than flow in the vertical. However, during convective processes, where horizontal and vertical scales are similar, the hydrostatic approximation does not hold, and vertical acceleration must be parametrized.

Incompressibility approximation

We assume that seawater is incompressible, so that the density remains constant $\left(\frac{D\rho(T,S,p)}{Dt} = 0\right)$ following the motion.

2.1.1 Primitive Equations

The curvilinear coordinate system that the model uses contains two horizontal vectors (**i**, **j**) which are perpendicular to the local vertical vector (**k**). The following seven primitive equations are written in accordance with the six assumptions mentioned previously, as well as the curvilinear coordinate system used in NEMO.

Horizontal equation of motion

$$\frac{\partial \boldsymbol{U}_h}{\partial t} = -\underbrace{\left[(\nabla \times \boldsymbol{U}) \times \boldsymbol{U} + \frac{1}{2}\nabla(\boldsymbol{U}^2)\right]_h}_{\text{Inertial term}} - \underbrace{f\boldsymbol{k} \times \boldsymbol{U}_h}_{\text{Coriolis term}} - \underbrace{\frac{1}{\rho_o}\nabla_h p}_{\text{Pressure Gradient term}} + \underbrace{D^{\boldsymbol{U}} + F^{\boldsymbol{U}}}_{\substack{\text{small-scale parametrizations} \\ \text{+ surface terms}}} \tag{2.1}$$

Hydrostatic equilibrium

$$\frac{\partial p}{\partial z} = -\rho g \tag{2.2}$$

Incompressibility equation

$$\nabla \cdot \boldsymbol{U} = 0 \tag{2.3}$$

Heat conservation

$$\frac{\partial T}{\partial t} = -\underbrace{\nabla \cdot (T\boldsymbol{U})}_{\text{Heat divergence}} + \underbrace{D^T + F^T}_{\substack{\text{small-scale parametrizations} \\ \text{+ surface forcing}}} \tag{2.4}$$

Salt conservation

$$\frac{\partial S}{\partial t} = -\underbrace{\nabla \cdot (S\boldsymbol{U})}_{\text{Salt divergence}} + \underbrace{D^S + F^S}_{\substack{\text{small-scale parametrizations} \\ \text{+ surface forcing}}} \tag{2.5}$$

Equation of state

$$\rho = \rho(T, S, p) \tag{2.6}$$

where D and F represent small-scale physics parametrizations and surface forcing respectively, for temperature (T), salinity (S), and velocity ($\mathbf{U}$). The 3D velocity vector is given by $\mathbf{U} = \mathbf{U}_h + w\mathbf{k}$, where $\mathbf{U}_h = (U, V)$ is the horizontal flow components and w is the vertical velocity in the $\mathbf{k}$ direction. The variables f, p, and ρ_o stand for the Coriolis force, pressure, and reference density respectively. The density, ρ, is derived from the equation of state (Equation 2.6). Lastly, g is the gravity constant, and z and t indicate depth and time accordingly.

Lateral boundaries in the model are provided by the coastlines, while the ocean bottom and atmosphere (or sea ice) provide the boundaries for the bottom and top of the ocean respectively. Mathematically, the bottom boundary is defined as $z = -H(i, j)$ and the surface boundary is given as $z = \eta(i, j, t)$ (Figure 2.1). Both H and η are referenced to the mean sea surface, $z = 0$. There is no heat, salt, or momentum transfer *across* the bottom boundary, however, there is momentum transfer via friction. The kinematic boundary condition for the

ocean bottom is

$$w|_{z=-H} = -\boldsymbol{U}_h \cdot \nabla H \tag{2.7}$$

At the surface, there is exchange of heat, salt (or freshwater), and momentum from sea ice, runoff, and the atmosphere. Thus, the kinematic surface condition includes all processes that displace the sea surface from 0, and is defined as

$$w|_{z=\eta} = \frac{\partial \eta}{\partial t} + \boldsymbol{U}_h \cdot \nabla_h \eta|_{z=\eta} - (P - E + R + I) \tag{2.8}$$

where P, E, R, and I represent precipitation, evaporation, runoff (from rivers or ice sheets), and ice melt/growth fluxes respectively. The first term on the right hand side of Equation 2.8 can be derived by vertically integrating Equation 2.3 and using the surface and bottom kinematic boundary conditions to obtain

$$\frac{\partial \eta}{\partial t} = (P - E + R + I) - \nabla \cdot [(H + \eta)\overline{\boldsymbol{U}_h}] \tag{2.9}$$

where $\overline{\boldsymbol{U}_h} = \frac{1}{H+\eta} \int_{-H}^{\eta} \boldsymbol{U}_h dz$ is the horizontal velocity averaged in the vertical. This dynamic boundary condition allows for pressure continuity at $z = \eta$ as well as exchanges of mass, heat, momentum, and salt between the ocean and atmosphere or sea ice.

One minor disadvantage to using a free surface formulation in a model is that this can lead to the generation of surface gravity waves. For the work in this thesis, these gravity waves are high frequency noise. To dampen these waves, we use a linear filter free surface model (Roullet and Madec, 2000) which adds an additional dampening term to the equation of motion (Equation 2.1)

$$\frac{\partial \boldsymbol{U}_h}{\partial t} = M - g\nabla(\tilde{\rho}\eta) - gT_c\nabla\Big(\tilde{\rho}\frac{\partial \eta}{\partial t}\Big) \tag{2.10}$$

where M includes the Coriolis force, hydrostatic pressure gradient, viscous, and non-linear terms. The parameter characterizing this force is T_c, with units of time, while the dimensionless density is given by $\tilde{\rho} = \frac{\rho}{\rho_o}$.

This model uses free-slip for the lateral boundary condition. Deremble et al. (2011) argue that even though the no-slip boundary condition is the most suitable condition for the primitive equations in terms of small-scale molecular processes, their drag-slip boundary con-

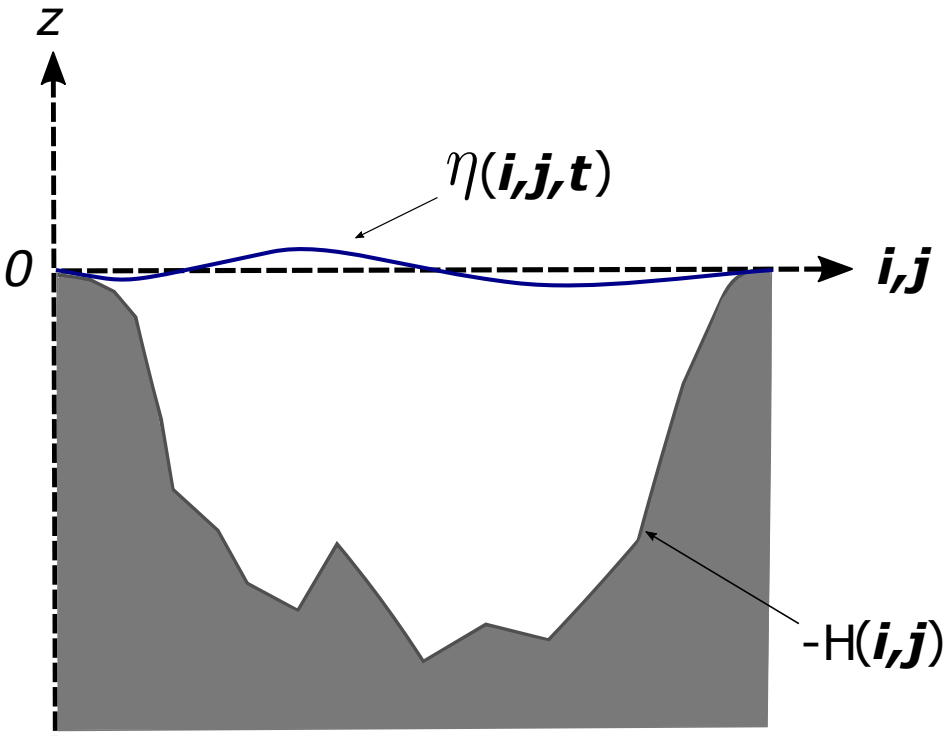

Figure 2.1: The ocean in NEMO is laterally bounded by coastlines, bounded below by the ocean floor, shown by -H, and bounded on the surface by η. Both -H and η are relative to $z = 0$.

dition is more similar to the free-slip boundary condition than the standard no-slip boundary condition.

2.1.2 Curvilinear coordinate system and spatial discretization

NEMO uses a curvilinear z-coordinate system, with vertical levels at specific depths (z) along the local vertical vector, $\boldsymbol{k}$. Horizontal vectors ($\boldsymbol{i}, \boldsymbol{j}$) are perpendicular to $\boldsymbol{k}$, and are aligned with Earth's geographic coordinate system, latitude and longitude. The lines of longitude converge at the north and south poles, creating a singularity (a point that is not well defined or well behaved) in the model (Eby and Holloway, 1994, Murray, 1996, Roberts et al., 2006). To avoid this singularity, the poles have been shifted to land using the tri pole transformation described in Murray (1996). The re-projected horizontal grid uses the staggered Arakawa C grid (Mesinger et al., 1976). Scalar variables, such as T, S, and p are located in the center of the grid cell (Figure 2.3), while vector variables, such as U, V, and W are located on the

west/east, south/north, and bottom/top faces respectively. Both planetary (f) and relative (ζ) vorticity are defined on the F point (blue circles in Figure 2.3). Grid cell size is defined by three local scale factors $e1$, $e2$, and $e3$ providing the width, length, and height of each grid cell respectively (Figure 2.3).

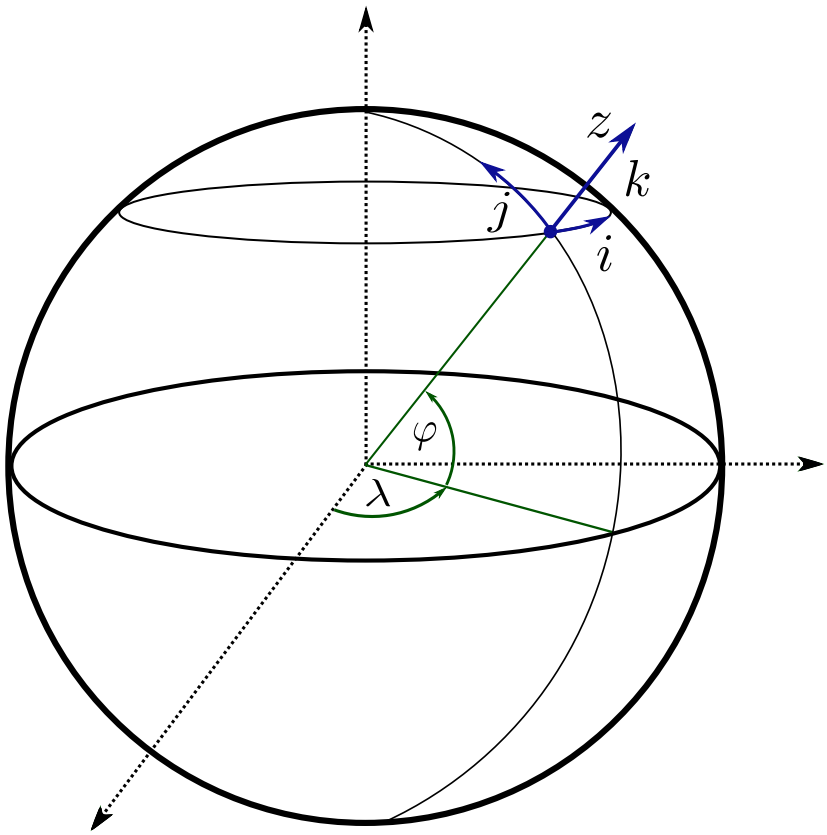

Figure 2.2: NEMO coordinate system uses a curvilinear z-coordinate system. The horizontal vectors, $\boldsymbol{i}$ and $\boldsymbol{j}$ (in blue) are described by λ and φ respectively (in green), and are aligned with Earth's latitude and longitude. The vertical vector, $\boldsymbol{k}$ (blue), is perpendicular to $\boldsymbol{i}$ and $\boldsymbol{j}$, and is described by z.

In the vertical, we use z-coordinates with partial steps (Bernard et al., 2006), as this has been found to resolve topography better (Figure 2.4). Pressure gradient calculations are simple and accurate when calculated on z-coordinates, however, the drawback is that bottom bathymetry is not well resolved. Using partial steps allows for the bottom level to vary in thickness, so as to better resolve the bathymetry while still keeping pressure gradient calculations simple.

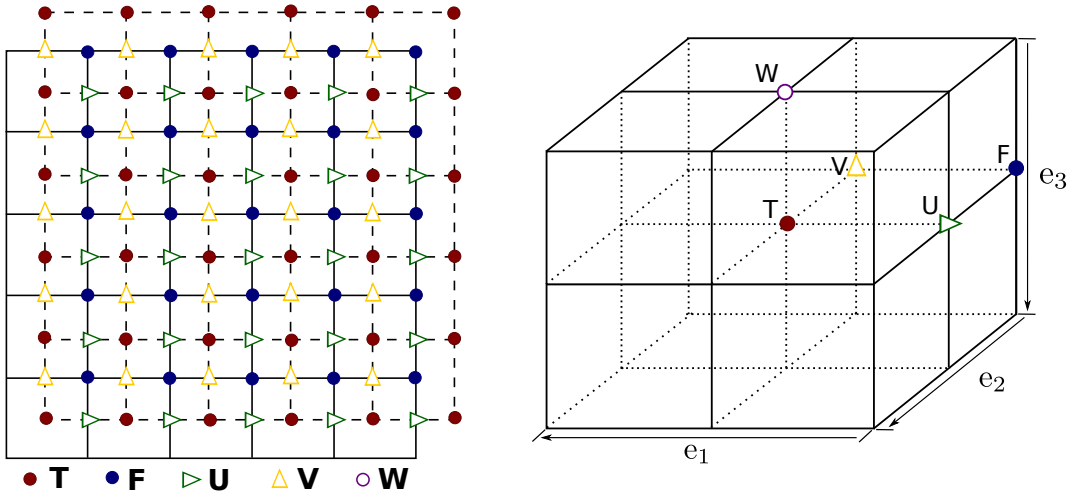

(a) (b)

Figure 2.3: The model grid shown in 2D (a) and 3D (b). Scalar variables are located on the T point, shown by the red circles, while vorticity is defined and located at the F point, shown by blue circles. Velocity components U and V are shown by the green and yellow triangles respectively. Vertical velocities (W) are in line with the T point, but located half a grid cell above, on the top face of the grid cell. The three local scale factors, e_1, e_2, and e_3, which define the size of the grid cell are shown in (b).

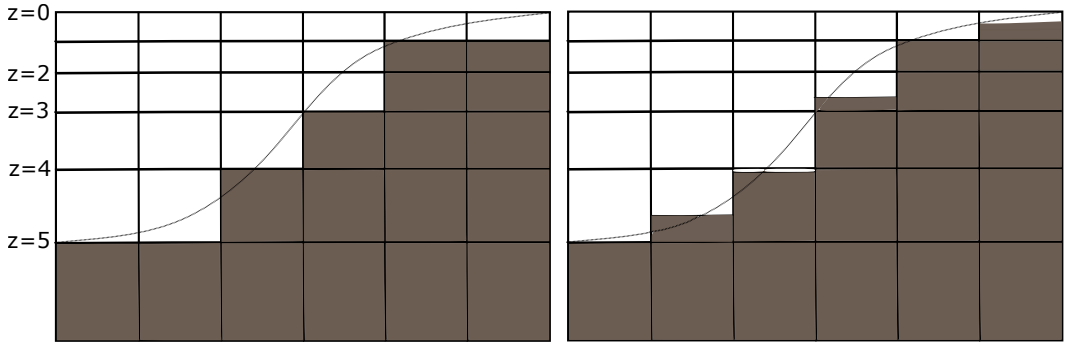

(a) (b)

Figure 2.4: The bottom bathymetry, as described by z-coordinates without partial steps (a), and with partial steps (b). True bathymetry is shown by the thin line, while thick lines show model grid cells.

2.1.3 Subgrid Scale Physics

2.1.3.1 Turbulence

Numerical models solve various processes on a finite grid with finite time steps, meaning that processes occurring on a smaller space or time scale must be parametrized. Turbulence is one of these processes. Important on the large scale, small-scale turbulent motions, which stem from the advection term in the equation of motion (Equation 2.1) and represented by $D^{\boldsymbol{U}}$, D^S, and D^T, are parametrized to close the system of equations.

The vertical component of the turbulent fluxes for momentum, heat, and salinity are

$$D_v^{\boldsymbol{U}} = \frac{\partial}{\partial z}\Big(A_v^m \frac{\partial \boldsymbol{U}_h}{\partial z}\Big) \tag{2.11}$$

$$D_v^T = \frac{\partial}{\partial z}\Big(A_v^T \frac{\partial T}{\partial z}\Big) \tag{2.12}$$

$$D_v^S = \frac{\partial}{\partial z}\Big(A_v^T \frac{\partial S}{\partial z}\Big) \tag{2.13}$$

where A_v^m and A_v^T denote the vertical eddy viscosity and diffusivity coefficients accordingly. For non-turbulent conditions A_v^m and A_v^T are constants, with values of 1×10^{-4} m^2 s^{-1} and 1×10^{-5} m^2 s^{-1} respectively, while for turbulent conditions, A_v^m and A_v^T are calculated using the turbulent kinetic energy scheme described in the following paragraph. The assumption here, is that the vertical turbulent fluxes linearly depend on large-scale quantity gradients, resembling equations for molecular dissipation and diffusion. The vertical acceleration is a parametrized quantity because vertical motions are much smaller than the vertical grid spacing.

For turbulent conditions, the vertical eddy viscosity and diffusivity coefficients are computed using a turbulent kinetic energy (TKE) turbulence closure scheme (Blanke and Delecluse, 1993; Bougeault and Lacarrere, 1989; Gaspar et al., 1990; Madec et al., 1998) based on the initial values. The TKE is defined as $\bar{e} = \frac{1}{2}(\overline{u'^2} + \overline{v'^2} + \overline{w'^2})$ and the turbulent closure scheme is comprised of the following equations:

$$\frac{\partial \bar{e}}{\partial t} = \underbrace{\frac{A_v^m}{e_3^2}\Big[\Big(\frac{\partial u}{\partial k}\Big)^2 + \Big(\frac{\partial v}{\partial k}\Big)^2\Big]}_{\text{vertical shear}} - \underbrace{A_v^T N^2}_{\text{stratification}} + \underbrace{\frac{1}{e_3}\frac{\partial}{\partial k}\Big[\frac{A_v^m}{e_3}\frac{\partial \bar{e}}{\partial k}\Big]}_{\text{vertical diffusion}} - \underbrace{c_\epsilon \frac{\bar{e}^{\frac{3}{2}}}{l_\epsilon}}_{\text{dissipation}} \tag{2.14}$$

$$A_m^v = c_k l_k \sqrt{\bar{e}} \tag{2.15}$$

$$A_v^T = \frac{A_v^m}{P_{rt}} \tag{2.16}$$

where u', v', and w' are the turbulent components of the flow, k as the vertical index, $N = \sqrt{-\frac{g}{\rho_o}\frac{d\bar{\rho}}{dz}}$ and $P_{rt} = \frac{\nu}{\alpha}$ are the local Brunt–Väisälä (buoyancy) frequency and the Prandtl number, where ν is momentum diffusivity and α is thermal diffusivity. Constants $c_k = 0.1$ and $c_\epsilon = \sqrt{2}/2$, while the dissipation (l_ϵ) and mixing length (l_k) scales are defined as follows

$$l_k = l_\epsilon = \frac{\sqrt{2\bar{e}}}{N} \tag{2.17}$$

$$\frac{1}{e_3}\Big|\frac{\partial l}{\partial k}\Big| \leq 1 \text{ with } l = l_k = l_\epsilon \tag{2.18}$$

Horizontal components (or along isopycnals) of the turbulent flux use a Laplacian operator ($\nabla \cdot \nabla$) for temperature and salinity diffusion and are given by

$$D_l^T = \nabla \cdot (A_l^T \Re \nabla T) \text{ with } \Re = \begin{pmatrix} 1 & 0 & -r_1 \\ 0 & 1 & -r_2 \\ -r_1 & -r_2 & r_1^2 + r_2^2 \end{pmatrix} \tag{2.19}$$

where T denotes the tracer (i.e.. temperature or salinity) r_1 and r_2 are the slopes between the vertical model layer and the surface which the diffusive operator acts on (i.e. the slope of the isopycnal). The horizontal eddy viscosity is shown by A_l^T. Thus, in z-coordinates, these values are zero ($r_1 = r_2 = 0$), since the surface that the diffusive operator acts on is the same as the vertical model level. This results in a much simpler horizontal diffusion equation

$$D_l^T = \frac{1}{e_1 e_2}\Big[\frac{\partial}{\partial i}\Big(\frac{e_2}{e_1}A_l^T\frac{\partial T}{\partial i}\Big|_z\Big)\Big|_z + \frac{\partial}{\partial j}\Big(\frac{e_1}{e_2}A_l^T\frac{\partial T}{\partial j}\Big|_z\Big)\Big|_z\Big] \tag{2.20}$$

By using the Laplacian operator, it is possible to separate the divergent and rotational components of the flow. The rotational component, due to relative vorticity, is given by

$$\zeta = \frac{1}{e_1 e_2}\Big[\frac{\partial(e_2 v)}{\partial i} - \frac{\partial(e_1 u)}{\partial j}\Big] \tag{2.21}$$

while the divergent part of the flow is given as

$$\chi = \frac{1}{e_1 e_2}\Big[\frac{\partial(e_2 u)}{\partial i} + \frac{\partial(e_1 v)}{\partial j}\Big] \tag{2.22}$$

Momentum diffusion to the second order is defined as

$$\begin{aligned} D_l^U &= \Delta_h(A_l^m \boldsymbol{U}) \\ &= \nabla_h(A_l^m \chi) + \nabla_h \times (A_l^m \zeta \boldsymbol{k}) \\ &= \begin{pmatrix} \dfrac{1}{e_1}\dfrac{\partial(A_l^m \chi)}{\partial i} - \dfrac{1}{e_2 e_3}\dfrac{\partial(A_l^m e_3 \zeta)}{\partial j} \\ \dfrac{1}{e_2}\dfrac{\partial(A_l^m \chi)}{\partial j} + \dfrac{1}{e_1 e_3}\dfrac{\partial(A_l^m e_3 \zeta)}{\partial i} \end{pmatrix} \end{aligned}$$

The configuration used in this thesis uses a fourth order operator (bilaplacian) for momentum diffusion, which means, in practice, the second order operator is applied twice.

2.1.3.2 Friction at boundary layers

Friction at boundary layers, for instance where the ocean meets the ocean floor, is another process that needs to be parametrized. A nonlinear bottom friction parametrization was chosen, which defines the downward flux of horizontal momentum as quadratic, and is given as:

$$F_h^{\boldsymbol{U}} = \frac{A_v^m}{e_3}\frac{\partial \boldsymbol{U}_h}{\partial k} = C_D \sqrt{u_b^2 + v_b^2 + e_b} \;\; \boldsymbol{U}_h^b \tag{2.23}$$

where $\boldsymbol{U}_h^b = (u_b, v_b)$ is the horizontal, near bottom ocean velocity, C_D is a drag coefficient, and e_b is the bottom turbulent kinetic energy from short time scale flow, such as breaking internal waves and tides.

The magnitude of the bottom friction is determined by two friction coefficients, defined as:

$$c_b^u = -C_D \left[u^2 + \left(\bar{\bar{v}}^{i+1,j} \right)^2 + e_b \right]^{1/2} \tag{2.24}$$

$$c_b^v = -C_D \left[\left(\bar{\bar{u}}^{i,j+1} \right)^2 + v^2 + e_b \right]^{1/2} \tag{2.25}$$

Bottom friction is then included in the simulated flow by the addition of the general momentum flow and the flow due to bottom friction.

2.1.4 Time discretization

A three level time stepping scheme is used in NEMO, and is as follows

$$x^{t+\Delta t} = x^{t-\Delta t} + 2\Delta t RHS_x^{t-\Delta t,t,t+\Delta t} \tag{2.26}$$

where x represents a scalar or vector (u, v, T, or S), Δt is the time step, superscripts denote the time level x is evaluated at, and RHS stands for Right Hand Side of the corresponding time stepping scheme.

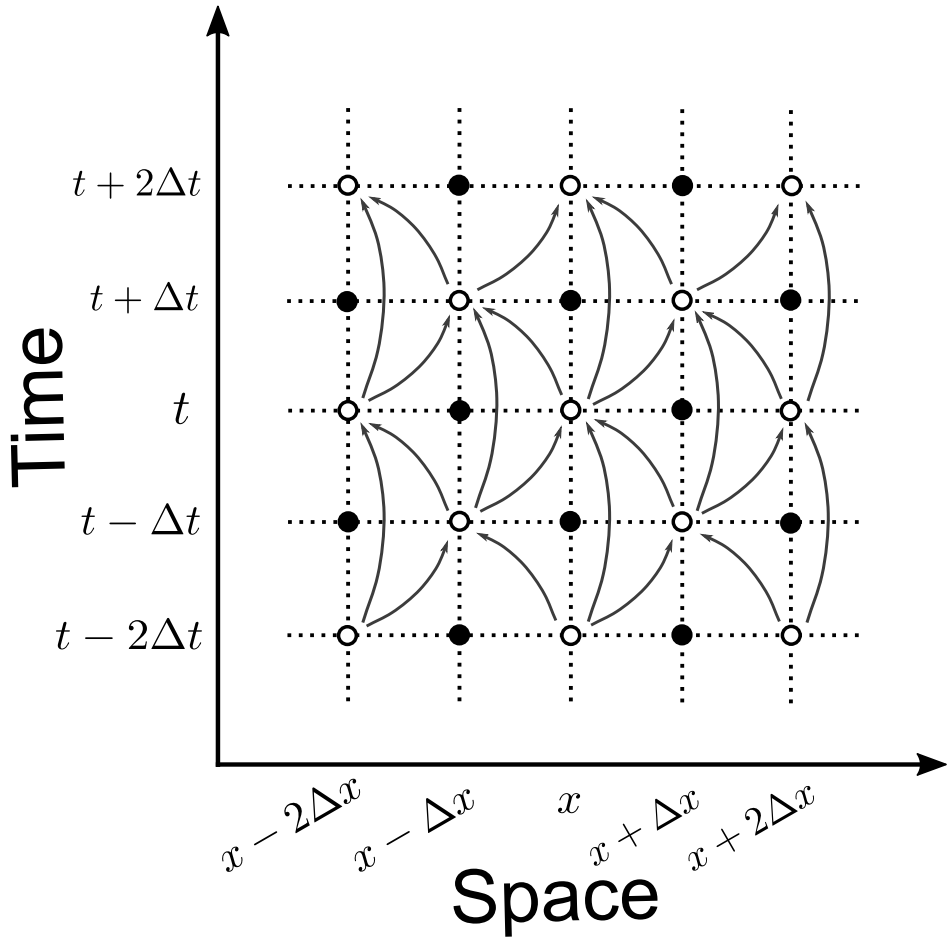

Figure 2.5: The time stepping scheme (Leapfrog scheme) used for non-diffusive processes, which calculates the even time steps in this schematic. Arrows directed to the white points are inputs from other space and time steps, while arrows directed away from the white points shows where the output will be used as input.

Non-diffusive processes, such as the advection, Coriolis, and pressure gradient terms in Equation 2.1, use the Leapfrog scheme (Mesinger et al., 1976), which is a time centered

scheme (Figure 2.5). The Leapfrog scheme has second order accuracy, and does not amplify or damp linear oscillatory motion. A drawback of this scheme, is the presence of an non-physical solution called a computational mode. To avoid the computational mode, we use a Robert–Asselin time filter with the Leapfrog scheme (Asselin, 1972; Robert, 1966). This time filter mixes the odd and even time steps, as the separation of the time steps can be seen in Figure 2.5, with the black points not contributing to the time evolution of a variable. The Robert–Asselin time filter is given as

$$x_F^t = x^t + \gamma[x_F^{t-\Delta t} - 2x^t + x^{t+\Delta t}] \tag{2.27}$$

where F denotes the filtered values and γ is the Asselin coefficient, with a value of 0.1 in the experiments used in this thesis.

For diffusive processes, such as horizontal diffusion and tracer restoring terms, a forward time stepping scheme is used. The Leapfrog scheme cannot be used for these processes because the coefficients of the even derivative terms are zero. The forward scheme is given by:

$$x^{t+\Delta t} = x^{t-\Delta t} + 2\Delta t D_x^{t-\Delta t} \tag{2.28}$$

where D denotes the diffusive term. This scheme is conditionally stable. For horizontal tracer (Laplacian) and momentum diffusion (bilaplacian) the conditions for stability are (Griffies, 2004)

$$A^h < \begin{cases} \frac{e^2}{8\Delta t} & \text{Laplacian diffusion} \\ \frac{e^4}{64\Delta t} & \text{bilaplacian diffusion} \end{cases} \tag{2.29}$$

where A^h is the mixing coefficient, and e is the largest horizontal grid size. For $1/4^\circ$ horizontal resolution, we use a baroclinic time step of 1080 s. The largest grid cell is 27,799.7 m. Using Equation 2.29, the upper bound for A^h is then $A^h < 8.94 \times 10^4$ m^2/s for Laplacian diffusion, and $A^h < 8.64 \times 10^{12}$ m^4/s for bilaplacian diffusion. The lower bound to A^h is determined by model stability. The values for $1/12^\circ$ horizontal resolution are 5.26 $\times 10^4$ m^2/s for Laplacian diffusion and 4.98 $\times 10^{11}$ m^4/s for bilaplacian diffusion.

An implicit backward time stepping scheme is used for vertical diffusion, and is given as

$$x^{t+\Delta t} = x^{t-\Delta t} + 2\Delta t RHS_x^{t+\Delta t} \tag{2.30}$$

This scheme is unconditionally stable.

2.2 The White Ocean

The white ocean used in NEMO is the Louvain-la-Neuve sea ice model (LIM2; Fichefet and Maqueda, 1997), which describes the dynamic and thermodynamic processes of sea ice. LIM2 represents sea ice with three layers, one layer of snow on the top, and two equal-thickness ice layers below (Semtner, 1976). Sea ice in each grid cell is described by one of two ice thickness categories, open water or a homogeneous slab of ice, with a mean ice thickness.

2.2.1 Sea ice dynamics

The model sea ice momentum balance is

$$\frac{\partial \boldsymbol{u}}{\partial t} = \underbrace{A\boldsymbol{\tau}_a m^{-1}}_{\text{Atmospheric stress}} + \underbrace{A\boldsymbol{\tau}_o m^{-1}}_{\text{Ocean stress}} - \underbrace{f\boldsymbol{k}\times\boldsymbol{u}}_{\text{Coriolis force}} - \underbrace{g\nabla\eta}_{\text{SSH tilt}} + \underbrace{m^{-1}\nabla\cdot\sigma}_{\text{Rheology}} \tag{2.31}$$

where m is mass per unit area of ice and snow, $\boldsymbol{u}$ is ice velocity, f is the Coriolis parameter, A is ice concentration, $\boldsymbol{k}$ is the vertical unit vector, and g is gravity. Sea surface height is represented by η, while $\nabla\cdot\sigma$ denotes the internal stress. Stress from the atmosphere (denoted by the subscript a) and ocean (shown by the subscript o) are represented by $\boldsymbol{\tau}_a$ and $\boldsymbol{\tau}_o$ respectively. As shown by Thorndike (1986), advection of momentum can be neglected on time scales greater than 30 minutes, which is the case here.

Stress from the atmosphere in the form of wind, and stress from the ocean in the form of currents are defined as

$$\boldsymbol{\tau}_a = \rho_a C_a |\boldsymbol{u}_a| \boldsymbol{u}_a \tag{2.32}$$

$$\boldsymbol{\tau}_o = \rho_o C_o |\boldsymbol{u}_o - \boldsymbol{u}_i| (\boldsymbol{u}_o - \boldsymbol{u}_i) \tag{2.33}$$

where $\boldsymbol{u}$ is the velocity of ice ($\boldsymbol{u}_i$), ocean surface currents ($\boldsymbol{u}_o$), and surface wind ($\boldsymbol{u}_a$, at 10 m height). Similarly, ρ_o is the seawater density, and ρ_a is the air density. Drag coefficients for both ocean and air are denoted by $C_o = 0.0055$ and C_a accordingly. The CORE bulk formula from Large and Yeager (2004) is used to compute the air drag coefficient.

For the last term in Equation 2.31, internal ice stress, the Elastic-Viscous-Plastic (EVP)

approach is used, where on short time scales sea ice behaves more elastically, and on longer times scales (on the order of days), the sea ice behaviour is simplified to viscous-plastic rheology (Hunke, 2001; Hunke and Dukowicz, 1997), which also considers the state of the ice (i.e. ice thickness and ice concentration). The horizontal internal ice stress is

$$\nabla_h \cdot \sigma = (\frac{\partial \sigma_1}{\partial x}, \frac{\partial \sigma_2}{\partial y}) \tag{2.34}$$

$$\sigma_1 = \sigma_{11} + \sigma_{22} \tag{2.35}$$

$$\sigma_2 = \sigma_{11} - \sigma_{22} \tag{2.36}$$

Sea ice divergence (D_D), and horizontal tension (D_T) and shearing (D_S) strain rates are given by

$$D_D = \frac{1}{e_1 e_2}\Big(\frac{\partial(e_2 u)}{\partial i} + \frac{\partial(e_1 v)}{\partial j}\Big) = \dot{\epsilon}_{11} + \dot{\epsilon}_{22} \tag{2.37}$$

$$D_T = \frac{1}{e_1 e_2}\left(e_2^2 \frac{\partial(\frac{u}{e_2})}{\partial i} - e_1^2 \frac{\partial(\frac{v}{e_1})}{\partial j}\right) = \dot{\epsilon}_{11} - \dot{\epsilon}_{22} \tag{2.38}$$

$$D_S = \frac{1}{e_1 e_2}\left(e_1^2 \frac{\partial(\frac{u}{e_1})}{\partial j} + e_2^2 \frac{\partial(\frac{v}{e_2})}{\partial i}\right) = 2\dot{\epsilon}_{12} \tag{2.39}$$

where $\dot{\epsilon}_{11}$, $\dot{\epsilon}_{22}$, and $\dot{\epsilon}_{12}$ are from the symmetric strain rate tensor matrix (Hunke, 2001). At shorter time scales when sea ice has an elastic response, the internal stress tensor relates to the strain rate through the following:

$$\frac{1}{E}\frac{\partial \sigma_1}{\partial t} = D_D - \frac{\sigma_1 \Delta}{P} - \Delta \tag{2.40}$$

$$\frac{1}{E}\frac{\partial \sigma_2}{\partial t} = D_T - \frac{\sigma_2 e^2 \Delta}{P} \tag{2.41}$$

$$\frac{1}{E}\frac{\partial \sigma_{12}}{\partial t} = \frac{1}{2}D_S - \frac{\sigma_{12} e^2 \Delta}{P} \tag{2.42}$$

$$\Delta = \sqrt{D_D^2 + \frac{1}{e^2}(D_T^2 + D_S^2)} \tag{2.43}$$

where E is the modulus of elasticity (Young's modulus), e is the eccentricity of the sea ice elliptical curve, and P is ice strength (a function of both ice thickness and concentration)

$$P = P^* h \exp^{-C_{reh}(1-A)} \tag{2.44}$$

where $P^* = 5000$ N m^{-2} and $C_{reh} = 20$ are constants, and h is ice thickness. Equations

2.40 to 2.42 are arranged so the elastic component is on the left hand side, and the viscous-plastic component is on the right hand side. At longer time scales (steady state), the elastic component is 0, and one can solve for σ_{ij} as before (Hunke, 2001).

2.2.2 Sea ice thermodynamics

Processes related to sea ice growth and melt are dependent on how heat is transferred to and from the sea ice, as well as how heat is stored within the ice.

2.2.2.1 Vertical growth and decay

As mentioned previously, LIM2 describes sea ice with two equal thickness horizontal ice slabs and one snow layer. To determine the rates of ice melt/growth at the top and bottom of sea ice, we first need to know the heat storage in the system. We use a one-dimension heat diffusion equation of the form

$$\rho C_p \frac{\partial T}{\partial t} = Gk \frac{\partial^2 T}{\partial z^2} \tag{2.45}$$

where T is temperature, and t is time. The components specific to the snow or ice are the density ρ, thermal conductivity k, and C_p representing the specific heat. G is a correction factor because heat conduction varies for different ice thickness (Fichefet and Maqueda, 1997).

At the surface of the snow–ice system, the heat budget is given as

$$B_{si}(T_{si}) = Q_{sw} + Q_{lw} + Q_h + Q_{le} + Q_{cs} \tag{2.46}$$

where the heat balance, B_{si}, is a function of the temperature at the surface (T_{si}), and is equal to the sum of sensible (Q_h) and latent (Q_{le}) heat fluxes, conductive heat flux from below (Q_{cs}), and shortwave (Q_{sw}) and longwave (Q_{lw}) radiation. Bulk formula from Large and Yeager (2004) are used to calculate the radiation fluxes, and sensible and latent heat fluxes as follows

$$Q_{sw} = (1 - i_0)(1 - \alpha)Q_{ds} \tag{2.47}$$

$$Q_{lw} = \epsilon(Q_{dl} - \sigma SST^4) \tag{2.48}$$

$$Q_h = \rho_a c_p C_h (T_a - SST)|\mathbf{u}_a - \mathbf{u}_o| \tag{2.49}$$

$$Q_{le} = \rho_a L_e C_e (q_a - q_s)|\mathbf{u}_a - \mathbf{u}_o| \tag{2.50}$$

where i_0 is the fraction of the net shortwave radiation that goes through the snow-ice, α is albedo, Q_{ds} (Q_{dl}) is the downward directed atmospheric shortwave (longwave) radiation, emissivity is represented by ϵ, and the Stephan–Boltzmann constant is $\sigma = 5.67 \times 10^{-8}$ W m^{-2} K^{-4}. Transfer coefficients of latent and sensible heat are given by C_h and C_e respectively. $L_e = 2.5 \times 10^6$ J kg^{-1} is the latent heat of vaporization, and finally, q_a, T_a, and SST denote the specific humidity, air temperature (at 10 m), and sea surface temperature, while q_s is the specific humidity at the surface. Surface melting will occur when the surface temperature is larger than the melting point, and is given by

$$\left(\frac{\partial h_*}{\partial t}\right)_{ai} = \frac{B_{si}}{L_*} \tag{2.51}$$

where the latent heat of fusion is L_*, with the subscript being either s or i depending on the presence of snow, and h_* denotes the ice or snow thickness.

At the bottom of the sea ice, where the sea ice and ocean come into contact, the heat balance is between the heat flux from the ocean (Q_{oi}) and the conductive heat flux at the ice bottom (Q_{cb}), and is mathematically written as

$$\left(\frac{\partial h_i}{\partial t}\right)_{oi} = \frac{Q_{cb} - Q_{oi}}{L_i} \tag{2.52}$$

Thus, when Q_{cb} is larger than Q_{oi}, ice growth occurs.

2.2.2.2 Lateral growth and decay

Sea ice concentration (A) defines the percentage of a grid cell that is covered by ice, as smaller scale features, such as polynyas, need to be represented. Lateral sea ice growth depends on the open water heat budget, B_l, in the form

$$\frac{\partial A}{\partial t} = (1 - A^2)^{1/2} \frac{(1 - A) B_l}{L_i h_o} \tag{2.53}$$

where h_0 is the thickness of ice formed in a polynya or on the side of the existing ice floe. When B_l is negative, there is ice formation, and when B_l is positive there is ice melt.

2.3 Ice-Ocean coupling

The ice and ocean models must be coupled together because sea ice processes impact the surface boundary conditions in the ocean model, and the ocean model impacts the sea ice through heat and momentum exchange. The shortwave radiation flux (Q_{swoc}) at the ocean surface with sea ice cover is

$$Q_{swoc} = AQ_{str} + (1-A)(1-\alpha_w)Q_{ds} \tag{2.54}$$

$$Q_{str} = i_0(1-\alpha)Q_{ds}\exp^{(-1.5(h_i-0.1))} \tag{2.55}$$

where Q_{str} is the amount of shortwave radiation that penetrates the ice slab and reaches the ocean surface, and α is the open water albedo.

When ice is present, the temperature in the ocean mixed layer, a homogeneous layer in both temperature (T_m) and salinity (S_m) at the ocean surface, is set to the freezing temperature (T_{fw}) which is dependent on salinity. Therefore, the heat balance in the upper ocean is based on the heat gain of the mixed layer and the sensible heat flux from the ocean to the sea ice, Q_{oi}. The ocean to ice sensible heat flux is defined as

$$Q_{oi} = (1-i_w|_{z=-h_m})Q_{str} + \Gamma\left[\frac{(1-A)B_l}{A}\right] + Q_{ent} + Q_{dif} + Q_{ovT}|_{-h_m} + Q_{fus} \tag{2.56}$$

where h_m is the depth of the mixed layer, the fraction of shortwave radiation reaching the ocean is given as i_w and is a function of depth. The Heaviside unit function is represented as Γ, and the diffusion, entrainment, salinity changes, and overturning heat fluxes are denoted by $Q_{dif}, Q_{ent}, Q_{fus}$, and Q_{ovT} respectively. The ocean mixed layer model calculates these last four terms.

The heat flux budget of open water areas, such as polynyas, is

$$\begin{aligned} B_l =& (1-i_w|_{-h_m})(1-\alpha_w)Q_{sw} + \epsilon_w(Q_{lw} - \sigma T_m^4) + Q_h + Q_{le} \\ &+ Q_{lsi} - Q_{lpr} + Q_{ent} + Q_{dif} + Q_{ovT}|_{-h_m} + Q_{fus} \end{aligned} \tag{2.57}$$

where Q_{lsi} is the latent heat released during snow/ice formation, and Q_{lpr} is the latent heat release associated with snow falling on the open ocean. As the main focus of this thesis is on

freshwater, the salt flux at the ocean surface is given as

$$Q_{salt} = \underbrace{S_m \frac{\partial m_s}{\partial t}}_{\text{snow melt}} + \underbrace{(S_m - S_i)\frac{\partial m_i}{\partial t}}_{\text{ice melt}} + \underbrace{S_i \frac{\partial m_s}{\partial t}}_{\text{artificial meteoric ice}} + \underbrace{(S_m - S_i)\Big(\frac{\partial m_s}{\partial t} + \frac{\partial m_i}{\partial t}\Big)}_{\text{salt rejection}} + \underbrace{S_m(AE - P_w)}_{\text{evaporation and precipitation}} \tag{2.58}$$

where E is evaporation over polynyas and leads, P_w the freshwater change from precipitation, m denotes mass of ice (m_i) or snow (m_s), and S_i is the salinity of the sea ice. The artificial meteoric ice term is included so as to provide salinity to the meteoric ice. The salt rejection term also includes the impact of snow ice formation.

Bibliography

Asselin, R. (1972). Frequency Filter for Time Integrations. *Monthly Weather Review*, 100(6):487–490.

Bernard, B., Madec, G., Penduff, T., Molines, J.-M., Treguier, A.-M., Le Sommer, J., Beckmann, A., Biastoch, A., Böning, C., Dengg, J., Derval, C., Durand, E., Gulev, S., Remy, E., Talandier, C., Theetten, S., Maltrud, M., McClean, J., and De Cuevas, B. (2006). Impact of partial steps and momentum advection schemes in a global ocean circulation model at eddy-permitting resolution. *Ocean Dynamics*, 56(5/6):543 – 567.

Blanke, B. and Delecluse, P. (1993). Variability of the Tropical Atlantic Ocean Simulated by a General Circulation Model with Two Different Mixed-Layer Physics. *Journal of Physical Oceanography*, 23(7):1363–1388.

Bougeault, P. and Lacarrere, P. (1989). Parameterization of orography-induced turbulence in a mesobeta-scale model. *Monthly Weather Review*, 117(8):1872 – 1890.

Deremble, B., Hogg, A. M., Berloff, P., and Dewar, W. (2011). On the application of no-slip lateral boundary conditions to 'coarsely' resolved ocean models. *Ocean Modelling*, 39(3/4):411 – 415.

Eby, M. and Holloway, G. (1994). Grid transformation for incorporating the Arctic in a global ocean model. *Climate Dynamics*, (4-5):241.

Fichefet, T. and Morales Maqueda, M. (1997). Sensitivity of a global sea ice model to the treatment of ice thermodynamics and dynamics. *Journal of Geophysical Research*.

Gaspar, P., Gregoris, Y., and Lefevre, J. (1990). A simple eddy kinetic-energy model for simulations of the oceanic vertical mixing - Tests at station Papa and long-term upper ocean study site. *Journal of Geophysical Research: Oceans*, 95(C9):16179 – 16193.

Griffies, S. M. (2004). *Fundamentals of ocean climate models*. Princeton, N.J. : Princeton University Press.

Hunke, E. C. (2001). Viscous–plastic sea ice dynamics with the EVP model: Linearization issues. *Journal of Computational Physics*, 170(1):18 – 38.

Hunke, E. C. and Dukowicz, J. K. (1997). An Elastic–Viscous–Plastic model for sea ice dynamics. *Journal of Physical Oceanography*, 27(9):1849–1867.

Large, W. and Yeager, S. (2004). Diurnal to Decadal Global Forcing For Ocean and Sea-Ice Models: The Data Sets and Flux Climatologies. NCAR/TN-460+STR NCAR Technical Note, National Center for Atmospheric Research.

Madec, G., Delécluse, P., Imbard, M., and Lévy, C. (1998). OPA 8.1 Ocean General Circulation Model reference manual. *Note du Pole de Modélisation*, 11:91p.

Madec, G. and the NEMO team (2008). NEMO ocean engine. *Note du Pole de Modélisation*, (No 27 ISSN No 1288-1619).

Mesinger, F., Arakawa, A., and Global Atmospheric Research Programme, G. (1976). *Numerical Methods Used in Atmospheric Model*, volume 17 of *GARP publications series*. Global Atmospheric Research Programme, GARP.

Murray, R. (1996). Explicit generation of orthogonal grids for ocean models. *Journal of Computational Physics*, (2):251.

Robert, A. J. (1966). The Integration of a Low Order Spectral Form of the Primitive Meteorological Equations. *Journal of the Meteorological Society of Japan. Ser. II*, 44(5):237–245.

Roberts, J. L., Heil, P., Murray, R. J., Holloway, D. S., and Bindoff, N. L. (2006). Pole relocation for an orthogonal grid: An analytic method. *Ocean Modelling*, 12(1/2):16 – 31.

Roullet, G. and Madec, G. (2000). Salt conservation, free surface, and varying levels; a new formulation for ocean general circulation models. *Journal of Geophysical Research*, 105(C10):23.

Semtner, A. (1976). A model for the thermodynamic growth of sea ice in numerical investigations of climate. *Journal of Physical Oceanography*, pages 379 – 389.

Stull, R. B. (1988). *An Introduction to Boundary Layer Meteorology.* Dordrecht: Kluwer Academic Publishers.

Thorndike, A. S. (1986). *Kinematics of Sea Ice*, pages 489–549. Springer US, Boston, MA.

Chapter 3

Sensitivity of freshwater dynamics to ocean model resolution and river discharge forcing in the Hudson Bay Complex

Published in Journal of Marine Systems (April 2019). DOI: 10.1016/j.jmarsys.2019.04.002
Natasha A. Ridenour, Xianmin Hu, Shabnam Jarfari Khasragh, Jack C. Landy, Jennifer V. Lukovich, Tricia A. Stadnyk, Kevin Sydor, Paul G. Myers, David G. Barber

I did the analysis, the majority of the model evaluation, runoff remapping, writing, and ran two of the four experiments. X. Hu ran the remaining two experiments, taught and guided me how to remap the runoff, and provided assistance on some calculations. S. Jafari Khasragh provided the spatial sea surface temperature plots. Sea ice thickness data was provided by J.C. Landy along with input regarding the data. J.V. Lukovich provided the ice drift vector plots along with some writing on the plots. T.A. Stadnyk provided two HYPE river discharge datasets. P.G. Myers provided advice, guidance, and, along with K. Sydor, D.G. Barber, and all co-authors, provided manuscript edits.

Abstract

Hydroelectric development and regulation have modified the temporal and spatial distribution of runoff entering the Hudson Bay Complex (HBC). To understand the impacts and future of regulation in this region, the numerical ocean model, NEMO, run with the Arctic and Northern Hemispheric Atlantic (ANHA) configuration, is used to model present day freshwater dynamics associated with river runoff and sea ice melt. The present work establishes the freshwater budget in each subregion of the HBC, in addition to evaluating the sensitivity to model resolution and estimates of river discharge forcing. It is shown that the annually averaged HBC freshwater budget is mainly a balance between river discharge and freshwater advected out of the region, while surface fluxes (ice melt and growth, and precipitation and evaporation) are the dominant term on seasonal time scales. Runoff forcing is found to impact the long term mean volume and freshwater fluxes out of the HBC, while increased resolution has minimal effect on these fluxes, with the exception of the Southampton–Baffin Island gate. Quantitative estimates of turbulent, mean, and Ekman components of freshwater exchange between the interior and boundary regions of Hudson Bay are also presented. We use offline Lagrangian passive tracers to estimate the HBC runoff residence time, which is as long as 32 years.

3.1 Introduction

Anthropogenic changes such as global warming, which is causing an intensification of the hydrological cycle in the Arctic region (Déry et al., 2009; Zhang et al., 2012), as well as hydroelectric development, are changing the river discharge in northern Canada (Déry et al., 2018, 2011, 2016; MacDonald et al., 2018). One such region undergoing these changes is the Hudson Bay Complex (HBC), which includes Hudson Bay, James Bay, and neighbouring basins, Foxe Basin, and Hudson Strait and Ungava Bay, shown in Figure 3.1. The HBC receives about 900 km^3/year of river runoff, equivalent to roughly three times the Mackenzie River (Holmes et al., 2012; Shiklomanov and Shiklomanov, 2003), causing this region to be quite fresh compared to the Arctic Ocean. The main pathway of heat, mass, and freshwater exchange between the HBC, the Arctic, and the North Atlantic is via Hudson Strait. This river

water flows out of Hudson Strait and along the coast of Labrador in the Labrador Sea, where deep convection occurs (Aagaard and Carmack, 1989; Lazier et al., 2002; Lozier et al., 2019; Straneo, 2006). The role of the fresh Hudson Strait outflow in these processes, however, is still largely unknown. This study aims to provide multi-year estimates of the HBC freshwater budget, so as to understand the role of model resolution and river discharge on freshwater fluxes within the HBC as well as to the North Atlantic.

Isolated from large scale ocean circulation, the main sources of freshwater to the HBC are river discharge and sea ice melt (Prinsenberg, 1988). On time scales less than a year, sea ice melt/growth has a much larger role in the freshwater budget compared to river discharge (Prinsenberg, 1988). Freshwater sourced from river discharge is found mainly along the coast, while freshwater from sea ice melt is distributed more equally around the bay (Granskog et al., 2011, 2007).

Spatially, the distribution of freshwater within Hudson Bay can be divided into two regions, the outer boundary region and the interior region. The exchange of freshwater between the interior and boundary regions is mainly driven by Ekman transport (St-Laurent et al., 2011). In summer, the freshwater is imported into the interior, and is released during the fall (St-Laurent et al., 2012).

In the context of climate change, the length of the ice free season in the HBC is increasing, with both earlier break up in spring (Castro de la Guardia et al., 2017; Gagnon and Gough, 2005; Gough et al., 2004a; Hochheim and Barber, 2014; Kowal et al., 2017) and later freeze up in the fall (Castro de la Guardia et al., 2017; Gagnon and Gough, 2005; Hochheim and Barber, 2014; Kowal et al., 2017). These changes have been found to be related to the region's air temperature (Hochheim and Barber, 2014; McGovern and Gough, 2015). Hochheim and Barber (2010) found, for every 1°C increase in the region's mean air temperature, it can result in a decrease of 105,000–117,000 km^2 in late November sea ice extent with concentrations greater than 80%. Sea ice thickness, on the other hand, is weakly related to air temperatures (Gough et al., 2004b). Ice thickness derived from satellite altimetry (Landy et al., 2017) shows a significantly asymmetrical spatial pattern across Hudson Bay in spring due to the strong cyclonic ice drift in winter. Their study also estimated 742 $\pm$10 km^3 of freshwater is stored in sea ice within the bay in April.

Anthropogenic influences have also impacted the HBC river discharge. Discharge entering the HBC has increased (Déry et al., 2016), which is associated with the intensified hydrological cycle in the context of Arctic warming (Déry et al., 2009, 2011, 2016; Rawlins et al., 2010; Zhang et al., 2012). Seasonally, hydroelectric development has increased winter HBC streamflow (Déry et al., 2011). Increasing air temperature also leads to earlier spring peak runoff (Déry et al., 2005; Gagnon and Gough, 2002), however, this varies regionally (Gagnon and Gough, 2002). Under the 1.5° and 2°C future warming scenarios, MacDonald et al. (2018) found discharge increased in all seasons, except summer, with the largest increases occurring in spring.

In light of these current trends, it is still unclear as to the impact that these changes will have on the freshwater dynamics in this region. The annual net freshwater flux of river discharge is large, thus, changes in river runoff, by seasonal and spatial redistribution, or long term trends, lead to changes in seawater density and stability. A high runoff year and regulated discharge have been shown to lead to a decrease in salinity, along with a general increase in sea ice thickness (Saucier and Dionne, 1998).

To date, there have been no multi-year evaluations of the freshwater budget in this region. Other questions remain regarding the freshwater budget, for instance, how important are small scale processes in HBC dynamics? Does the freshwater budget change with changes in river runoff? To determine the sensitivity of the HBC to runoff forcing as well as model resolution, we use a general circulation ocean model coupled with a sea ice model to evaluate the freshwater budgets, pathways, and boundary-interior exchange processes of each simulation. The following section contains a description of the model, as well as the various datasets used in the numerical experiments. In Section 3.3, an evaluation of the model and the freshwater budgets for each subregion in the HBC, as well as boundary-interior freshwater exchanges and riverine water residence time, are shown. Our analysis of the residence time is in Section 3.3.4, preceding the summary and conclusions. This work is part of the BaySys project, a bay-wide initiative to investigate effects of hydroelectric regulation and climate change on various aspects of the Hudson Bay environment, such as the biogeochemical, biological, and physical components of the system.

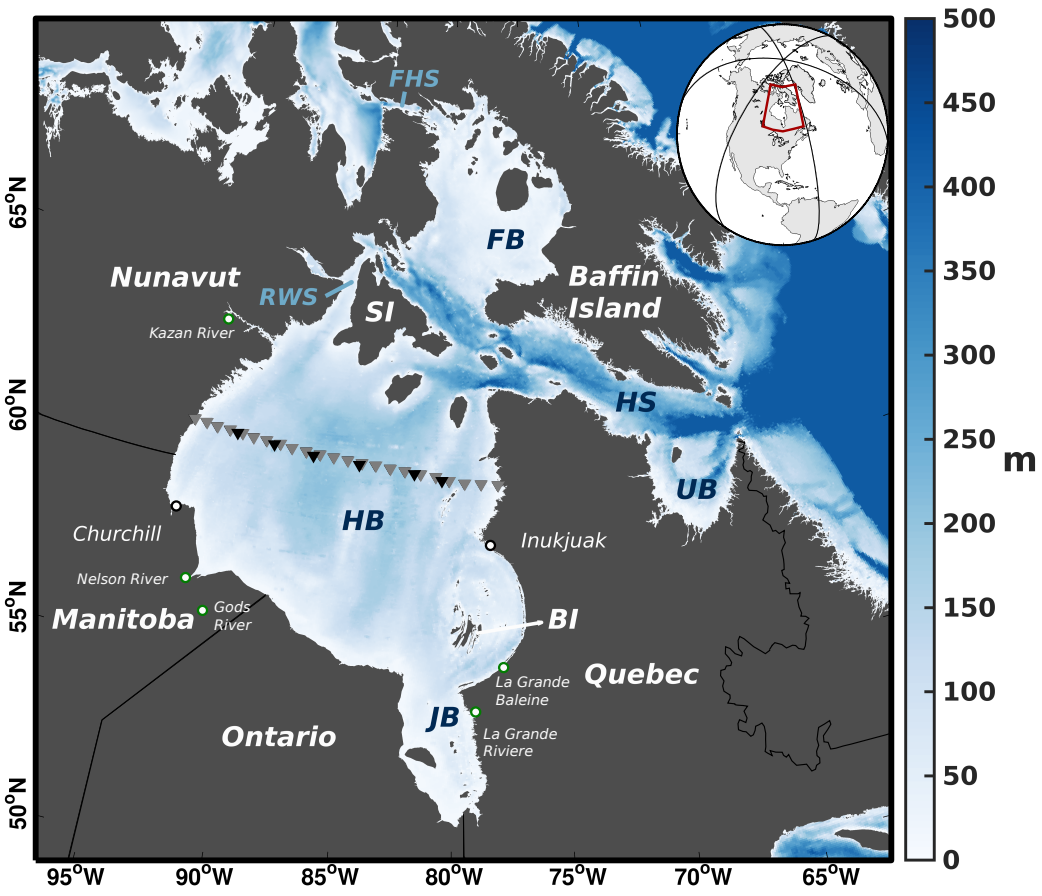

Figure 3.1: Bathymetry of the Hudson Bay Complex (HBC). Abbreviations for geographic locations and features are as follows: FB = Foxe Basin, HS = Hudson Strait, UB = Ungava Bay, HB = Hudson Bay, JB = James Bay, SI = Southampton Island, FHS = Fury and Hecla Strait, RWS = Roes Welcome Sound, and BI = Belcher Islands. The towns of Inukjuak and Churchill are shown by the black rimmed circles, while river outlets are shown by green rimmed circles. Grey triangles show the model transect, and black triangles show observations, used for Figure 3.5.

3.2 Methods and Data

3.2.1 Numerical Model

We use a general circulation ocean model, based on the Nucleus for European Modelling of the Ocean version 3.4 (NEMO; Madec and the NEMO team, 2008), which is coupled to the sea ice model, Louvain-la-neuve Ice Model version 2 (LIM2) with elastic-viscous-plastic (EVP) rheology (Hunke and Dukowicz, 1997), and includes both thermodynamic and dynamic processes (Fichefet and Maqueda, 1997), for our simulations. We use the Arctic and Northern

Hemisphere Atlantic (ANHA) configuration, which has two open boundaries, one at Bering Strait and the other at 20°S in the Atlantic Ocean. Two horizontal resolutions are used in our study, ¼° (ANHA4) and 1/12° (ANHA12) (Dukhovskoy et al., 2016; Gillard et al., 2016; Holdsworth and Myers, 2015; Hu et al., 2018; Müller et al., 2017), meaning the resolution within the HBC is 10–17 km for ANHA4 (Figure 3.2a), and 3.5–5.5 km for ANHA12 (Figure 3.2b). Vertically, there are 50 geopotential levels that have the highest resolution at the surface and decrease in resolution with increasing depth. For the vertical mixing scheme, we use a turbulent kinetic energy (TKE) turbulence closure scheme (Blanke and Delecluse, 1993; Bougeault and Lacarrere, 1989; Gaspar et al., 1990; Madec et al., 1998). Our simulations do not use temperature or salinity restoring so as to not damp the freshwater signals. Tides are also not included in these simulations as we will focus on large scale processes. We use 5-day averaged output from the model for our analysis, however, the time step for each resolution is 1080 seconds and 180 seconds for ANHA4 and ANHA12 respectively.

Our simulations are initialized with 2D (sea surface height and sea ice) and 3D (temperature, salinity, and horizontal velocities) fields from GLobal Ocean ReanalYsis and Simulations (GLORYS2v3) produced by Mercator Ocean (Masina et al., 2015). Boundary conditions, such as salinity, temperature, and ocean velocities are also provided by the GLORYS2v3 dataset. We use atmospheric forcing from the Canadian Meteorological Centre's (CMC) global deterministic prediction system (GDPS) reforecasts (CGRF) described in Smith et al. (2014), along with CORE bulk formulae (Large and Yeager, 2004). This dataset provides 2 m air temperature and specific humidity, 10 m wind, downwelling shortwave and longwave radiation flux, and total precipitation to the surface at high temporal (hourly) and spatial (33 km) resolution. We integrate our simulations from January 2002 to December 2016. Monthly interannual runoff (described more in Section 3.2.2), as well as Greenland melt water provided by Bamber et al. (2012) is also carefully remapped onto the model grid to have more realistic freshwater input from land to ocean. The temperature of discharge when entering the ocean is given the same temperature as the surrounding seawater, a typical approach of ocean general circulation models when no reliable discharge temperature is available.

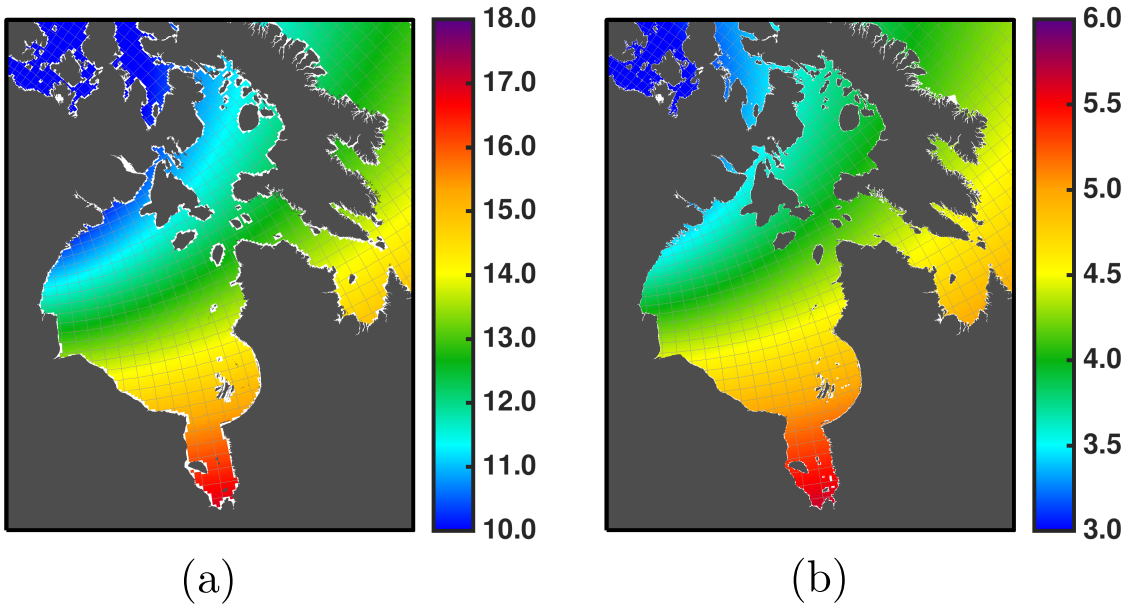

Figure 3.2: (a) ANHA4 and (b) ANHA12 configuration mesh for the HBC (every 5^{th} and 15^{th} mesh grid respectively), with colours showing model horizontal resolution in kilometers.

3.2.2 Runoff Datasets

To test the model sensitivity to runoff forcing, we use three river discharge datasets: corrected Dai and Trenberth (referred to as DT; Dai et al., 2009; Dai and Trenberth, 2002), and two products from HYdrological Predictions for the Environment (HYPE; Andersson et al., 2013; Gelfan et al., 2017; Lindström et al., 2010) provided by BaySys Team 2. In this case, the HYPE model simulates streamflow for 398 streams and rivers draining into the HBC. One of the HYPE datasets used here is uncalibrated HYPE simulated streamflow that has been integrated with observed streamflow. Where observations are available, HYPE discharge is replaced with gap-filled observations from Déry et al. (2016). We also note that observed discharge for La Grande Riviere (second largest river by volume) was not used, and the uncalibrated HYPE model underestimates La Grande Riviere discharge. Thus, for the purposes of this study, this integrated, uncalibrated version of HYPE discharge will be referred to as HIUC. The second HYPE streamflow product used is from the calibrated version of HYPE, which we will refer to as HCAL. This runoff dataset has not been integrated with observations, but includes the improvements to the model, such as better representation of La Grande Riviere discharge and Nelson River regulated discharge. HCAL and HIUC discharge extends to 2013 and 2010

respectively. We use the final year as forcing for the remaining years up to 2016. This is also the case for DT, which ends in December 2007. For consistency, throughout the study we compare the two HYPE datasets to DT, as DT is the standard river discharge dataset used for forcing ocean models. DT interannual runoff is used for the entire configuration for the control (CTRL) and high resolution (HIRES) experiments. The HYPE datasets are used in the HBC, with DT runoff used elsewhere in the third and fourth experiments (HIUC and HCAL). All runoff datasets are prescribed as monthly averages.

The seasonal cycles of the three runoff datasets used in the HBC in this study are shown in Figure 3.3. The DT discharge is larger than the HIUC discharge in most months, due to the gap filling strategy used for the dataset, most notably during the spring freshet, with differences peaking at 1.53 km^3/day in May. The difference between DT and HCAL also peaks in May at 1.07 km^3/day. All datasets show a secondary runoff peak in the fall, with the DT dataset having a more level peak spanning September and October. Throughout the year, DT discharge averages at 2.99 km^3/day (dark blue dashed line, Figure 3.3), HIUC averages at 2.45 km^3/day (light blue dashed line), and HCAL has an annual average discharge of 2.54 km^3/day (green dashed line, Figure 3.3). This difference leads to nearly 200 km^3/yr more runoff in the DT dataset compared to HIUC, and over 150 km^3/yr compared to HCAL.

3.2.3 Residence Time Estimation

To estimate the residence time of river runoff in the HBC, we use an offline Lagrangian tool called Ariane (Blanke et al., 1999; Blanke and Raynaud, 1997) to track water parcels from major river mouths. Even though Ariane only uses advection scheme tracking, with diffusion and mixing processes partly handled by the source (numerical model) velocity fields, it has been successful in tracing pathways of given water masses (de Boisséson et al., 2012; Gillard et al., 2016; Hu and Myers, 2013; Lique et al., 2010).

In this study, Ariane particles were released in January 2004, and tracked until December 2016 in the CTRL simulation. Particles were released along the coastline where runoff forcing is applied. Our results are based on releasing 50 particles per runoff grid cell in the top 10 m of the water column, so as to mimic how runoff is dealt with in the model. Therefore, rivers with more discharge have more runoff grid cells and thus more Lagrangian floats are released.

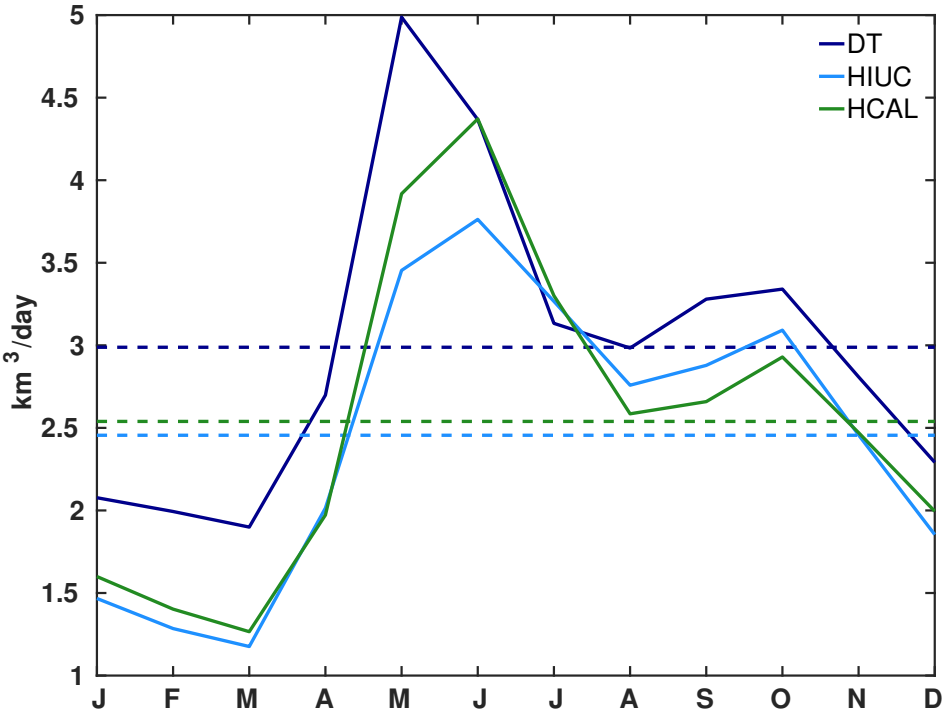

Figure 3.3: Seasonal cycle of the three runoff datasets used, averaged from 2004–2007, the common period of all datasets used, for the HBC. Dai and Trenberth discharge is represented by dark blue lines, where the solid line is the seasonal cycle and the dashed line is the mean discharge. Similarly, seasonal and mean HIUC discharge is shown by the solid and dashed light blue lines respectively, and HCAL by the green solid and dashed lines.

3.2.4 Ocean hydrological observations

To evaluate the model simulations, we used observations comprised of ArcticNet cruise data (2005, 2006, 2007, and 2010 cruises; `http://www.arcticnet.ulaval.ca/`), Marine Environmental Data Service (MEDS, now Oceanography and Scientific Data or OSD; `http://www.meds-sdmm.dfo-mpo.gc.ca/`) data from 1929–2015, and ICES Dataset on Ocean Hydrography (International Council for the Exploration of the Sea. Accessed March 14, 2016. Copenhagen, 2014. `http://www.ices.dk`) data from 1929–2016. Duplicate data in the dataset collection were removed.

Sea surface temperature (SST) data used is satellite data from the Optimum Interpolation SST (OISST) Version 2 dataset (Reynolds et al., 2007) which are available from the National Oceanic and Atmospheric Administration (NOAA) Earth System Research Laboratory Physical Science Division (ESRL/PSD). The spatial resolution of this dataset is ¼° and is based on the combination of the Advanced Very High Resolution Radiometer (AVHRR) infrared

satellite and SST observations from ships and buoys.

Ocean velocities were evaluated against altimeter products, absolute geostrophic velocity, produced by Ssalto/Duacs and distributed by Aviso with support from Cnes (`http://www.aviso.altimetry.fr/duacs/`). These data were available daily with a ¼° spatial resolution.

3.2.5 Ice Observations

We evaluated simulated sea ice drift through comparison with the low-resolution sea ice drift product of the EUMETSAT Ocean and Sea Ice Satellite Application Facility (OSI-SAF, www.osi-saf.org). With a spatial resolution of 62.5 km, and time lapse of two days, the OSI-SAF sea ice drift product combines data from daily maps of satellite signals, including brightness temperatures from passive microwave sensors, or radar backscatter from scatterometers (Lavergne et al., 2015). Uncertainty in zonal and meridional displacements is on the order of 2.5 km.

Sea ice thickness observations were obtained for the period November 2010–April 2016 from a combination of Cryosat-2 Synthetic Aperture Interferometric Radar Altimeter (SIRAL) Baseline C data and Soil Moisture and Ocean Salinity (SMOS) L-band radiometer data. The full processing chain for deriving and merging these thickness products for the HBC region is provided in Landy et al. (2017).

Simulated ice concentrations were compared to ASI Algorithm AMSR-E/AMSR2 sea ice concentration, which were obtained for 2002–2015 from the Institute of Environmental Physics (`https://seaice.uni-bremen.de/sea-ice-concentration/`), University of Bremen, Bremen, Germany (Spreen et al., 2008). AMSR-E data is used from January 2004 to October 2011, and AMSR2 data is used from July 2012 to December 2015. AMSR-E/AMSR2 ice concentration data has a horizontal resolution of 6.25 km and a temporal resolution of 1 day.

3.2.6 Reference Salinity

We use a reference salinity of 33 for our freshwater calculations as this is the most saline layer in Hudson Bay and has been used by earlier studies (Granskog et al., 2007; Prinsenberg, 1984; St-Laurent et al., 2011). The freshwater fluxes are the product of the area of the side of the

grid cell, the perpendicular velocity, and the grid cell's freshwater concentration, defined as

$$FW = \frac{S_{ref} - S}{S_{ref}} \tag{3.1}$$

where FW is the freshwater concentration. The reference salinity is represented by S_{ref} for which we use 33, and the seawater salinity as S.

3.3 Results

3.3.1 Model evaluation

To evaluate the model, we first show spatial SST for the model and observations in Figure 3.4a-j for both summer and fall. During the winter (January, February, March) and spring (April, May, June), the simulated SSTs are close to the freezing point (not shown) since the bay is ice covered. In fall, simulated SSTs (Figure 3.4a-d) agree very well with observations (Figure 3.4e). The temperature gradient from north to south in Hudson Bay is captured well by all simulations. Most simulations are too cold along the northern coast of Hudson Strait, as well as along the western coast of Foxe Basin, compared to observations.

In summer, the general pattern of the simulated SST tends to follow the observed SST pattern, with higher temperatures in James Bay and lower temperatures in northern Hudson Bay, Hudson Strait, and Foxe Basin (Figure 3.4f-j). There are some inconsistencies as well. On the large scale, simulations show colder SSTs compared to observations, such as in central Hudson Bay where SSTs are approximately 3°C colder than observations in all simulations, due to the heat flux associated with CGRF atmospheric forcing. Moreover, the coastal areas in northwestern and southwestern Hudson Bay, and in southern James Bay and Ungava Bay, show higher temperatures in all simulations compared to observations. Along the eastern shore of Hudson Bay, all simulations are colder than observations, with the exception of northeast of the Belcher Islands.

Figure 3.4k-o shows the spatial distribution of the top 100 m averaged salinity for observations and four experiments. Observations from July–September are shown, while only August is shown for model experiments. This was done because the majority of observations were taken in August (450,000 measurements from all depths), but a significant number of obser-

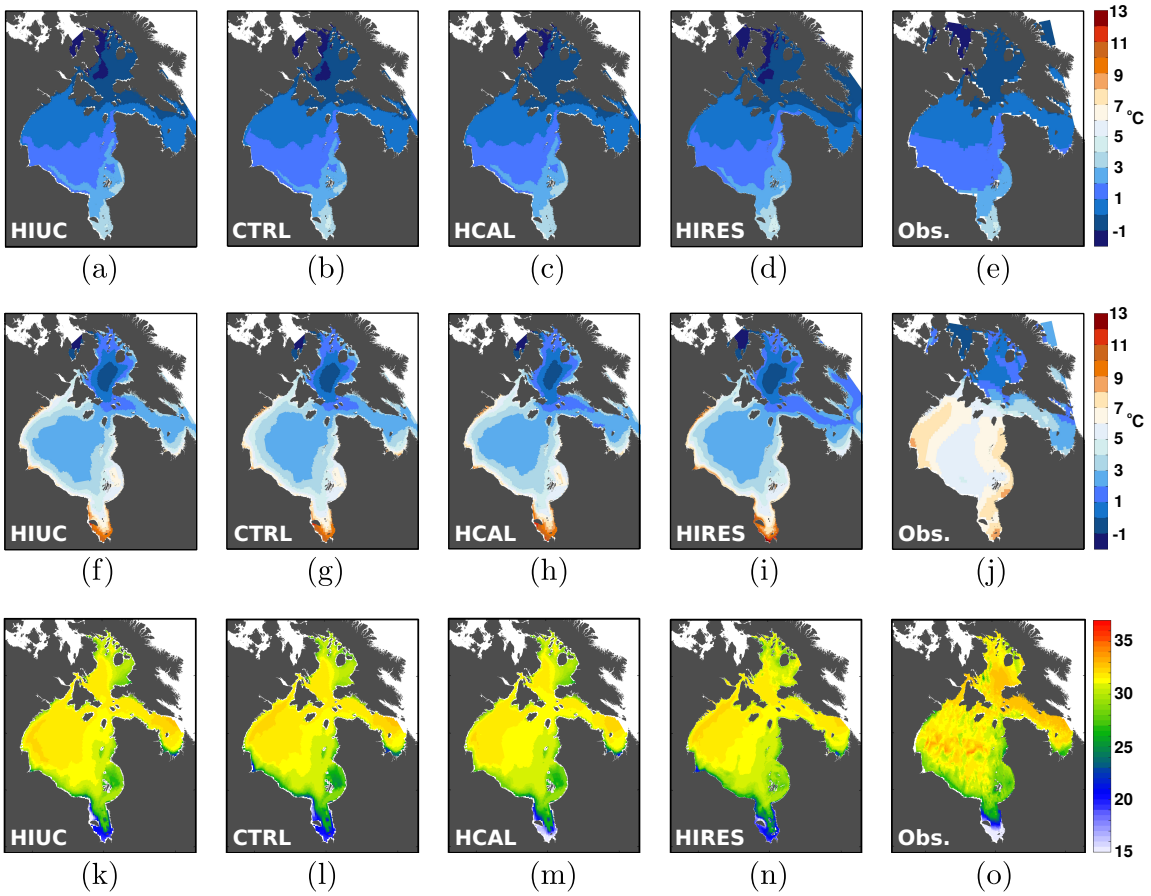

Figure 3.4: Fall (October, November, December) SST for four model experiments (a) HIUC, (b) CTRL, (c) HCAL, (d) HIRES, and (e) observations. Summer (July, August, September) SST for four model experiments (f) HIUC, (g) CTRL, (h) HCAL, (i) HIRES, and with observations shown in (j). The bottom panel shows top 100 m mean salinity for August 2004–2016 for model experiments (k) HIUC, (l) CTRL, (m) HCAL, and (n) HIRES, and in (o) available gridded July–September observations.

vations were taken in July and September (25,000 and 200,000 measurements respectively), which were included for more spatial coverage. All four model experiments capture the higher salinities in the center of Hudson Bay, western Foxe Basin, and the northern coast of Hudson Strait. The experiments also reproduce the low salinities observed along the southern coast of Hudson Bay, and in James Bay. Smaller features, such as low salinities east of the Belcher Islands, north of Inukjuak, eastern Foxe Basin, and southern Ungava Bay are also captured by the experiments.

Data from an ArcticNet Cruise in September 2006 (`http://www.arcticnet.ulaval.ca/`) were used to compare a west–east cross section in Hudson Bay with the model simulations

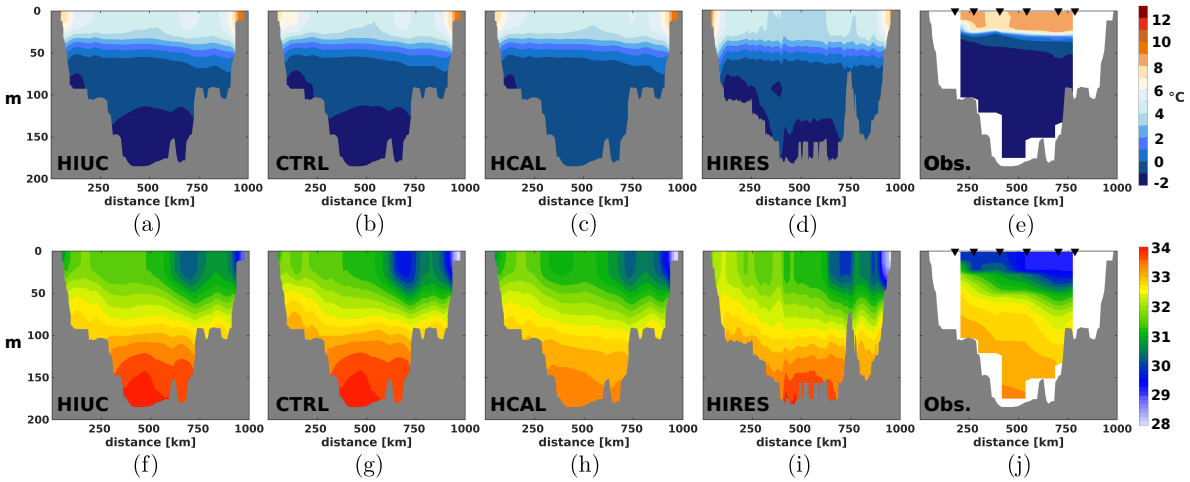

Figure 3.5: Mean temperature and salinity cross sections for the (a,f) HIUC, (b,g) CTRL, (c,h) HCAL, and (d,i) HIRES simulations for September 8–12, 2006. Observations (e,j) shown are from a transect spanning from September 8–10, 2006. The x–axis shows the distance in kilometers from the western coast, and observed profiles were taken at the points marked with black triangles shown in Figure 3.1.

(Figure 3.5). Observations show warmer surface temperatures and cooler temperatures at depth (Figure 3.5e) compared to all model simulations (Figure 3.5a-d). This could be due to an issue with the air-sea fluxes or that the model uses 5-day averages, instead of single point measurements at a given time. Another possible explanation for this discrepancy is that the model overestimates vertical mixing. All model simulations show warmer surface temperatures along the coast, which is not available in the observations. The depth of the mixed layer in model simulations, around 40 m, is close to the observed mixed layer depth seen in Figure 3.5e. The transition between the warm surface waters and the cooler waters at depth is more abrupt in observations compared to the model simulations as well.

Figure 3.5f-i shows salinity along the same west–east cross section in Hudson Bay for the HIUC, CTRL, HCAL, and HIRES simulations. Bathymetry is different in the HIRES simulation due to the higher resolution. Three of the four simulations show salinities higher than 33.5 at the bottom, while the HCAL experiment and observed salinities do not exceed this value. In 5-day mean model output, salinities at the surface are also higher than observations, with closer agreement towards the east coast. The model captures the isohaline slopes at intermediate depths very well, which are generally at comparable depths to observations.

Aviso geostrophic currents in Figure 3.6 (red) are compared to simulated geostrophic ve-

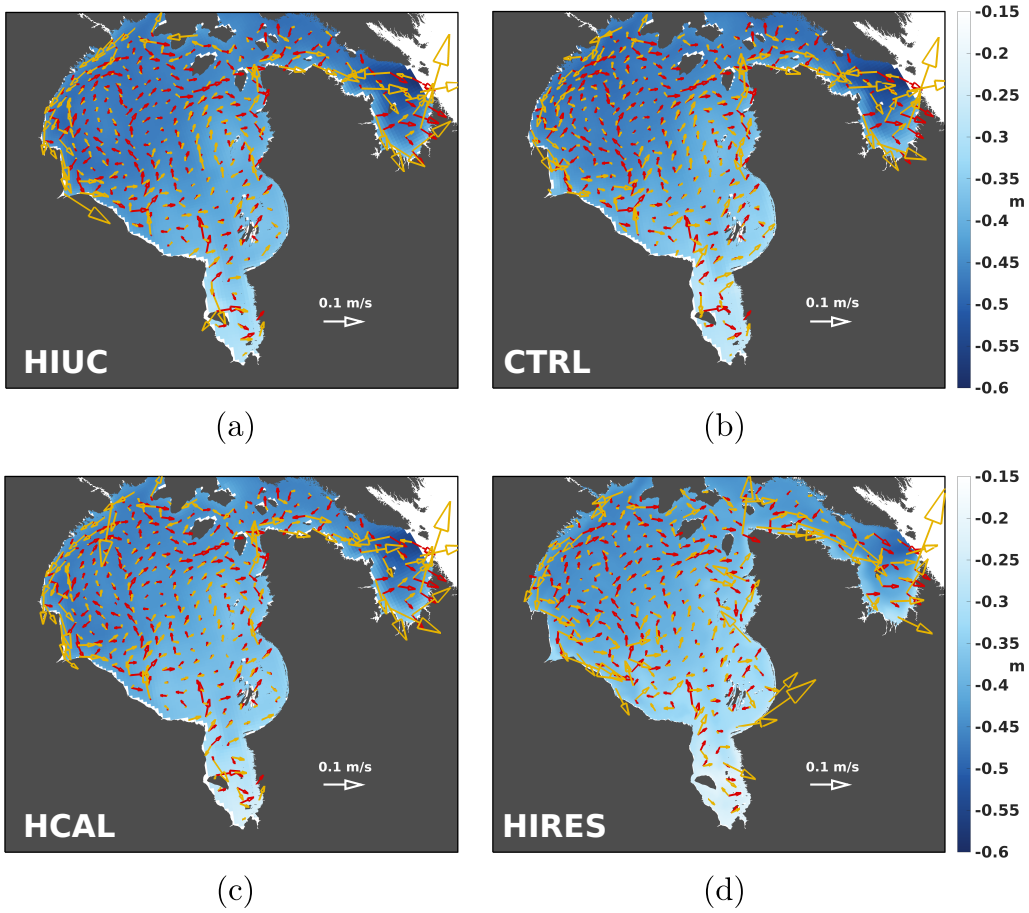

Figure 3.6: Simulated July-September mean surface geostrophic velocities (yellow) and sea surface height with Aviso vectors in red for (a) HIUC, (b) CTRL, (c) HCAL, and (d) HIRES. Velocities, both observed and simulated, were averaged over 2004–2015.

locities shown in yellow. All simulations show weaker geostrophic velocities in central Hudson Bay compared to the Aviso geostrophic velocities. In all cases, flow along the southern coast of Hudson Strait is stronger in the model than observations, as well as along the western Hudson Bay coast. This discrepancy could partly be explained by Aviso's coarse resolution.

The HBC ice concentration seasonal cycle is shown in Figure 3.7a. Simulated ice concentration is less than observed in the first three months of the year, for all experiments. The HIRES experiment has the best agreement with observations for January–May. During the melt season, ice concentrations are up to 5% lower than observations, while during the ice growth season in the fall, simulated ice concentrations are significantly lower, particularly in December with an ice concentration difference of over 30%. This discrepancy can be explained by the late ice formation in the fall in our model configuration. This late ice formation is also

seen in the seasonal cycle of ice thickness (Figure 3.7b), where we have differences of over 20 cm in December, with all simulations underestimating ice thickness to the same degree. Underestimations of ice thickness continue to occur throughout the winter, however the difference between observations and the model simulations decreases in March and April. The two simulations using the DT runoff have marginally thicker ice in March compared to the two simulations that use the HYPE discharge datasets.

We focus on the model skill in capturing the sea ice growth and melt periods. Figure 3.8 (top panels) shows the mean ice concentration for April–June. Observations (Figure 3.8e) show high ice concentrations in Foxe Basin during this time, which all model simulations capture. Observations show lower ice concentrations on the northern coast of Hudson Strait, and higher concentrations along the southern coast, of up to 70%. All model simulations show too much ice in Hudson Strait, and the north-south structure is not completely captured. During this time, high ice concentrations (up to 95%) are still observed in central Hudson Bay, which is generally reproduced by the simulations as well. Finally, although with relatively high ice concentrations, the model is able to simulate the observed low ice concentration pattern (i.e., in James Bay, along the southern and eastern coasts) as well as the high ice concentration in the northwest corner of James Bay. The ice concentration within James Bay is overestimated, particularly in the ¼° simulations. It is likely attributed to the bias in local sea ice advection.

Ice concentrations during the ice growth season, from October–December, are shown in Figure 3.8f-j. As has been stated previously, the late ice formation in our model simulations is a known issue. Ice concentrations in Foxe Basin are well simulated in all model experiments. Hudson Strait has ice concentrations that are higher than observations, especially near its eastern gate, but overall model simulations are comparable to observations in this region. Larger differences between the model and observations occur in Hudson Bay. Higher ice concentrations, between 40-50%, in northwestern Hudson Bay are not captured, as well as the higher concentrations across the bay, which is due to late freeze up in the model. However, the progression of ice concentrations across the bay from east to west is captured by the model simulations.

Spatial ice thickness is shown in Figure 3.8k-o for the months January–April. The model

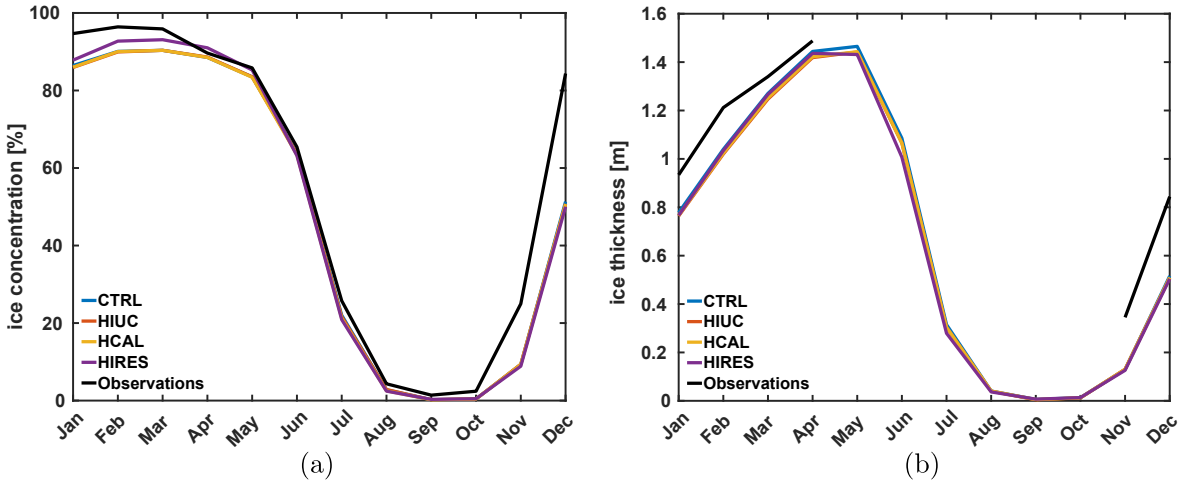

Figure 3.7: Seasonal cycle of (a) ice concentration and (b) thickness in the HBC for model experiments and observations (black). HBC ice concentration for simulations and AMSR-E/AMSR2 observations is averaged over 2004–2015, while for ice thickness, simulations and observations were averaged over 2011-2015.

is able to reproduce thinner ice in western Hudson Bay where there is a recurrent polynya. All experiments show thicker ice in eastern relative to western Hudson Bay, specifically east of the Belcher Islands. The observations show thicker ice from the center of the bay to the eastern coast, of which all experiments are not able to simulate. Additionally, thicker ice in the interior, between 1.5–2 m, is not captured as simulated ice thickness ranges from 0.8–1.2 m. Thicker ice along the eastern coast of Ungava Bay is captured by all experiments, with approximately the same magnitude. Ice thickness in Hudson Strait is simulated well, with the exception of the northwestern portion, where observations show ice thickness exceeding 2.5 m. In Foxe Basin, thick ice is located in the eastern region in observations, the location of which was captured in the model experiments. However, simulated ice thickness is up to 1 m thinner compared to observations.

Next we show the ice thickness distributions (ITDs) in Hudson Bay for January–April (Figure 3.9a-d), with observations shown in grey. All model simulations are unable to simulate the width of the ITD in observations, to compensate for this, the peak fraction of the ice thickness is higher than observations. We will note that the simulated peak ice thickness is close to the peak ice thickness in the observations. The HIRES simulation shows lower fractions of thicker ice from January–April, compared to the other experiments, however the fractions of the peak ice thickness are larger. This indicates that small scale processes not

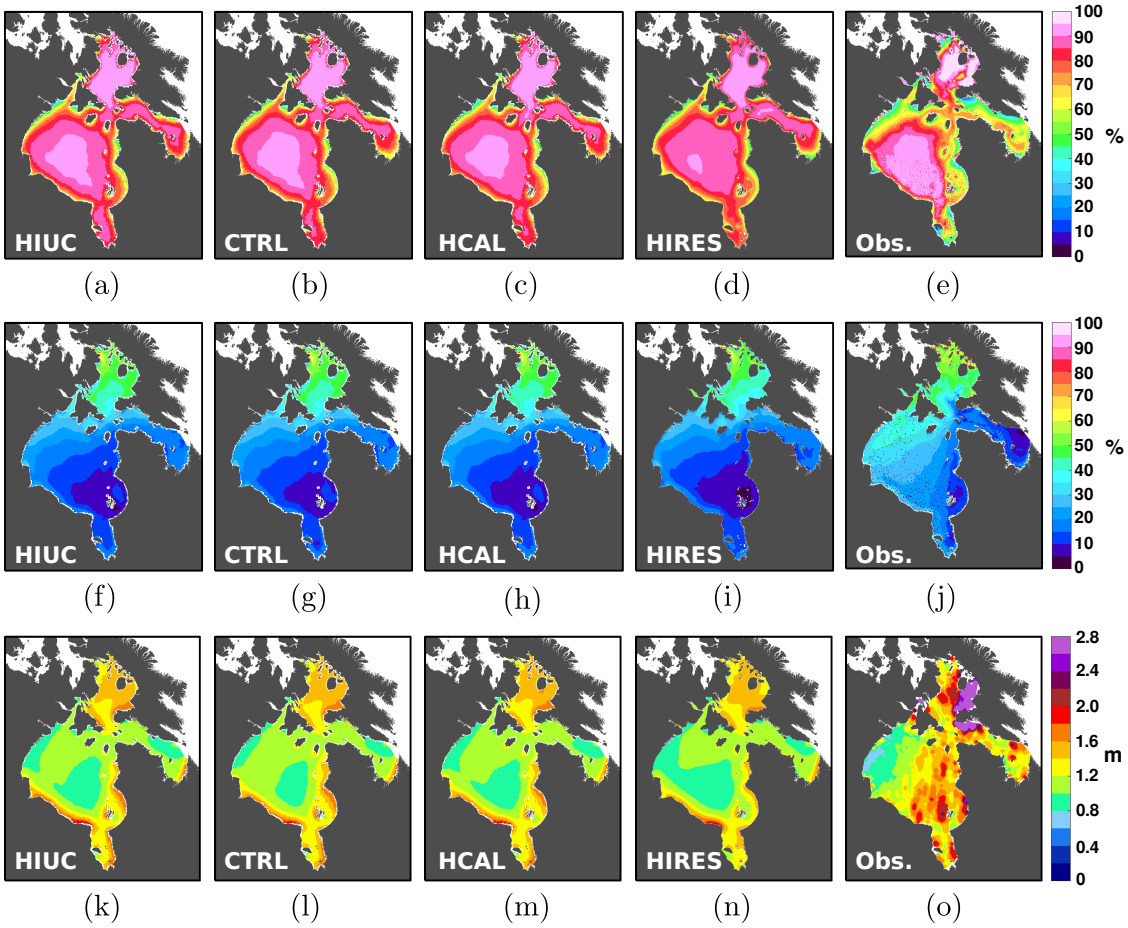

Figure 3.8: Top panels (a-e) show mean April–June ice concentration averaged from 2004–2011 HIUC, CTRL, HCAL, HIRES, and AMSR-E/AMSR2 observations. Center panels (f-j) shows the October–December ice concentration counter part to the top panels. In the bottom panels (k-o), mean January–April ice thickness (2011-2015) for HIUC, CTRL, HCAL, HIRES, and observations.

resolved in the lower resolution experiments are producing thinner ice.

The amount of freshwater stored in ice is important for the seasonal freshwater budget. Following Landy et al. (2017) with a constant sea ice salinity of 6, we calculated the freshwater stored in sea ice in April averaged over 2004-2015 (Table 3.1). Our results agree very well with their observational estimate, with all simulations within 70 km^3 of the observational estimate. CTRL contains the most freshwater in sea ice in April, while HIRES contains the least, which agrees best with observations, indicating the importance of resolution. Volume of runoff, as well as the timing and location of its release in the bay impacts the volume of freshwater in ice, as both HCAL and HIUC have less runoff than CTRL and thus have a lower volume of

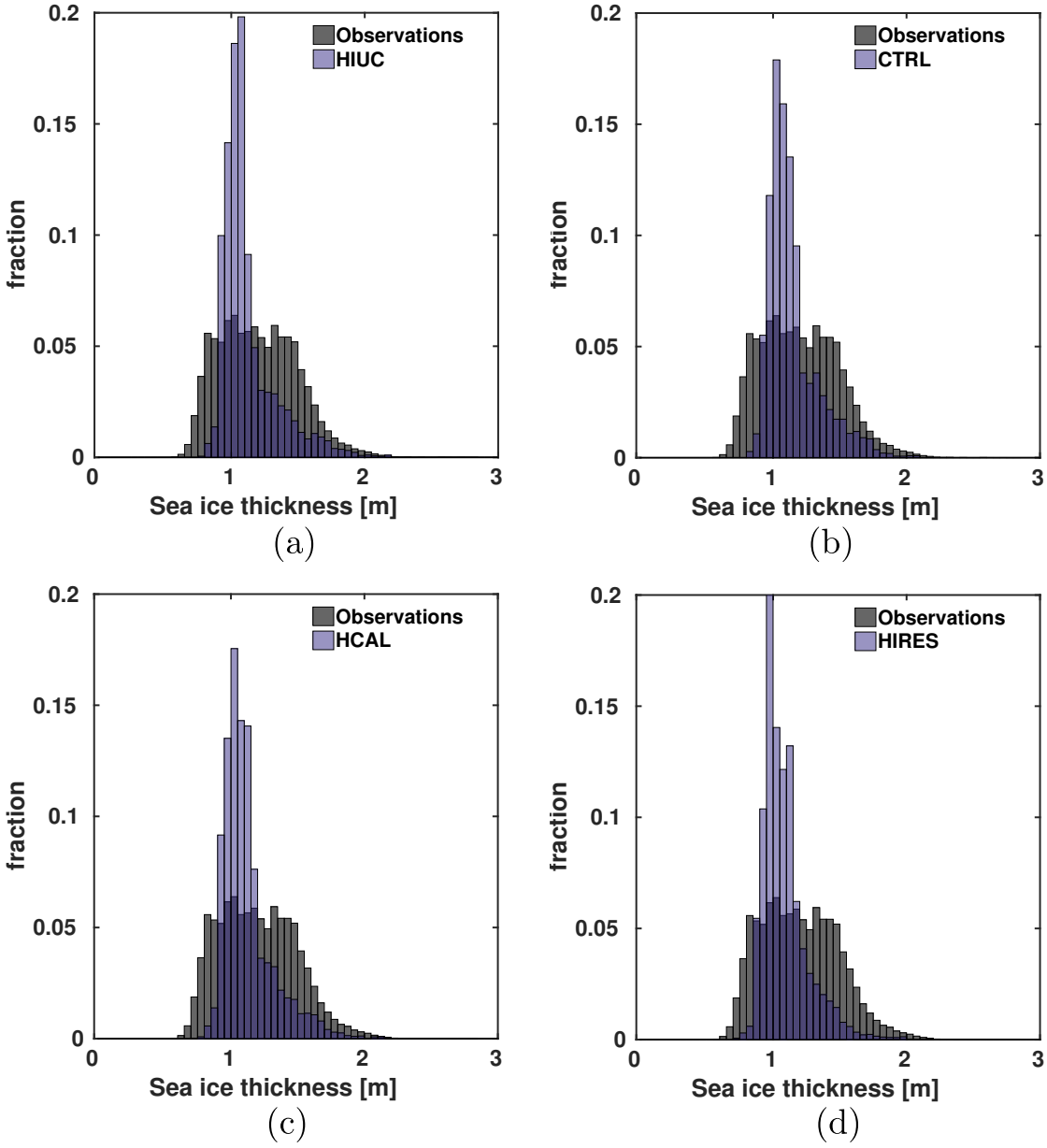

Figure 3.9: January–April (2011–2015) ice thickness distribution in Hudson Bay for (a) HIUC, (b) CTRL, (c) HCAL, and (d) HIRES shown in purple and observations shown in grey.

freshwater in ice. However, the HCAL simulation receives more discharge than HIUC, yet HIUC contains more freshwater in the ice.

We compare simulated ice drift to the OSI-SAF observational dataset (Figure 3.10). General sea ice circulation features are captured by all model simulations, with regional differences in ice drift patterns (Figure 3.10). An evaluation of root mean square error (RMSE) and bias (not shown) shows northwest/southeast asymmetry in drift and error distribution, comparable

Table 3.1: Liquid freshwater equivalent (± 1 standard deviation) contained in HBC sea ice in April (2004–2015) in units of km^3.

Experiment	$\mathbf{V}_{fw} \pm \mathbf{1}\sigma$
HIUC	1306 ± 112
CTRL	1323 ± 112
HCAL	1300 ± 107
HIRES	1285 ± 115
Landy et al. (2017)	1253 ± 15

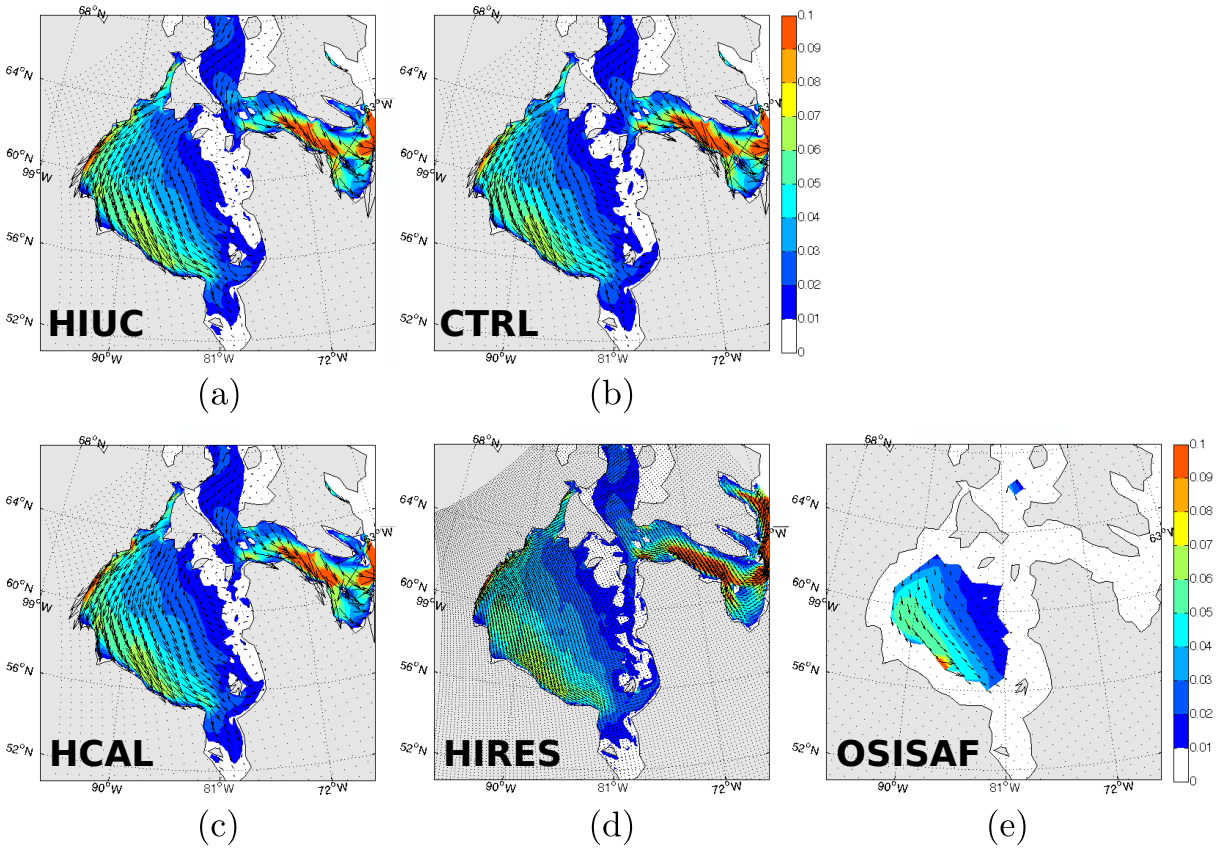

Figure 3.10: Mean 2007-2015 January-March ice drift vectors (arrows) and speed (colours) for (a) HIUC, (b) CTRL, (c) HCAL, (d) HIRES, and (e) OSI-SAF observations in units of m/s.

to Saucier et al. (2004).

Based on the above model evaluation, we acknowledge the larger model-observation discrepancies in sea ice in fall, however, we find overall, with the volume of equivalent freshwater in sea ice in April as well as the spatial distribution of ice concentration and thickness in the

bay, that the model is able to capture and simulate the main features of the sea ice. Similarly, oceanographic variables, such as temperature, salinity, and velocities, are also reasonably simulated.

3.3.2 HBC annual freshwater budget

The freshwater budget for the HBC and its subregions takes the form

$$\Delta FW storage = \int_{t_1}^{t_2} (FW_{adv} + FW_{surf} + R)\, dt \tag{3.2}$$

where $\Delta FW storage$ is the freshwater storage change between time t_1 and t_2; FW_{adv} is the lateral freshwater flux, the sign of which depends on both salinity and the direction of the flow; FW_{surf} is the freshwater input (due to precipitation minus evaporation and sea ice growth/melt) at the ocean surface; R is the runoff, a source of freshwater. For the purposes of this paper, negative fluxes are defined as leaving the region, and positive fluxes as entering the region, unless otherwise specified.

3.3.2.1 Impact of runoff on surface and lateral fluxes

Annual freshwater budgets for the HBC and its subregions were calculated for the three ¼° experiments, and are shown in Figure 3.11. The HBC, as a whole, receives about 22% (200 km^3/yr) more runoff in CTRL compared to the HIUC experiment. The HIUC discharge dataset has less runoff entering the HBC in all months, especially during peak runoff in spring and early fall (Figure 3.12a). The one exception is Hudson Strait, where the HIUC dataset is larger than the DT dataset by 8% (20 km^3/yr). The HCAL experiment has about 3% (20 km^3/yr) more runoff entering the HBC as a whole compared to HIUC. However, separating into subregions shows that CTRL has the least amount of runoff entering Hudson Strait, followed by HCAL and HIUC. In Hudson Bay, HCAL has 28% (110 km^3/yr) less runoff than CTRL. Foxe Basin, on the other hand, has the most discharge in the HCAL simulation, 35% (30 km^3/yr) and 56% (50 km^3/yr) more than the CTRL and HIUC experiments respectively. Lastly, the DT dataset has the most runoff in James Bay of 360 km^3/yr, compared to both HYPE products which have 213 and 224 km^3/yr for HIUC and HCAL accordingly.

Surface fluxes are larger in the HBC, as a whole, in the HIUC experiment, followed by

HCAL. The separate basins show higher net surface fluxes in Hudson Bay (13 km^3/yr or 12%) and James Bay (5 km^3/yr or 7%) in the HIUC simulation compared to CTRL, with no change in Hudson Strait surface fluxes. Surface fluxes in Hudson Bay in HCAL are similar to HIUC, while HCAL surface fluxes in James Bay are comparable to CTRL. Of the ¼° simulations, HCAL has the lowest magnitude of surface fluxes, at -2 km^3/yr in Hudson Strait. Foxe Basin surface fluxes show little change between the CTRL and HIUC experiments, while HCAL has the largest net negative surface flux.

Advected freshwater out of the HBC, as a whole, is 18% (140 km^3/yr) larger in the CTRL experiment than HIUC. This is also the case for freshwater advection in both Hudson and James Bays, with 21% (82 km^3/yr) and 41% (147 km^3/yr) more river discharge per year respectively. Advected freshwater in the HCAL simulation falls between CTRL and HIUC for Hudson Bay, and the HBC as a whole. Advection in James Bay for HCAL is 9% (25 km^3/yr) larger than HIUC, with CTRL having even more advected freshwater out of the shallow bay. On its own, Hudson Strait has more freshwater advection out of the strait in HIUC, by 18% (40 km^3/yr), than CTRL, due to less freshwater accumulation and more runoff, with HCAL falling in between. HCAL is the only simulation to have net advection out of Foxe Basin of the three ¼° experiments of -3 km^3/yr, with the CTRL experiment advecting 45% (13 km^3/yr) less into the basin than the HIUC experiment. The sum of the advected freshwater, surface fluxes, and runoff, equals the changing rate of freshwater that is stored in each region. All simulations show freshening of the HBC and its subregions over time. CTRL has higher freshwater accumulation overall than HIUC and HCAL, with the exception of Foxe Basin, where HCAL has the highest freshwater storage of the ¼° experiments.

Figure 3.12 shows the seasonality of each of the freshwater terms in the freshwater budget equation. In regions such as the HBC and Hudson Bay proper, surface fluxes are the dominant term throughout the year, with maxima in June and minima in December. In the HBC, advected freshwater and runoff are approximately in balance, with different runoff datasets having very little impact on the seasonality of advected freshwater (Figure 3.12a). As Foxe Basin is farther north, peak surface fluxes occur in July (Figure 3.12c) and are minimum in November, and like Hudson Bay proper, surface fluxes are the dominant term. The DT and HCAL datasets show a runoff peak in June in Foxe Basin, whereas, there is no clear peak in the

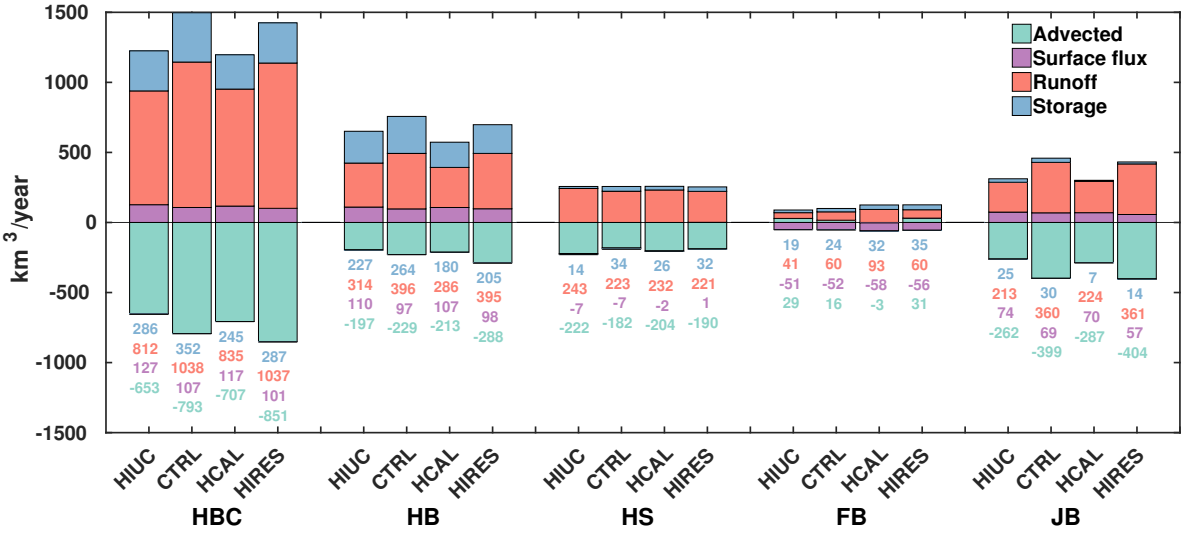

Figure 3.11: Annual freshwater budget for the HBC, Hudson Bay (HB), Hudson Strait and Ungava Bay (HS), Foxe Basin (FB), and James Bay (JB), for each of the four experiments. Units are km^3 per year, with a reference salinity of 33. Time period is 2004–2016.

HIUC runoff. This difference appears not to have a large impact on advected freshwater in the region, as peak net advection into the basin occurs in August in all simulations, with maximum freshwater export out of the basin occurring in November. Similar to the HBC seasonal cycle, Hudson Bay proper runoff and advected freshwater are roughly balanced during winter, with maximum freshwater export occurring in October and December for all experiments. However, during summer, freshwater export weakens and there is a net freshwater import into the bay. This occurs because of the large amount of freshwater that is advected out of James Bay (Figures 3.12e) and into Hudson Bay. During the year, surface fluxes in both James Bay and Hudson Strait are not as dominant in the freshwater budget as the other basins (Figure 3.12). Surface fluxes peak in June in both regions with minima in December and January for all experiments. Runoff seasonality in both basins is reduced in the HIUC experiment compared to CTRL, due to the more 'damped' seasonal cycle in the runoff dataset, with HCAL having more seasonality than HIUC, but less than CTRL. Advected freshwater in Hudson Strait varies between simulations, with CTRL advecting more than the other two ¼° experiments, likely due to the gap filled DT dataset, and is more noticeable in the winter months. Similarly, advected freshwater in James Bay is also reduced in HIUC and HCAL compared to the CTRL simulation throughout the year, due to the impacts of regulation

included in the HYPE datasets. The advection is directly related to the runoff, with peak advection occurring one month later than peak runoff in both summer and fall. Peak runoff in CTRL causes maximum freshwater storage in May, one month earlier than both the HIUC and HCAL experiments. In this study, our focus is on the long term mean, however, investigating year-to-year variability in the freshwater budget would be an interesting topic for future work.

Figure 3.13 shows the freshwater advection for each gate in the HBC for the four experiments (gates are indicated in Figure 3.12f). Freshwater and volume transport through Fury and Hecla Strait are similar for the HIUC, HCAL, and CTRL experiments, while freshwater transport through Southampton and Baffin Islands are similar between the HIUC and CTRL experiments. The HCAL experiment has 0.1 mSv more freshwater transport through this gate compared to the other two. Volume transport, on the other hand, varies, with CTRL having 7.4 mSv less volume transport than HIUC through Baffin–Southampton Gate, while HCAL has 1 mSv less transport compared to HIUC. Flow through Roes Welcome Sound is similar between HIUC and HCAL with regards to freshwater transport, but there is more volume transport, by 2.6 mSv, in HCAL. CTRL has a larger volume flux by 7.2 mSv compared to HIUC, in addition to 0.5 mSv more freshwater transport through the sound. Freshwater and volume fluxes through the Southampton–Quebec gate, James Bay, and eastern Hudson Strait are all smaller in the HIUC experiment compared to CTRL, which is due to the HIUC dataset having less runoff, as this dataset does not include regulation on the La Grande Riviere. Fluxes through the three eastern gates in the HCAL experiment fall between HIUC and CTRL. A detailed comparison of fluxes obtained here and available observations is presented in Section 3.4.

3.3.2.2 Impact of model resolution on surface and lateral fluxes

The CTRL and HIRES experiments have the same runoff forcing, and thus the same volume of runoff entering each region every year (Figure 3.11). HIRES has more advected freshwater out of the HBC by roughly 7% (60 km^3/yr). The difference leads to less, by roughly the same amount, freshwater storage in the HBC in the HIRES experiment, compared to CTRL. In the subregions, runoff and surface fluxes are similar in Foxe Basin, while advected freshwater (into Foxe Basin) is about twice as much as in CTRL. Thus, freshwater storage within Foxe Basin

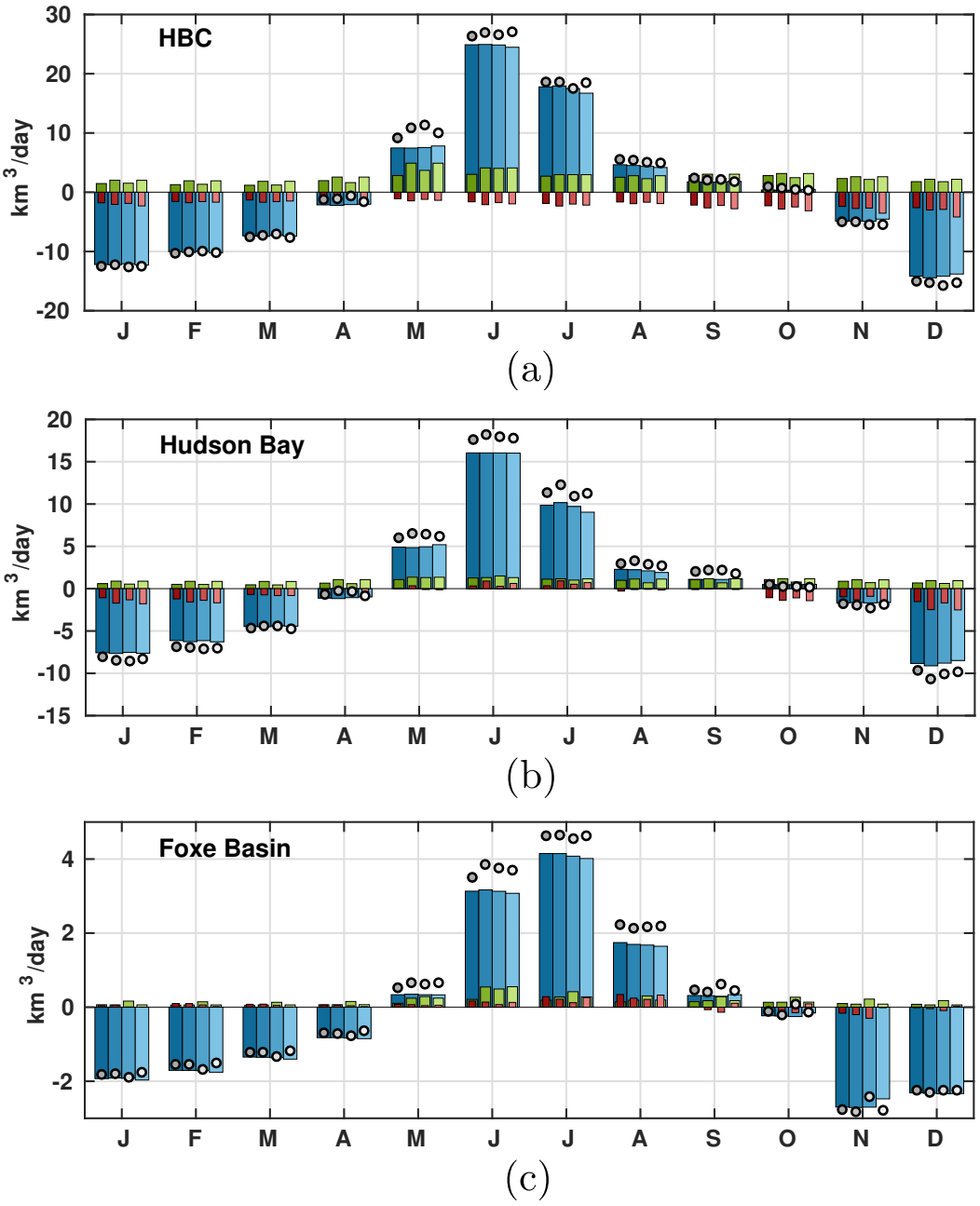

Figure 3.12: Seasonality of the freshwater budget terms (2004–2016) for four experiments in each region, (a) HBC, (b) Hudson Bay, (c) Foxe Basin, (d) Hudson Strait, and (e) James Bay (e). A map showing the definition of each region is shown in (f) with various gates indicated. Each term in the freshwater budget is shown by a different colour, with blue bars showing surface fluxes, river runoff as green bars, red bars as advected freshwater, and grey circles showing the change rate of freshwater storage in each basin. Experiments are ordered as HIUC, CTRL, HCAL, and HIRES (darkest to lightest shade) from left to right in each set of bars.

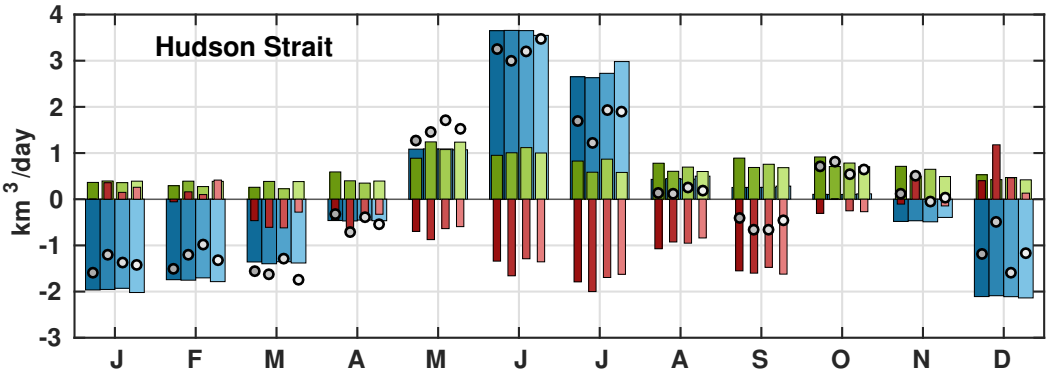

(d)

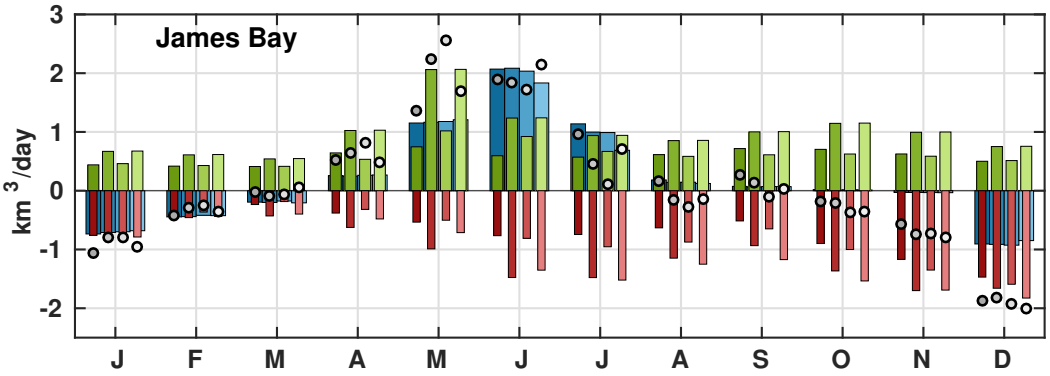

(e)

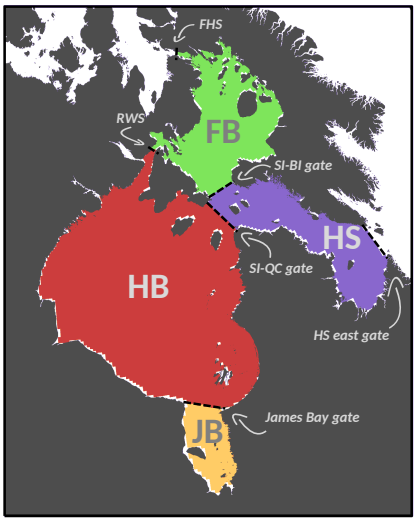

(f)

Figure 3.12: Gates are indicated in (f) with back dashed lines. Abbreviations for each gate are as follows: FHS for Fury and Hecla Strait, RWS for Roes Welcome Sound, SI-BI gate for Southampton Island-Baffin Island gate, SI-QC gate for Southampton Island-Quebec gate, and HS east gate for Hudson Strait east gate.

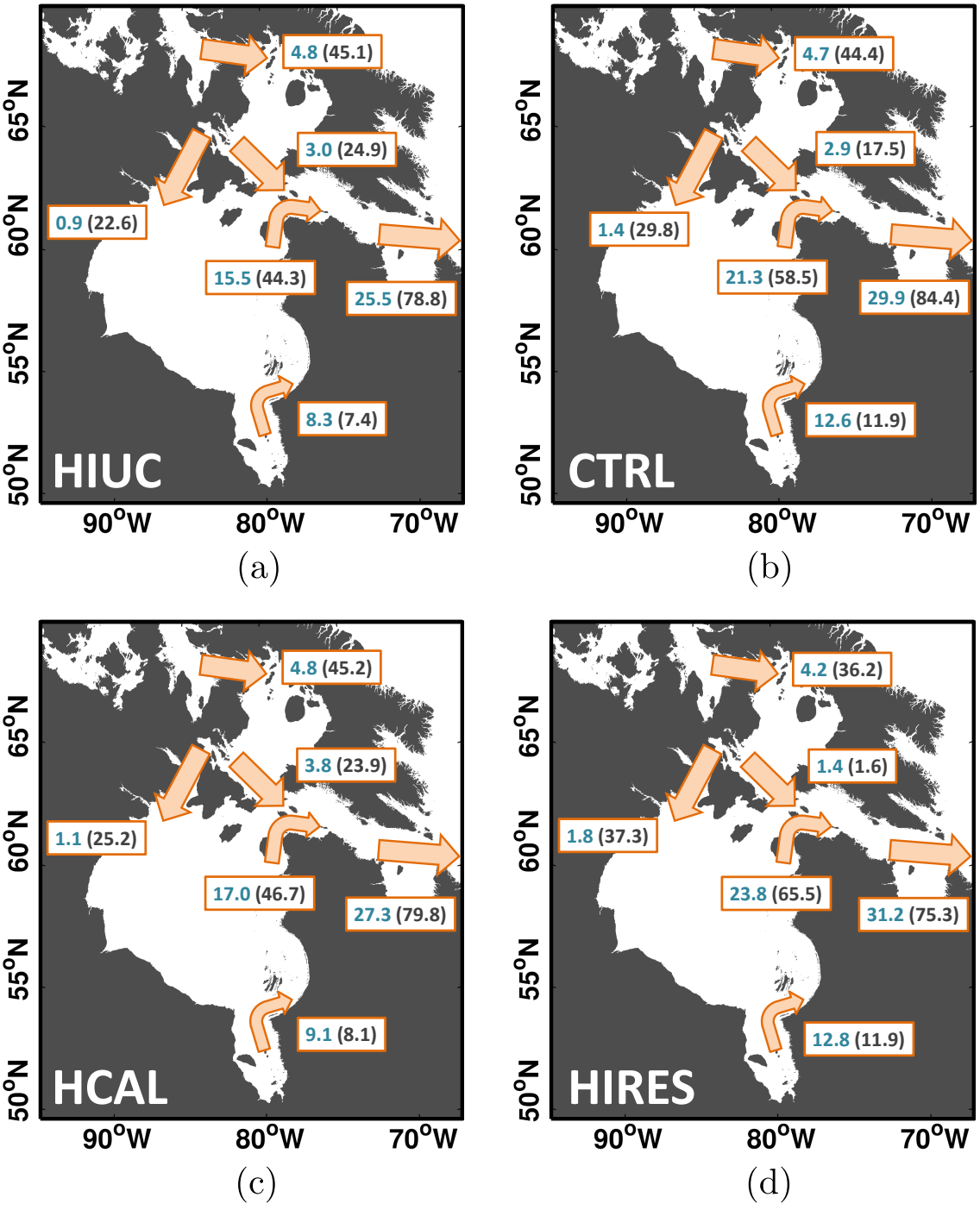

Figure 3.13: Advected freshwater (volume) fluxes shown in blue (black) between basins in the HBC for four experiments, (a) HIUC, (b) CTRL, (c) HCAL, and (d) HIRES. Fluxes are averaged from 2004–2016, with units of mSv (1 mSv = 1000 m^3/s).

in HIRES is 31% (11 km^3/yr) larger than in CTRL. In Hudson Strait, runoff is similar while advected freshwater is 4% (8 km^3/yr) higher than CTRL. Surface fluxes are close to zero in HIRES, and are a freshwater source, whereas CTRL surface fluxes are a freshwater sink and have a magnitude of 7 km^3/yr. Freshwater storage in the strait is similar between the two runs, at 34 km^3/yr in CTRL and 32 km^3/yr in HIRES. Both surface fluxes and runoff are the same in Hudson Bay. Advected freshwater, however, is larger in the HIRES simulation compared to CTRL by 20% (60 km^3/yr), leading to less freshwater storage in the HIRES simulation.

Figure 3.12 (lightest shaded symbols) shows the freshwater seasonal cycle for all regions of the HBC for the HIRES simulation. The freshwater seasonal cycle of both the HBC, as a whole, Hudson Bay proper, and Foxe Basin is not largely impacted by increased resolution. Differences between experiments are more clearly seen in Hudson Strait (Figure 3.12d) and James Bay (Figure 3.12e). Advection into and out of Hudson Strait is generally smaller in all months (for the exception of February), with little advection in HIRES in December, while net freshwater import occurs in December in CTRL. James Bay freshwater advection is also diminished during the first part of the year, with increasing advection occurring in May/June and maximum summertime advection occurring in July, while CTRL has maintained peak advection through June and July. Advection is larger throughout the fall in HIRES compared to CTRL.

HIRES experiment fluxes between each region of the HBC are shown in Figure 3.13d. Compared to CTRL (Figure 3.13b), freshwater and volume fluxes in HIRES are similar from James Bay, but lower through Fury and Hecla Strait. Lower freshwater fluxes occur between Foxe Basin and Hudson Strait, with volume fluxes being largely reduced in HIRES to only 1.6 mSv compared to 17.5 mSv in CTRL. Fluxes through Roes Welcome Sound and between Southampton Island and Quebec are larger in HIRES than CTRL, in addition to higher freshwater fluxes out of Hudson Strait into the North Atlantic. Volume fluxes, however, were smaller than CTRL out of Hudson Strait.

3.3.3 Boundary–Interior exchange in Hudson Bay

To investigate the processes involved in freshwater exchange between the boundary and interior regions in Hudson Bay, a boundary line based on the annual mean barotropic streamfunction is defined. To be more specific, we chose the contour of -0.18 Sv (1 Sv = 10^6 m^3/s) of the annual mean streamfunction (Figure 3.14, top panels) for our analysis, as this was the largest value which was a closed contour in Hudson Bay in the HIRES simulation. The total freshwater and volume transport, in addition to the Ekman, turbulent, and mean flow contributions are shown in Figure 3.14 for the four experiments. Ekman transports were calculated using:

$$T_{EKy} = \frac{-1}{f\rho}\tau_x dx \tag{3.3}$$

$$T_{EKx} = \frac{1}{f\rho}\tau_y dy \tag{3.4}$$

where T_{EKx} and T_{EKy} are the Ekman transports in the model grid x and y directions respectively. Grid cell width is denoted by dx and dy in the x and y directions respectively, f is the Coriolis parameter, and ρ represents density. Surface stress in the model grid x and y directions is given by τ_x and τ_y respectively. The freshwater transport due to Ekman transport is calculated by multiplying the Ekman volume transport with the freshwater concentration in the top 24 m (the nearest vertical level) based on Yang (2006). The total flow ($\boldsymbol{v}$) can be decomposed into the mean and turbulent components. Here we assume the 5-day average model output as the total flow ($\boldsymbol{v}$) and a running 25-day mean as the mean flow component ($\overline{\boldsymbol{v}}$). Thus the turbulent component is given by $\boldsymbol{v}' = \boldsymbol{v} - \overline{\boldsymbol{v}}$.

On average, we see minimal turbulent freshwater exchange between the boundary and interior (Figure 3.14, orange), while the mean component of the flow (yellow) contributes to the majority of freshwater exchanged, with significant contributions from Ekman transport (purple). It should be noted that both the turbulent and Ekman components of the flow are highly variable, but the variability has been averaged out in the mean seasonal cycle. Ekman transport through time (not shown) reach magnitudes of 10 km^3/day, with the largest values occurring between September–December. Turbulent fluxes have smaller magnitudes, reaching over 6 km^3/day in fall, and have lower values during winter months (January–April) with a maximum value of almost 3 km^3/day (not shown).

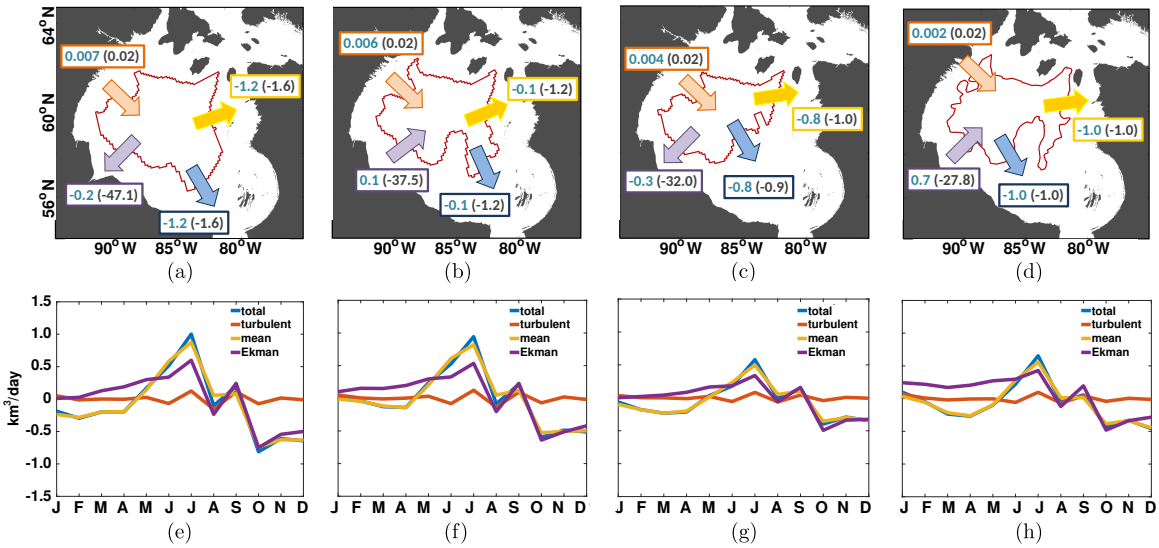

Figure 3.14: Freshwater exchange between Hudson Bay interior and boundary. Annual mean transports (top panels) of mean freshwater (volume) exchange in blue (black), in units of mSv, across the mean barotropic streamfunction (-0.18 Sv contour, red line), and the seasonal cycle of each process (bottom panels, units of km^3/day) are shown for four model experiments, (a,e) HIUC, (b,f) CTRL, (c,g) HCAL, and (d,h) HIRES. Blue represents the total freshwater exchange between the two regions, while yellow, orange, and purple show the mean, turbulent, and Ekman components of the flow respectively. Note that the arrows show the direction of the freshwater flux, while the arrow locations are arbitrary.

Net freshwater advection (Figure 3.14, blue) is directed out of the interior in all experiments. Comparing the HIUC and CTRL experiments (Figures 3.14e and 3.14f), about three times more freshwater is exported out of the interior from January–April than CTRL, in addition to peak export in October being larger as well (blue). Peak import in July is similar in both experiments. The total freshwater flux is mostly determined by the mean component of the flow, having a comparable seasonal cycle. The mean flow in summer has been shown to have an anticyclonic component in eastern Hudson Bay, generated by the spring freshet and reinforced by the mean wind patterns, causing freshwater to enter the interior, as discussed in Gough et al. (2005) and Ridenour et al. (2019). The net and mean components of the volume flux are directed out of the interior and are similar in magnitude for both experiments. The turbulent component of the flow is also similar for both volume and freshwater transports for the two experiments. Ekman volume transport in both experiments is directed out of the interior, with HIUC having more water directed out of the interior on average than CTRL. Ekman freshwater transport is a source to the interior in CTRL, while it is a sink in the

HIUC experiment. This can be explained by more freshwater entering the interior with the DT runoff at the beginning of the year compared to the HIUC discharge, along with weaker freshwater export in the second half of the year (Figure 3.14).

The HCAL experiment (Figures 3.14c and 3.14g) is different from the other two ¼° experiments as the annual mean -0.18 Sv streamline is not present in southeastern Hudson Bay. This results in weaker exchange between the boundary and the interior compared to both HIUC and CTRL, and is most similar to the HIRES interior-boundary exchange. The turbulent component of the flow in HCAL is a net source of both volume and freshwater to the interior while Ekman transport is a net sink of freshwater and volume. Ekman transport is still a source of freshwater in summer and a sink in fall, however magnitudes of the annual cycle are reduced. Similarly for both the mean and total freshwater transports, magnitudes are weaker in both summer and fall in HCAL compared to HIUC and CTRL.

Figures 3.14d and 3.14h show freshwater exchange between the interior and boundary regions of Hudson Bay for the HIRES run. The annual mean barotropic streamfunction has a more convoluted shape in the ⅟₁₂° than the ¼° experiments. The freshwater exchange between the interior and boundary is still dominated by the mean component of the flow (yellow), but with a diminished seasonal cycle. We see larger magnitudes of freshwater export out of the interior in late winter/early spring, which leads to larger net export values on average in HIRES than CTRL, for both the mean and total freshwater exchange components. Ekman volume transport is directed out of the interior on average, however, Ekman freshwater transport is directed into the interior on average in the HIRES experiment (Figure 3.14d), as with CTRL, but with a larger magnitude. Ekman transport of freshwater into the interior is maintained for the first seven months of the year, while in CTRL, import of freshwater over the first three months is less than HIRES (Figure 3.14f and 3.14h). The turbulent component of the flow is small in both experiments, but more significant on shorter time scales. This, however, is beyond the scope of this study.

Freshwater flowing from the interior to the boundary, instead of from the boundary to the interior, may seem counter intuitive, since runoff flows directly into the boundary. In this analysis, we do not include the lateral movement of sea ice in our freshwater exchanges between the two regions. Therefore, sea ice imported to the interior is solid freshwater, and

is only included in the lateral fluxes if the sea ice melts and the resulting liquid freshwater is transported across the streamline. Another source of freshwater export from the interior is if water more saline than the reference value leaves the boundary and crosses the streamline, which results in a freshwater flux out of the interior to the boundary.

There are still open questions with regards to the retention of freshwater in the bay. Is the bay opposite to the Beaufort Gyre, with a predominantly cyclonic flow with freshwater retention events? This topic requires further study, as this might provide some key insights to processes occurring in the bay and the resulting freshwater fluxes to the North Atlantic.

3.3.4 HBC Residence Time

This section presents the residence time of riverine water within the HBC based on the results of Ariane particle tracking. Note that the analysis is based on the CTRL simulation only. Figure 3.15 shows the percentage of Ariane particles remaining in the HBC (Figure 3.15a), and the particle depth distribution at the end of December 2016 for each of the four regions (Figure 3.12f). By the end of the 13^{th} year after being released in Hudson Bay, 16.6% of particles remain in the HBC. The majority of particles are in the top 60 m, while a few particles reach depths of 200 m and below. Particles that remain are fairly well distributed around Hudson and James Bays, as well as along the southern coast of Hudson Strait. Hudson Bay particles do enter Foxe Basin, and for the most part, remain in the south, near Southampton Island, with few being located farther north.

The majority of particles released in James Bay leave the HBC after 4 years, with a slow decline to 14.2% in the following 9 years (Figure 3.15a). As with Hudson Bay, the highest concentration of particles are within the top 60 m. Remaining James Bay particles are found to be well distributed in Hudson Bay and in the Hudson Strait outflow. Once again, particles that reach Foxe Basin, are mostly in the south, at varying depths, ranging from the surface to almost 300 m.

The region with the most particles remaining in the HBC is Foxe Basin, at 38.7% (Figure 3.15a). Foxe Basin particles are well distributed throughout the HBC, and has a smoother depth profile than the other HBC regions. Foxe Basin particles are mixed to deeper depths north of Southampton Island, likely due to the many polynyas in the region (Prinsenberg,

1986a). Particles are more concentrated in eastern Foxe Basin and likely were released in the vicinity, where they have remained.

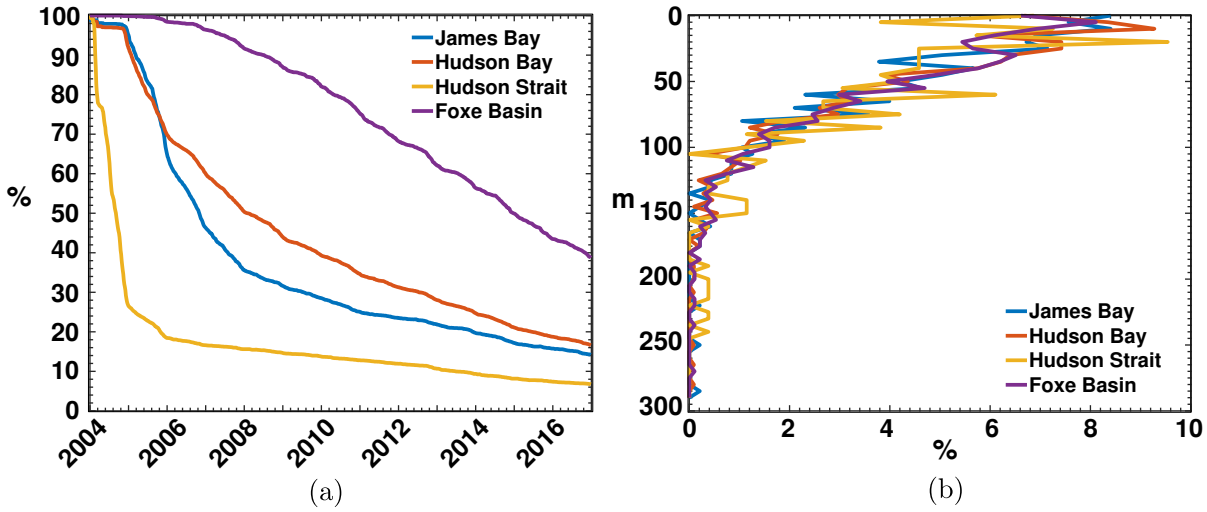

Figure 3.15: Particles released using Ariane and tracked for 13 years. The time series of particles remaining in the HBC (left) and final particle depth distribution of remaining particles in the HBC (right) for each of the four regions.

Fitting a trend line to the time series of the number of particles remaining in the HBC, we can estimate the residence time for particles released in each region. Using a 10% threshold, we found that particles released in Hudson Bay, using an exponential curve, can remain in the HBC for 17.6 years, while Foxe Basin has a residence time of 32.2 years, also using an exponential trend line. Hudson Strait has the shortest residence time of 9.5 years (no trend line used). Finally, James Bay was estimated to have a residence time of 21.5 years using an exponential curve. We suggest a topic of future work would be to investigate the temporal and spatial variability of residence times. Particles released during the spring freshet may have shorter residence times than those released in winter, while particles released in northwestern Hudson Bay likely have a longer residence time than those released along the eastern coast.

3.4 Discussion

In this study we investigated the sensitivity of freshwater in the HBC to model resolution and runoff forcing. The results obtained here also have implications for pathways and residence times of various nutrients or pollutants commonly found in river discharge.

In terms of the freshwater budget, our estimates of surface fluxes are comparable to Prinsenberg (1988), with our peak freshwater fluxes in the summer of 18 km^3/day compared to their 12 km^3/day (including areas of both Hudson Bay and James Bay). Minimum surface fluxes are similar in both studies. Hudson and James Bay surface fluxes calculated by St-Laurent et al. (2011) are roughly 8-23% lower than in this study. Mean Hudson and James Bay runoff shown here accounts for 37%–41% (510–756 km^3/yr) of the freshwater budget, while average runoff in St-Laurent et al. (2011) accounts for 41% of the freshwater budget for the same region. Additionally, total freshwater advection out of the Hudson and James Bay area was 50% of the freshwater budget (743 km^3/yr; St-Laurent et al., 2011), while our estimates are lower, ranging from 32%–38%.

Earlier estimates of freshwater and volume fluxes through Fury and Hecla Strait vary, with winter volume (freshwater) fluxes of 40 (1.2) mSv (Barber, 1965), and summer volume fluxes of 100 (3.0) mSv (Sadler, 1982). Using the aforementioned volume fluxes, Straneo and Saucier (2008a) estimated the year round volume and freshwater fluxes to be 70 and 2.8 mSv (S_{ref}=33) respectively. Our results are closest to the winter season fluxes from Barber (1965). Our larger freshwater flux estimates are partly due to the fact that Fury and Hecla Strait is wider in the model domain than in reality due to the model resolution, while previous assumptions, such as constant salinity and volume transport for consecutive months of the year, might also lead to discrepancies between studies.

Hudson Strait net volume and freshwater fluxes were estimated to be 100-101 and 29-35 mSv respectively (Drinkwater, 1988; Saucier et al., 2004; Straneo and Saucier, 2008a). The net freshwater and volume fluxes simulated here are smaller, ranging from 25.5–31.2 and 75.3–84.4 mSv respectively. Additionally, Straneo and Saucier (2008b) estimate the volume outflow of Hudson Strait to be between 1–1.2 Sv, whereas in this suite of experiments, we have a volume outflow range of 1.2–1.4 Sv.

Fluxes through Roes Welcome Sound and the three eastern gates connecting Hudson Bay and Hudson Strait were modelled by St-Laurent et al. (2011), who found freshwater and volume fluxes through Roes Welcome Sound to be 0.5 and 18 mSv respectively, both of which are lower than the fluxes simulated here. We find that our range for freshwater fluxes through the passage between Southampton Island and Quebec of 15.5–23.8 mSv, are lower than or

comparable to the St-Laurent et al. (2011) value of 24 mSv, with the HIRES experiment having the best agreement. Volume fluxes obtained here are in the range of 44.3–65.5 mSv, compared to the volume flux of 35 mSv found by St-Laurent et al. (2011).

The volume fluxes through the Southampton–Baffin Island gate in this study range from 1.6–24.9 mSv out of Foxe Basin. These values are lower than the modelling study done by Defossez et al. (2012), who found a net volume flux of 56 mSv out of Foxe Basin. The discrepancy between studies can be explained by the horizontal and vertical resolutions, as well as different averaging time periods.

The freshwater exchange between the Hudson Bay boundary and interior has been studied previously by St-Laurent et al. (2012, 2011). In agreement with their studies, our results also show that freshwater from the boundary is transported to the interior in summer via Ekman transport, and vice versa in the fall. They neglected the eddy and mean components of the flow and assumed the flow could be separated into the geostrophic and Ekman components. Our 5-day mean Ekman fluxes agree in magnitude with those modelled by St-Laurent et al. (2011). Our turbulent component of the flow, however, has fluxes into the interior up to 6 km^3/day, and thus cannot be ignored on shorter time scales. However, investigating the specifics of the turbulent component is beyond the scope of this study.

Regarding residence time of river discharge, our results indicate that the residence time for the HBC could be as long as 32.2 years. This is longer than the previous estimates, 6.6 years by Prinsenberg (1984, 1986c) and 3–7 years (depending on the fitting method to reach the 10% threshold) by St-Laurent et al. (2011). However, considering river discharge can mix into the deep waters (Granskog et al., 2011), our estimated residence time in Hudson Bay (17.6 years) and James Bay (21.5 years) compares well with the Hudson Bay deep water residence time (4–14 years) based on the apparent oxygen utilisation measurements (Pett et al., 1982). Even though a full investigation of river runoff pathways is beyond the scope of this paper, it brings up interesting questions as to the processes involved, such as those mentioned by Granskog et al. (2011), and runoff pathways from different regions in the HBC.

Our study has provided a look at present day freshwater dynamics in the HBC, in addition to evaluating the sensitivity of the region to model resolution and runoff forcing. Using different estimates of runoff allows us to test the sensitivity of the region, which has importance

for future studies. Our main findings in this paper are:

Sensitivity to runoff Overall, the seasonality of freshwater is robust, however the strength and magnitude of fluxes were impacted. Increased discharge in runoff datasets lead to stronger circulation patterns, while decreased discharge and seasonality throughout the year lead to weaker circulation. Lower freshwater and volume exchange between subregions and between the HBC and North Atlantic were also due to decreased discharge and seasonality.

Sensitivity to model resolution Increased model resolution was able to reproduce freshwater contained in sea ice, however there was generally little impact on fluxes through gates with simple flow dynamics. Small scale processes were found to be important through Southampton–Baffin Island Gate. Freshwater interior-boundary exchange was also impacted by higher model resolution via the Ekman and mean components of the flow.

HBC residence time Particles released along the coast indicate that the residence time for the HBC is as long as 32.2 years, with HBC residence times for Foxe Basin, Hudson Bay, James Bay, and Hudson Strait being 32.2, 17.6, 21.5, and 9.5 years respectively, agreeing with previous estimates.

Our work highlights topics for future work such as the role of the turbulent component of the flow and freshwater retention in Hudson Bay. A complete understanding of the pathways of river discharge, in addition to regional variability of residence time, is important for tracing various nutrients in addition to pollutants, such as mercury (Hare et al., 2010; Wang and Zhang, 2013), both of which can impact the ecosystem and food sources for communities in the HBC.

Acknowledgments

We would like to thank Environment and Climate Change Canada for the use of the CGRF forcing fields, as well as the producers of GLORYS for the reanalysis data that we use to initialize our model simulations as well as providing our model with open boundary conditions.

Thank you to Dr. Gregory Smith who provided the CGRF atmospheric forcing to force our ocean model. This work is part of the BaySys project, thus we thank the Natural Sciences and Engineering Research Council of Canada and Manitoba Hydro for funding the BaySys project (CRDPJ 470028-14). We are grateful for the use of the HYPE dataset which was provided by BaySys Team 2 (Matt MacDonald, Tricia Stadnyk, and Stephen Déry). We are grateful to Dr. J Bamber for the Greenland melt dataset, and to Aviso, ArcticNet, ICES, and MEDS for their observational data which was used to evaluate the model simulations. Observational datasets such as SST data from NOAA ESRL/PSD, ice drift from EUMETSAT OSISAF, and ice concentration and thickness data from Integrated Climate Data Centre at the University of Hamburg were also greatly appreciated for model evaluation. Computational resources used for our work were provided by Westgrid and Compute Canada, which made this work possible.

Bibliography

Aagaard, K. and Carmack, E. C. (1989). The role of sea ice and other fresh water in the Arctic circulation. *Journal of Geophysical Research: Oceans*, 94(C10):14485–14498.

Andersson, J. C. M., Pechlivanidis, I. G., Gustafsson, D., Donnelly, C., and Arheimer, B. (2013). Key factors for improving large-scale hydrological model performance. In Lekkas, T., editor, *Proceedings of the 13th International Conference on Environmental Science and Technology*, Proceedings of the International Conference on Environmental Science and Technology, pages 77–88, Univ, Aegean, 30, Voulgaroktonou Str, Athens, GR 114 72, Greece. Univ Aegean; Global Network Environm Sci & Technol, Global Nest, Secritariat. 13th International Conference on Environmental Science and Technology (CEST), Athens, Greece, Sep 05-07, 2013.

Bamber, J., van den Broeke, M., Ettema, J., Lenaerts, J., and Rignot, E. (2012). Recent large increases in freshwater fluxes from Greenland into the North Atlantic. *Geophysical Research Letters*, 39(19).

Barber, F. G. (1965). Current Observations in Fury and Hecla Strait. *Journal of the Fisheries Research Board of Canada*, 22(1):225–229.

Blanke, B., Arhan, M., Madec, G., and Roche, S. (1999). Warm Water Paths in the Equatorial Atlantic as Diagnosed with a General Circulation Model. *Journal of Physical Oceanography*, 29(11):2753–2768.

Blanke, B. and Delecluse, P. (1993). Variability of the Tropical Atlantic Ocean Simulated by a General Circulation Model with Two Different Mixed-Layer Physics. *Journal of Physical Oceanography*, 23(7):1363–1388.

Blanke, B. and Raynaud, S. (1997). Kinematics of the Pacific Equatorial Undercurrent: An Eulerian and Lagrangian Approach from GCM Results. *Journal of Physical Oceanography*, 27(6):1038–1053.

Bougeault, P. and Lacarrere, P. (1989). Parameterization of orography-induced turbulence in a mesobeta-scale model. *Monthly Weather Review*, 117(8):1872 – 1890.

Castro de la Guardia, L., Myers, P. G., Derocher, A. E., Lunn, N. J., and Terwisscha van Scheltinga, A. D. (2017). Sea ice cycle in western Hudson Bay, Canada, from a polar bear perspective. *Marine Ecology Progress Series*, 564:225–233.

Dai, A., Qian, T., Trenberth, K. E., and Milliman, J. D. (2009). Changes in Continental Freshwater Discharge from 1948 to 2004. *Journal of Climate*, 22(10):2773–2792.

Dai, A. and Trenberth, K. E. (2002). Estimates of Freshwater Discharge from Continents: Latitudinal and Seasonal Variations. *Journal of Hydrometeorology*, 3(6):660–687.

de Boisséson, E., Thierry, V., Mercier, H., Caniaux, G., and Desbruyères, D. (2012). Origin, formation and variability of the Subpolar Mode Water located over the Reykjanes Ridge. *Journal of Geophysical Research: Oceans*, 117(C12).

Defossez, M., Saucier, F., Myers, P., Caya, D., and Dumais, J. (2012). Comparing Winter and Summer Simulated Estuarine Circulations in Foxe Basin, Canada. *Atmosphere-Ocean*, 50(3):386 – 401.

Déry, S. J., Hernández-Henríquez, M. A., Burford, J. E., and Wood, E. F. (2009). Observational evidence of an intensifying hydrological cycle in northern Canada. *Geophysical Research Letters*, 36(13).

Déry, S. J., Mlynowski, T. J., Hernández-Henríquez, M. A., and Straneo, F. (2011). Interannual variability and interdecadal trends in Hudson Bay streamflow. *Journal of Marine Systems*, 88:341 – 351.

Déry, S. J., Stadnyk, T. A., MacDonald, M. K., and Gauli-Sharma, B. (2016). Recent trends and variability in river discharge across northern Canada. *Hydrology and Earth System Sciences*, 20(12):4801 – 4818.

Déry, S. J., Stadnyk, T. A., MacDonald, M. K., Koenig, K. A., and Guay, C. (2018). Flow alteration impacts on Hudson Bay river discharge. *Hydrological Processes*, 32(24):3576–3587.

Déry, S. J., Stieglitz, M., and McKenna, E. C. (2005). Characteristics and Trends of River Discharge into Hudson, James, and Ungava Bays, 1964–2000. *Journal of Climate*, 18(14):2540–2557.

Drinkwater, K. F. (1988). On the Mean and Tidal Currents in Hudson Strait. *Atmosphere–Ocean*, 26(2):252 – 266.

Dukhovskoy, D. S., Myers, P. G., Platov, G., Timmermans, M.-L., Curry, B., Proshutinsky, A., Bamber, J. L., Chassignet, E., Hu, X., Lee, C. M., and Somavilla, R. (2016). Greenland freshwater pathways in the sub-Arctic seas from model experiments with passive tracers. *Journal of Geophysical Research: Oceans*, 121(1):877–907.

Fichefet, T. and Maqueda, M. A. M. (1997). Sensitivity of a global sea ice model to the treatment of ice thermodynamics and dynamics. *Journal of Geophysical Research: Oceans*, 102(C6):12609–12646.

Gagnon, A. S. and Gough, W. A. (2002). Hydro-Climatic trends in the Hudson Bay Region, Canada. *Canadian Water Resources Journal / Revue canadienne des ressources hydriques*, 27(3):245–262.

Gagnon, A. S. and Gough, W. A. (2005). Trends in the Dates of Ice Freeze-up and Breakup over Hudson Bay, Canada. *Arctic*, 58(4):370–382.

Gaspar, P., Gregoris, Y., and Lefevre, J. (1990). A simple eddy kinetic-energy model for simulations of the oceanic vertical mixing - Tests at station Papa and long-term upper ocean study site. *Journal of Geophysical Research: Oceans*, 95(C9):16179 – 16193.

Gelfan, A., Gustafsson, D., Motovilov, Y., Arheimer, B., Kalugin, A., Krylenko, I., and Lavrenov, A. (2017). Climate change impact on the water regime of two great Arctic rivers: modeling and uncertainty issues. *Climatic Change*, 141(3):499–515.

Gillard, L. C., Hu, X., Myers, P. G., and Bamber, J. L. (2016). Meltwater pathways from marine terminating glaciers of the Greenland ice sheet. *Geophysical Research Letters*, 43(20):10,873–10,882.

Gough, W., Cornwell, A., and Tsuji, L. (2004a). Trends in Seasonal Sea Ice Duration in Southwestern Hudson Bay. *Arctic*, 57(3):299–305.

Gough, W. A., Gagnon, A. S., and Lau, H. P. (2004b). Interannual Variability of Hudson Bay Ice Thickness. *Polar Geography*, 28(3):222–238.

Gough, W. A., Robinson, C., and Hosseinian, R. (2005). The Influence of James Bay River Discharge on Churchill, Manitoba Sea Level. *Polar Geography*, 29(3):213–223.

Granskog, M. A., Kuzyk, Z. Z. A., Azetsu-Scott, K., and Macdonald, R. W. (2011). Distributions of runoff, sea-ice melt and brine using δ^{18}O and salinity data — A new view on freshwater cycling in Hudson Bay. *Journal of Marine Systems*, 88:362 – 374.

Granskog, M. A., Macdonald, R. W., Mundy, C.-J., and Barber, D. G. (2007). Distribution, characteristics and potential impacts of chromophoric dissolved organic matter (CDOM) in Hudson Strait and Hudson Bay, Canada. *Continental Shelf Research*, 27(15):2032 – 2050.

Hare, A. A., Stern, G. A., Kuzyk, Z. Z. A., Macdonald, R. W., Johannessen, S. C., and Wang, F. (2010). Natural and Anthropogenic Mercury Distribution in Marine Sediments from Hudson Bay, Canada. *Environmental Science & Technology*, 44(15):5805–5811.

Hochheim, K. P. and Barber, D. G. (2010). Atmospheric forcing of sea ice in Hudson Bay during the fall period, 1980–2005. *Journal of Geophysical Research: Oceans*, 115(C5).

Hochheim, K. P. and Barber, D. G. (2014). An Update on the Ice Climatology of the Hudson Bay System. *Arctic, Antarctic, and Alpine Research*, 46(1):66–83.

Holdsworth, A. M. and Myers, P. G. (2015). The Influence of High-Frequency Atmospheric Forcing on the Circulation and Deep Convection of the Labrador Sea. *Journal of Climate*, 28(12):4980–4996.

Holmes, R. M., McClelland, J. W., Peterson, B. J., Tank, S. E., Bulygina, E., Eglinton, T. I., Gordeev, V. V., Gurtovaya, T. Y., Raymond, P. A., Repeta, D. J., Staples, R., Striegl, R. G., Zhulidov, A. V., and Zimov, S. A. (2012). Seasonal and Annual Fluxes of Nutrients and Organic Matter from Large Rivers to the Arctic Ocean and Surrounding Seas. *Estuaries and Coasts*, 35(2):369–382.

Hu, X. and Myers, P. G. (2013). A Lagrangian view of Pacific water inflow pathways in the Arctic Ocean during model spin-up. *Ocean Modelling*, 71:66 – 80.

Hu, X., Sun, J., Chan, T. O., and Myers, P. G. (2018). Thermodynamic and dynamic ice thickness contributions in the Canadian Arctic Archipelago in NEMO-LIM2 numerical simulations. *The Cryosphere*, 12(4):1233–1247.

Hunke, E. C. and Dukowicz, J. K. (1997). An Elastic–Viscous–Plastic Model for Sea Ice Dynamics. *Journal of Physical Oceanography*, 27(9):1849–1867.

Kowal, S., Gough, W. A., and Butler, K. (2017). Temporal evolution of Hudson Bay Sea Ice (1971–2011). *Theoretical and Applied Climatology*, 127(3):753–760.

Landy, J. C., Ehn, J. K., Babb, D. G., Thériault, N., and Barber, D. G. (2017). Sea ice thickness in the Eastern Canadian Arctic: Hudson Bay Complex & Baffin Bay. *Remote Sensing of Environment*, 200(Supplement C):281 – 294.

Large, W. and Yeager, S. (2004). Diurnal to Decadal Global Forcing For Ocean and Sea-Ice Models: The Data Sets and Flux Climatologies. NCAR/TN-460+STR NCAR Technical Note, National Center for Atmospheric Research.

Lavergne, T., Eastwood, S., Teffah, Z., Schyberg, H., and Breivik, L.-A. (2015). Sea ice motion from low-resolution satellite sensors: An alternative method and its validation in the Arctic. *Journal of Geophysical Research: Oceans*, 115(C10).

Lazier, J., Hendry, R., Clarke, A., Yashayaev, I., and Rhines, P. (2002). Convection and restratification in the Labrador Sea, 1990–2000. *Deep Sea Research Part I: Oceanographic Research Papers*, 49(10):1819 – 1835.

Lindström, G., Pers, C., Rosberg, J., Strömqvist, J., and Arheimer, B. (2010). Development and testing of the HYPE (Hydrological Predictions for the Environment) water quality model for different spatial scales. *Hydrology Research*, 41(3-4):295–319.

Lique, C., Treguier, A. M., Blanke, B., and Grima, N. (2010). On the origins of water masses exported along both sides of Greenland: A Lagrangian model analysis. *Journal of Geophysical Research: Oceans*, 115(C5).

Lozier, M. S., Li, F., Bacon, S., Bahr, F., Bower, A. S., Cunningham, S. A., de Jong, M. F., de Steur, L., deYoung, B., Fischer, J., Gary, S. F., Greenan, B. J. W., Holliday, N. P., Houk, A., Houpert, L., Inall, M. E., Johns, W. E., Johnson, H. L., Johnson, C., Karstensen, J., Koman, G., Le Bras, I. A., Lin, X., Mackay, N., Marshall, D. P., Mercier, H., Oltmanns, M., Pickart, R. S., Ramsey, A. L., Rayner, D., Straneo, F., Thierry, V., Torres, D. J., Williams, R. G., Wilson, C., Yang, J., Yashayaev, I., and Zhao, J. (2019). A sea change in our view of overturning in the subpolar North Atlantic. *Science*, 363(6426):516–521.

MacDonald, M. K., Stadnyk, T. A., Déry, S. J., Braun, M., Gustafsson, D., Isberg, K., and Arheimer, B. (2018). Impacts of 1.5 and 2.0 °C Warming on Pan-Arctic River Discharge Into the Hudson Bay Complex Through 2070. *Geophysical Research Letters*, 0(0).

Madec, G., Delécluse, P., Imbard, M., and Lévy, C. (1998). Opa 8.1 Ocean General Circulation Model reference manual. *Note du Pole de Modélisation*, 11:91p.

Madec, G. and the NEMO team (2008). NEMO ocean engine. *Note du Pole de Modélisation*, (No 27 ISSN No 1288-1619).

Masina, S., Storto, A., Ferry, N., Valdivieso, M., Haines, K., Balmaseda, M., Zuo, H., Drevillon, M., and Parent, L. (2017). An ensemble of eddy-permitting global ocean reanalyses from the MyOcean project. *Climate Dynamics*, 49(3):813–841.

McGovern, P. and Gough, W. (2015). East-West Asymmetry in Coastal Temperatures of Hudson Bay as a Proxy for Sea Ice. *Arctic*, 68(4):445–452.

Müller, V., Kieke, D., Myers, P. G., Pennelly, C., and Mertens, C. (2017). Temperature flux carried by individual eddies across 47°N in the Atlantic Ocean. *Journal of Geophysical Research: Oceans*.

Pett, R., Roff, J., and I.P., M. (1982). Some observations and deductions concerning the deep waters of Hudson Bay. *Naturaliste Canadien*, pages 767–774.

Prinsenberg, S. (1984). Freshwater contents and heat budgets of James Bay and Hudson Bay. *Continental Shelf Research*, 3(2):191 – 200.

Prinsenberg, S. (1986a). Chapter 12 On the Physical Oceanography of Foxe Basin. In Martini, I., editor, *Canadian Inland Seas*, volume 44 of *Elsevier Oceanography Series*, pages 217 – 236. Elsevier.

Prinsenberg, S. (1986b). Chapter 9 Salinity and Temperature Distributions of Hudson Bay and James Bay. *Elsevier Oceanography Series*, 44:163 – 186.

Prinsenberg, S. (1988). Ice-Cover and Ice-Ridge Contributions to the Freshwater Contents of Hudson Bay and Foxe Basin. *Arctic*, 41(1):6–11.

Rawlins, M. A., Steele, M., Holland, M. M., Adam, J. C., Cherry, J. E., Francis, J. A., Groisman, P. Y., Hinzman, L. D., Huntington, T. G., Kane, D. L., Kimball, J. S., Kwok, R., Lammers, R. B., Lee, C. M., Lettenmaier, D. P., McDonald, K. C., Podest, E., Pundsack, J. W., Rudels, B., Serreze, M. C., Shiklomanov, A., Øystein Skagseth, Troy, T. J., Vörösmarty, C. J., Wensnahan, M., Wood, E. F., Woodgate, R., Yang, D., Zhang, K., and Zhang, T. (2010). Analysis of the Arctic System for Freshwater Cycle Intensification: Observations and Expectations. *Journal of Climate*, 23(21):5715–5737.

Reynolds, R. W., Smith, T. M., Liu, C., Chelton, D. B., Casey, K. S., and Schlax, M. G. (2007). Daily High-Resolution-Blended Analyses for Sea Surface Temperature. *Journal of Climate*, 20(22):5473–5496.

Ridenour, N. A., Hu, X., Sydor, K., Myers, P. G., and Barber, D. G. (2019). Revisiting the circulation of Hudson Bay: Evidence for a seasonal pattern. *Geophysical Research Letters*, 46.

Sadler, H. E. (1982). Water flow into Foxe Basin through Fury and Hecla Strait. *Naturaliste Canadien*, pages 701 – 707.

Saucier, F. and Dionne, J. (1998). A 3-D coupled ice-ocean model applied to Hudson Bay, Canada: The seasonal cycle and time-dependent climate response to atmospheric forcing and runoff. *Journal of Geophysical Research–Oceans*, 103(C12):27689 – 27705.

Saucier, F. J., Senneville, S., Prinsenberg, S., Roy, F., Smith, G., Gachon, P., Caya, D., and

Laprise, R. (2004). Modelling the sea ice-ocean seasonal cycle in Hudson Bay, Foxe Basin and Hudson Strait, Canada. *Climate Dynamics*, 23(3/4):303 – 326.

Shiklomanov, I. A. and Shiklomanov, A. I. (2003). Climatic Change and the Dynamics of River Runoff into the Arctic Ocean. *Water Resources*, 30(6):593–601.

Smith, G. C., Roy, F., Mann, P., Dupont, F., Brasnett, B., Lemieux, J.-F., Laroche, S., and Bélair, S. (2014). A new atmospheric dataset for forcing ice–ocean models: Evaluation of reforecasts using the Canadian global deterministic prediction system. *Quarterly Journal of the Royal Meteorological Society*, 140(680):881–894.

Spreen, G., Kaleschke, L., and Heygster, G. (2008). Sea ice remote sensing using AMSR-E 89-GHz channels. *Journal of Geophysical Research: Oceans*, 113(C2). C02S03.

St-Laurent, P., Straneo, F., and Barber, D. G. (2012). A conceptual model of an Arctic sea. *Journal of Geophysical Research: Oceans*, 117(C6).

St-Laurent, P., Straneo, F., Dumais, J.-F., and Barber, D. G. (2011). What is the fate of the river waters of Hudson Bay? *Journal of Marine Systems*, 88:352 – 361.

Straneo, F. (2006). Heat and Freshwater Transport through the Central Labrador Sea. *Journal of Physical Oceanography*, 36(4):606–628.

Straneo, F. and Saucier, F. (2008a). The outflow from Hudson Strait and its contribution to the Labrador Current. *Deep-Sea Research Part I*, 55:926 – 946.

Straneo, F. and Saucier, F. J. (2008b). The Arctic–Subarctic Exchange Through Hudson Strait. In Dickson, R. R., Meincke, J., and Rhines, P., editors, *Arctic–Subarctic Ocean Fluxes: Defining the Role of the Northern Seas in Climate*, pages 249–261. Springer Netherlands, Dordrecht.

Wang, F. and Zhang, J. (2013). Mercury contamination in aquatic ecosystems under a changing environment: Implications for the Three Gorges Reservoir. *Chinese Science Bulletin*, 58(2):141–149.

Yang, J. (2006). The Seasonal Variability of the Arctic Ocean Ekman Transport and Its Role in the Mixed Layer Heat and Salt Fluxes. *Journal of Climate*, 19(20):5366–5387.

Zhang, X., He, J., Zhang, J., Polyakov, I., Gerdes, R., Inoue, J., and Wu, P. (2012). Enhanced poleward moisture transport and amplified northern high-latitude wetting trend. *Nature Climate Change*, 3(1):47 – 51.

Chapter 4

Revisiting the Circulation of Hudson Bay: Evidence for a Seasonal Pattern

Published in Geophysical Research Letters (March 2019). DOI: 10.1029/2019GL082344

Natasha A. Ridenour, Xianmin Hu, Kevin Sydor, Paul G. Myers, David G. Barber

I performed the analysis. X. Hu ran the simulation used in the paper. P.G. Myers provided advice, guidance, and, along with K. Sydor, D.G. Barber, and X. Hu, provided manuscript edits.

Abstract

The Hudson Bay Complex (HBC) is the outlet for many Canadian rivers, receiving roughly 900 km^3/year of river runoff. Historically, studies found a consistent cyclonic flow year-round in Hudson Bay, due to the geostrophic boundary current induced by river discharge and cyclonic wind forcing that was supported by available observations at that time. Using a high resolution ocean general circulation model, we show that, in summer, the mean circulation is not cyclonic, but consists of multiple small cyclonic and anticyclonic features, with the

mean flow directed through the center of the bay. Absolute Dynamic Topography (ADT) and velocity observations also show this seasonal flow pattern. We find that this summer circulation is driven by geostrophic currents, generated by steric height gradients which are induced by increased river discharge during the spring freshet, and reinforced by anticyclonic seasonal wind patterns.

4.1 Introduction

The Hudson Bay Complex (HBC; Figure 4.1), receives about 900 km^3/year of river discharge, roughly equal to 25% of what enters the Arctic Ocean (Shiklomanov and Shiklomanov, 2003). Hudson Bay is a shallow, inland sea, with two main sources of freshwater: sea ice melt and river discharge, which have maximum freshwater input during spring and summer, the time of both the spring freshet and sea ice melt (Prinsenberg, 1988). The river discharge induces a geostrophic boundary current, historically believed to generate year-round cyclonic flow in Hudson Bay.

Hudson Bay experiences a full sea ice cycle, being completely ice covered from December–May, as discovered in the late 1940s (Hare and Montgomery, 1949), and ice free from July–September. The spatial distribution of sea ice in Hudson Bay is associated with regional to large scale atmospheric patterns (Wang et al., 1994b), as well as basin-scale ocean forcing. Ocean currents lead to ice export out of Hudson Bay to Hudson Strait between Southampton Island and Quebec, while wind forcing is responsible for the accumulation of sea ice along the southern and eastern coasts in summer (Wang et al., 1994a).

As Hudson Bay receives a significant amount of discharge, it is possible to use chemical tracers to determine the distribution and pathways of riverine water in the bay. Both Granskog et al. (2007) and Granskog et al. (2009) found evidence of riverine water in the interior of the bay, while the highest concentrations of discharge remained along the coast, agreeing with spatial salinity distributions presented by Ingram and Prinsenberg (1998). Extending this analysis, Granskog et al. (2011) found high fractions of river discharge ($> 5\%$) in surface waters in the interior and along the coast. Eastern Hudson Bay was also shown to have higher concentrations of riverine water in the water column compared to the west, corresponding to

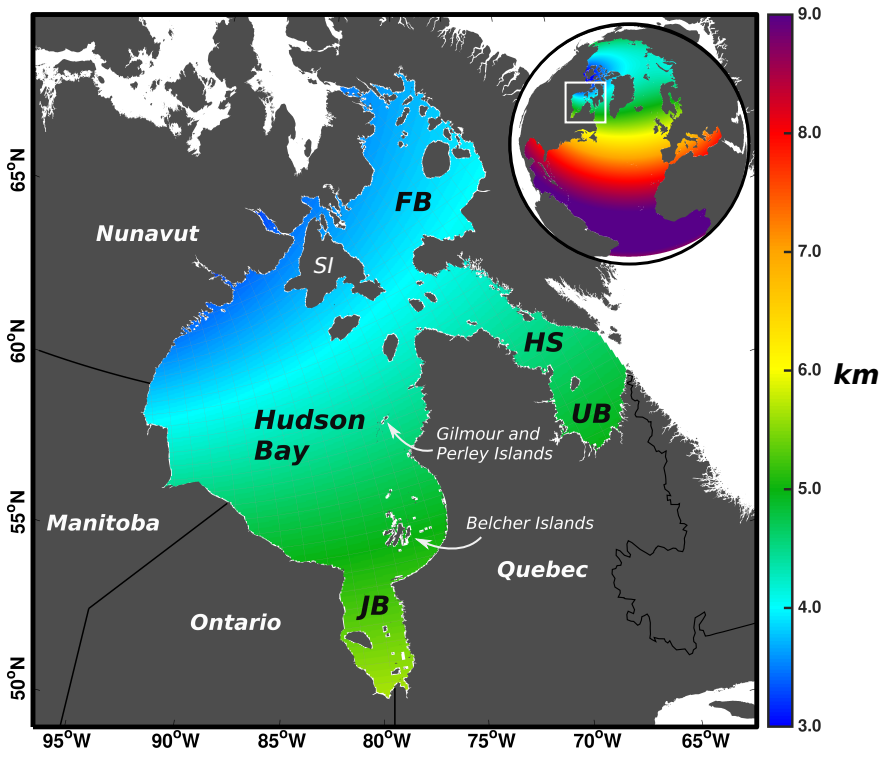

Figure 4.1: Configuration horizontal resolution (colours, in kilometers) in the HBC. Thin grey lines show every 15th mesh grid. The ANHA12 configuration horizontal resolution and model domain is shown in the inset. FB denotes Foxe Basin, HS is Hudson Strait, UB for Ungava Bay, and JB for James Bay. Southampton Island is shown by SI. Several additional geographic features are indicated.

the thickest freshwater layer in James Bay and southeastern Hudson Bay, which decreases northwards (Prinsenberg, 1984) and westwards (Granskog et al., 2011). The interior of Hudson Bay receives freshwater from the boundary via Ekman transport in summer, and in fall, the interior releases this freshwater to the boundary (St-Laurent et al., 2011). In summer, the mean atmospheric forcing is weakly anticyclonic, and reverses to strongly cyclonic in fall. St-Laurent et al. (2011) estimated about 25% of riverine water enters the interior, due to the reversal of the winds in summer.

The annual mean circulation in Hudson Bay is stably cyclonic, as determined by observational drift studies conducted as early as the 1930s (Dunbar, 1982; Prinsenberg, 1986; Hachey, 1935; Ingram and Larouche, 1987). These results were further supported by modelling studies. Summer circulation was modelled by Wang et al. (1994c), who found stable cyclonic circulation in August (using boundary conditions that constrained the circulation to cyclonic flow),

supporting earlier work. While Murty and Yuen (1973) found geostrophic wind stress was an appropriate approximation for simulating cyclonic circulation in September in Hudson Bay, this approximation was not appropriate for the month of May in simulating cyclonic flow. However, Gough et al. (2005) found that the variation in the October–November sea surface height (SSH) at Churchill is influenced by the May–June discharge in James Bay, explaining 47% of the variability from 1964–1983. The authors concluded that 35–50% of James Bay discharge must flow westward, however no velocity observations were available to support this statement. Furthermore, evidence of Hudson Strait waters at intermediate depths in northeastern Hudson Bay during summer months suggest that there could be a reversal of the cyclonic boundary current, allowing these waters to enter the bay (Granskog et al., 2011). A comparison of observed and simulated velocities in the northeastern corner of Hudson Bay in St-Laurent et al. (2012), show a flow reversal from March–May in current observations at 123 m depth, while a weaker flow reversal is observed at 28 m depth. Higher salinities in the boundary current occurred at the same time as these reversal events. Their model also shows signs of flow reversals in this region.

To our knowledge, there has been no study focusing on the existence of a seasonal flow reversal in Hudson Bay. We use a three dimensional (3D) ocean and sea ice coupled model to investigate Hudson Bay circulation in spring and summer, the time of both the spring freshet and ice melt. Satellite and reanalysis data are also used to further support our model results. We find weak anticyclonic circulation in spring and summer in eastern Hudson Bay, which can explain reversals in flow, variability in SSH, and the presence of Hudson Strait water at intermediate depths that have been observed in previous studies. The following section describes the model. In Section 4.3, the seasonal circulation in Hudson Bay and its generation is discussed, preceding the discussion.

4.2 Method

4.2.1 Numerical Model

In this study, a 3D, hydrostatic, primitive equation, ocean–sea ice coupled model, based on the Nucleus for European Modelling of the Ocean version 3.4 (NEMO) (Madec and the

NEMO team, 2008) is used to carry out the simulations. The ice module is the Louvain-la-neuve Ice Model version 2 (LIM2) with elastic-viscous-plastic (EVP) rheology (Hunke and Dukowicz, 1997), including both thermodynamic and dynamic processes (Fichefet and Maqueda, 1997). The model configuration used is the Arctic and Northern Hemisphere Atlantic with 1/12° resolution (ANHA12; Hu et al., 2018). Within the HBC, the horizontal resolution is 3.5–5.5 km (Figure 3.2). In the vertical, there are 50 geopotential levels with the highest resolution ($\sim$ 1 m) in the top 10 m. The simulation was integrated from January 2002 to December 2016 with initial fields (3D temperature, salinity, and horizontal velocities, as well as 2D SSH and sea ice) from GLobal Ocean ReanalYsis and Simulations (GLORYS2v3) produced by Mercator Ocean (Masina et al., 2015). At the surface, high spatial (33 km) and temporal (hourly) resolution atmospheric forcing data (10 m wind, 2 m air temperature and specific humidity, downwelling shortwave and longwave radiation flux, and total precipitation) from the Canadian Meteorological Centre's (CMC) global deterministic prediction system (GDPS) reforecasts (CGRF) described in Smith et al. (2014), are used to drive the model. The GLORYS2v3 dataset is also used to provide data (temperature, salinity, and ocean velocities) at the open boundaries, one near Bering Strait, and the other at 20°S in the Atlantic Ocean. Monthly interannual river discharge, corrected by Dai and Trenberth (Dai et al., 2009; Dai and Trenberth, 2002), as well as Greenland melt water provided by Bamber et al. (2012) is also carefully remapped onto the model grid to have more realistic freshwater input from land to ocean. Discharge entering the ocean is prescribed as the same temperature as the surrounding seawater.

Temperature or salinity restoring is not used in the simulation. Thus, freshwater signals will not be damped. Additionally, our configuration does not use tides as the focus is on large scale processes. The time step is 180 seconds, with 5-day averages being used for our analysis. Throughout this paper, spring refers to May–June which is the time of the spring freshet. Summer, defined as July–September, during the time of the melt season. This was done to separate the effects of freshwater from ice melt and river discharge. Finally, fall is defined as October–December.

4.2.2 Satellite Observations

To evaluate our model simulation, we use daily mean gridded Absolute Dynamic Topography (ADT) and geostrophic velocities with ¼° horizontal resolution. These data are altimeter products produced by Ssalto/Duacs and distributed by Aviso, with support from Cnes (`http://www.aviso.altimetry.fr/duacs/`).

4.2.3 Ocean Reanalysis Data

We also use SSH and surface velocity from the Estimating the Circulation and Climate of the Ocean Phase 2 (ECCO2) project (Forget et al., 2015; Fukumori et al., 2017), which is an ocean reanalysis product using the Massachusetts Institute of Technology general circulation model (MITgcm). Data, provided in 3-day averages, of these two fields from 2004–2015 are used in this study.

4.3 Results

Satellite surface geostrophic velocities for summer and fall are shown in Figure 4.2a and b. In summer, these observations show westward flow along the southern coast of Hudson Bay, and northward flow through the center of the bay (Figure 4.2a). We also see anticyclonic flow around Gilmour and Perley Islands. Northward flow along the western coast as well as a small cyclonic cell in southwestern Hudson Bay are also seen. In fall we see the strong geostrophic boundary current return to the bay, with weaker flow in the interior (Figure 4.2b). Satellite altimetry measurements are unreliable in spring due to the presence of sea ice, and are therefore not shown. However, model data are not limited to ice free periods, therefore we show model surface geostrophic velocities for spring, summer, and fall in Figure 4.2c-e. Modelled spring and summer geostrophic velocities show flow through the center of the bay. Velocities in our model in fall are larger than those shown in observations, however, our model agrees with the Aviso data, also showing the strong cyclonic boundary current at this time of year.

The bottom panels in Figure 4.2 show SSH and surface velocities from the ECCO2 reanalysis dataset. In spring (Figure 4.2f), westward flow is present along the southern coast,

as well as a meandering flow through the center of the bay. Northward flow is noted along the western coast, while southward flow is seen east of the Belcher Islands. During summer, northward flow is present in northeastern Hudson Bay with a cyclonic recirculation cell near the center of the bay. However, in fall, as with the two other datasets, a very clear cyclonic flow returns to the bay.

A comparison of the SSH values from observations and model output in Figure 4.2 show in spring (c,f) and summer (a,d,g) gradients decrease gradually from east to west, with a difference of about 10–15 cm across the bay. In fall however, as the riverine water and sea ice melt are advected northwards along the eastern coast, all datasets show larger SSH gradients along the eastern coast, driving the strong cyclonic flow.

We calculated the spring, summer, and fall mean model barotropic streamfunction, shown in Figure 4.3. The barotropic streamfunction shows lines of constant volume transport, with units of Sv (1 Sv = 10^6 m^3/s). The streamfunction is calculated based on zonal velocity (but with a switch in sign) integrated from south to north. For example, streamfunction values increasing northwards indicate westward flow while streamfunction values decreasing northwards indicate eastward flow. Thus, in Hudson Bay, this corresponds to positive (negative) values for anticyclonic (cyclonic) flow. During spring, we see positive values of the streamfunction in eastern Hudson Bay, while negative values are in the west (Figure 4.3a). Note the scale of the positive and negative values. The region with positive values spans over the eastern area, but is greatly reduced in summer, during ice melt (Figure 4.3b). Positive values are lower in magnitude and in area, before disappearing in the fall (Figure 4.3c), giving way to the cyclonic flow traditionally observed in this region.

To investigate this seasonal flow pattern, and to determine the processes involved, we calculated the spring steric height (Figure 4.4a), and the seasonal cycle for the curl of both Ekman transport and surface stress (bay-wide average; Figure 4.4b). Steric height shows the ocean temperature and salinity contributions to changes in SSH relative to a reference density. Thus, using this metric, we can determine the role of ocean temperature and salinity in SSH variations. We followed Steele and Ermold (2007), where steric height is defined as

$$SH = SH_T + SH_S \tag{4.1}$$

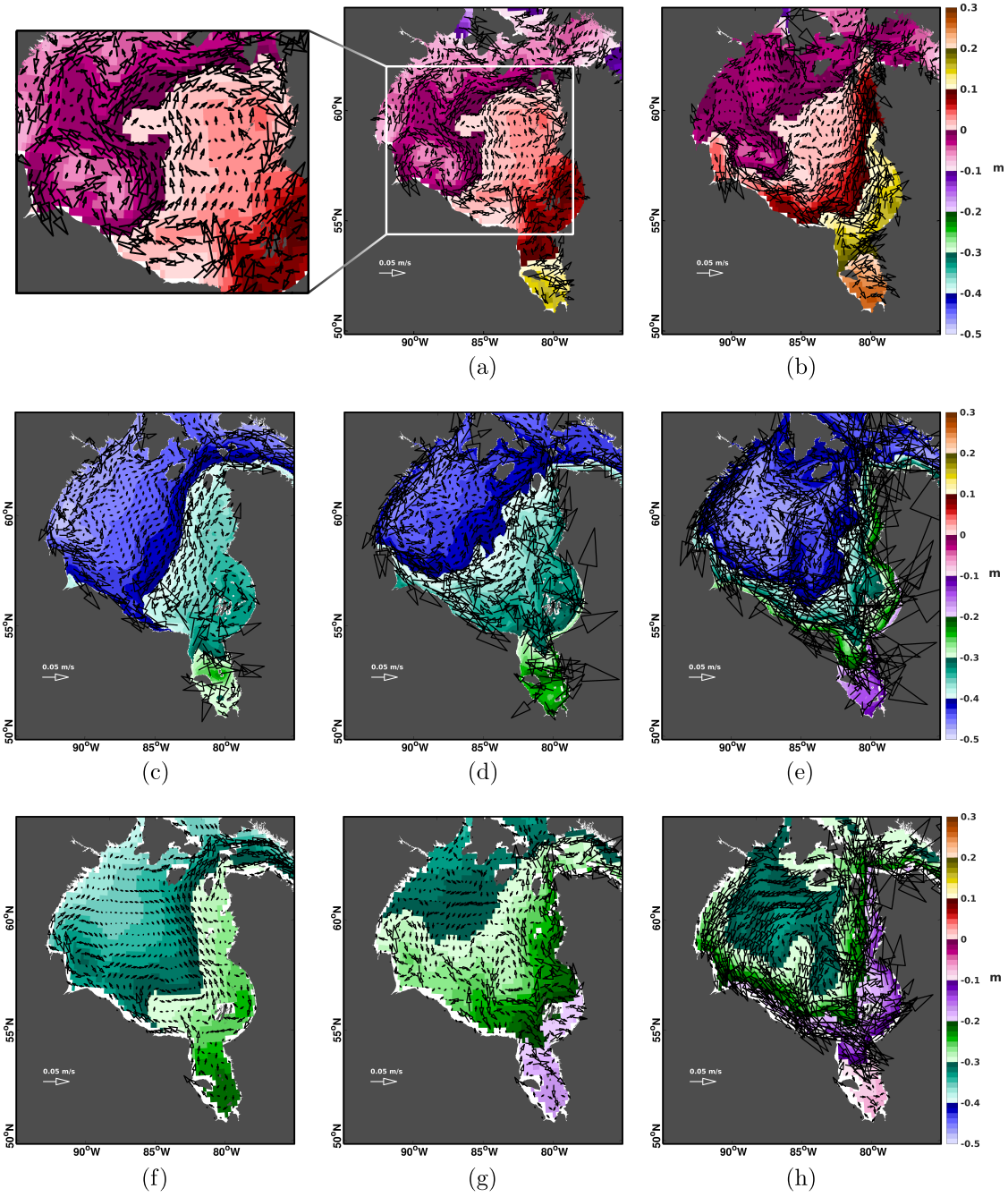

Figure 4.2: Mean 2004–2015 ocean surface variables shown for Aviso (top), our ANHA12 simulation (middle), and ECCO2 reanalysis (bottom). Columns from left to right show spring, summer, and fall. The two Aviso panels (a,b) show observed ADT with corresponding surface geostrophic velocities. ADT is the height above the geoid, and thus can have positive or negative values. Our model SSH and calculated surface geostrophic velocities are shown in panels c-e. Finally, the three ECCO2 panels (f,g,h) show SSH with surface velocities. Note the systematic differences between simulations and observations are due to different height references.

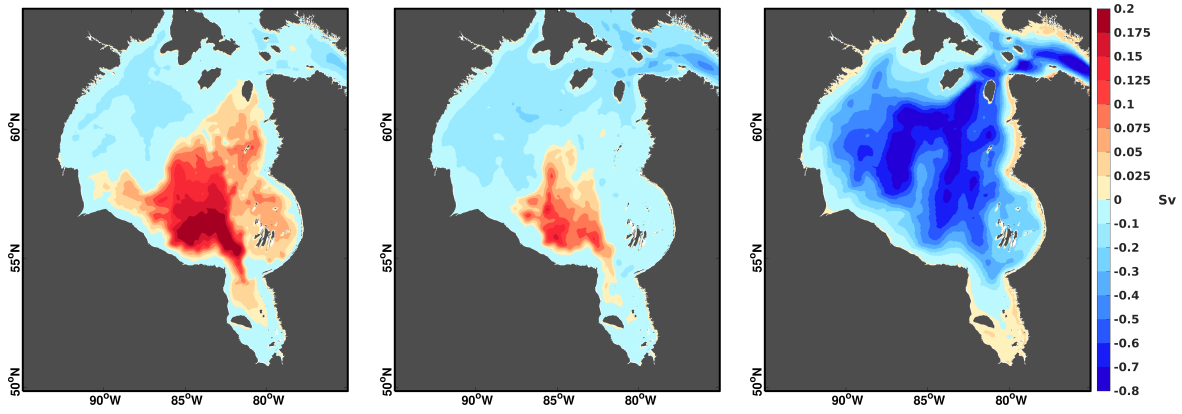

(a) (b) (c)

Figure 4.3: Mean 2004–2015 model barotropic streamfunction for (a) spring, (b) summer, and (c) fall. The streamfunction shows velocity vectors as a 2D scalar value, where the spacing between streamlines provide information on the strength of the flow. Positive (negative) values correspond to anticyclonic (cyclonic) flow.

$$SH_S = \left[\frac{S_{ref}}{\rho_{ref}}\left(\frac{\partial \rho}{\partial S}\right)_{T_{ref},S}\right]\int_{sfc}^{bot}\frac{S_{ref}-S}{S_{ref}}dz \tag{4.2}$$

$$SH_T = \left[\frac{1}{\rho_{ref}^2 c_p}\left(\frac{\partial \rho}{\partial T}\right)_{T,S_{ref}}\right]\int_{sfc}^{bot}\rho_{ref}c_p(T_{ref}-T)dz \tag{4.3}$$

where SH is the steric height, SH_T and SH_S are the thermosteric and halosteric heights respectively. T_{ref} is the reference temperature, which we chose to be -2°C, with S_{ref} being the reference salinity, at 33. The variables S and T are the salinity and temperature of the seawater accordingly. The reference density, ρ_{ref}, is determined by T_{ref} and S_{ref}, and finally, c_p is the heat capacity of water, with a value of 4218 J K^{-1} kg^{-1}. Values inside the square brackets are vertical averages. Steric heights were integrated from the surface to the ocean floor.

In spring, thermosteric heights are negligible (<0.02 m) as the bay is still ice covered. Thus it is the change in salinity that contributes most to steric height in eastern Hudson Bay (Figure 4.4a). Higher steric heights occur in the east and lower steric heights in the west. The spring freshet, followed by high streamflow during the summer months, lowers the salinity of the waters in the bay, causing steric heights to increase, with the largest amounts of river discharge entering James Bay and southeastern Hudson Bay. In agreement with the steric height distribution, the SSH is also higher in the east versus the west (Figure 4.2c) with a difference of over 10 cm. The SSH gradient between western and eastern Hudson Bay

induces a westward flow, but is deflected to the right by the Coriolis force and the resulting geostrophic flow is directed through the center of the bay.

Steric height is not the only process leading to changes in SSH, wind patterns also play a role. Consistent wind forcing in one direction can cause an accumulation of seawater along a coastline, increasing the SSH. The seasonal cycles of bay-wide averaged surface stress curl and the Ekman transport curl are seen in Figure 4.4b. The surface wind stress and Ekman transport curl is positive (negative) when there is cyclonic (anticyclonic) flow. The curl of the surface stress (Figure 4.4b, purple) is positive from January to around the end of March. During April, the surface stress curl dips below zero and from May to June, there is anti-cyclonic surface stress in Hudson Bay, before returning to strong cyclonic surface stress in the fall. The seasonality of the Ekman transport curl (Figure 4.4b, orange) shows cyclonic flow in the winter and fall, however, from June to mid October, Ekman transport is anticy-clonic. Spatially, Ekman transport in eastern Hudson Bay is directed to the west-southwest in May and June (not shown), and rotates to south-southwest in July to September, indicating that the atmosphere might also have a role in seawater accumulation, and increased SSH, in southeastern Hudson Bay.

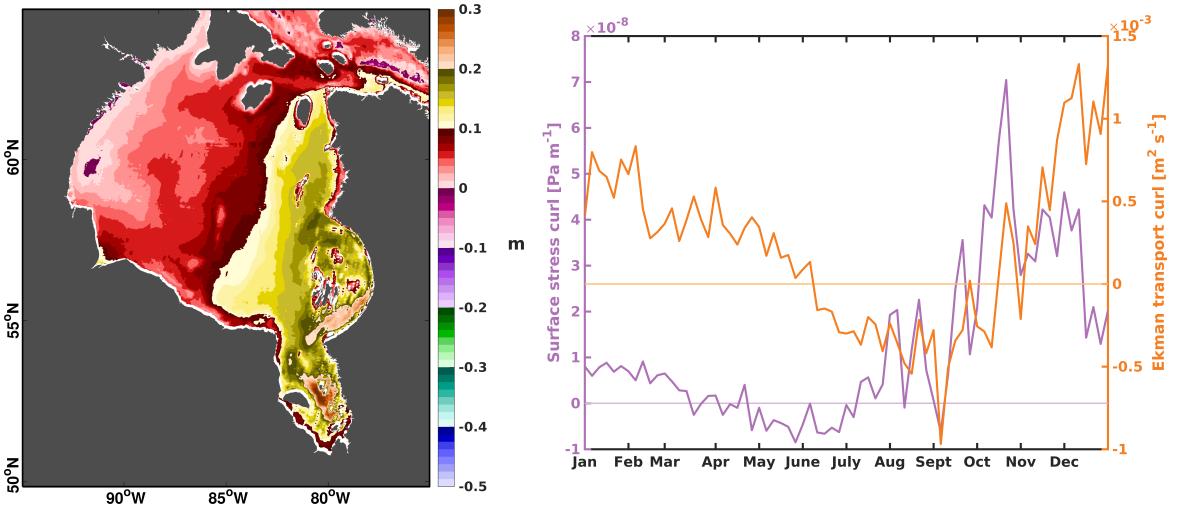

(a) (b)

Figure 4.4: (a) Mean May–June (2004–2015) model halosteric height and (b) seasonal cycles of the surface stress curl (purple) and Ekman transport curl (orange) with zero indicated in each colour. Positive (negative) values of the curl indicate cyclonic (anticyclonic) flow.

The direction of the geostrophic flow is in agreement with the mean summertime barotropic

streamfunction in Figure 4.3 and this pattern is consistent with the transport of freshwater from the boundary to the interior in the summer, as suggested by others (St-Laurent et al., 2011). Export of freshwater in the fall occurs when the SSH gradient weakens in the interior, decreasing freshwater import. Freshwater is then exported out of the interior in the north, while the strong cyclonic geostrophic current returns to the boundary (Figure 4.3). The summer and fall circulation patterns are also reinforced by the mean wind circulation in these seasons.

4.4 Discussion

In this study we investigated seasonal flow patterns in Hudson Bay during spring and summer. Using both observational data and model output, we show circulation in Hudson Bay is not cyclonic year-round. During summer, observations show a small cyclonic cell in southwestern Hudson Bay, and anticyclonic flow in eastern Hudson Bay. Observations from the 1930s (Hachey, 1935) and the 1970s and 1980s, as summarized in Prinsenberg (1986), have implied year long cyclonic circulation in the bay. Annual mean circulation in the bay is cyclonic, due to strong cyclonic flow in fall and winter, however, the weak summer circulation has not been captured.

Our findings help explain why Granskog et al. (2011) found high ($> 5\%$) concentrations of riverine water in the eastern interior of the bay, as well as the presence of Hudson Strait water at intermediate depths in northeastern Hudson Bay in summer. We are not the first to suggest a westward flow in southern Hudson Bay, however, we are the first to propose an update to the spring and summer circulation pattern in this region. Gough et al. (2005) suggest an advective mechanism, induced by wind forcing as well as discharge in James Bay and southeastern Hudson Bay, whereby discharge from James Bay not only goes north along the Quebec coast, but also to the west, impacting the SSH in Churchill in the fall. Interestingly, figure 9 in Saucier et al. (2004), which shows April–June velocities, also implies weak anticyclonic circulation in southeastern Hudson Bay. These studies support our results, yet neither of these papers presented an update to the cyclonic circulation pattern in the bay. Our study pieces together hints of flow reversals from earlier modelling and observational studies to

provide a complete picture of a seasonal circulation pattern in Hudson Bay.

To add further support, we have also investigated the spring/summer circulation in other model simulations with coarser resolution (¼°) and different river discharge forcing (see Supplementary Material; Andersson et al., 2013; Déry et al., 2016; Gelfan et al., 2017; Lindström et al., 2010). In all experiments we find anticyclonic flow in eastern Hudson Bay, with variation in strength due to the discharge dataset used. This indicates that modifications to discharge due to anthropogenic changes (Déry et al., 2011, 2016, 2005; Déry and Wood, 2004; McClelland et al., 2006; Shiklomanov and Shiklomanov, 2003) could have implications on seasonal circulation patterns in this region.

Given our findings, we present schematics of mean fall and spring/summer surface circulation patterns for Hudson Bay in Figure 4.5 based on both model and satellite altimetry analysis shown here. Water from Foxe Basin enters Hudson Bay through Roes Welcome Sound, while water is exported, on average, from Hudson Bay through Southampton Island and Quebec. In spring and summer the circulation changes substantially from the cyclonic circulation previously thought to dominate the flow. Waters continue to flow southward from Foxe Basin through Roes Welcome Sound, however, a cyclonic cell in southwestern Hudson Bay feeds into two currents flowing northwards. One just off of the western Hudson Bay coast, and another that flows northeastward towards Hudson Strait, through the center of the bay. On the eastern side of the bay, waters from James Bay follow SSH contours, which have a local minima along the southern Hudson Bay coast. Flow near the Belcher Islands is generally northwards, while to the west of James Bay, flow is westward before being directed northward. A local maxima of SSH surrounds Gilmour and Perley Islands, leading to anticyclonic circulation in northeastern Hudson Bay. This southward flow near the Quebec coast would help explain the current reversals noted by Granskog et al. (2011) and St-Laurent et al. (2012), where Hudson Strait waters enter Hudson Bay. In fall, circulation in the bay is cyclonic, with the strongest flow along the coast. However, observations show a small cyclonic cell in southwestern Hudson Bay and a moderately strong northeastward flow towards Hudson Strait.

This study has shown that during the year, the circulation in Hudson Bay is not consistently cyclonic, and that during spring and summer, there is weak anticyclonic flow in eastern Hudson

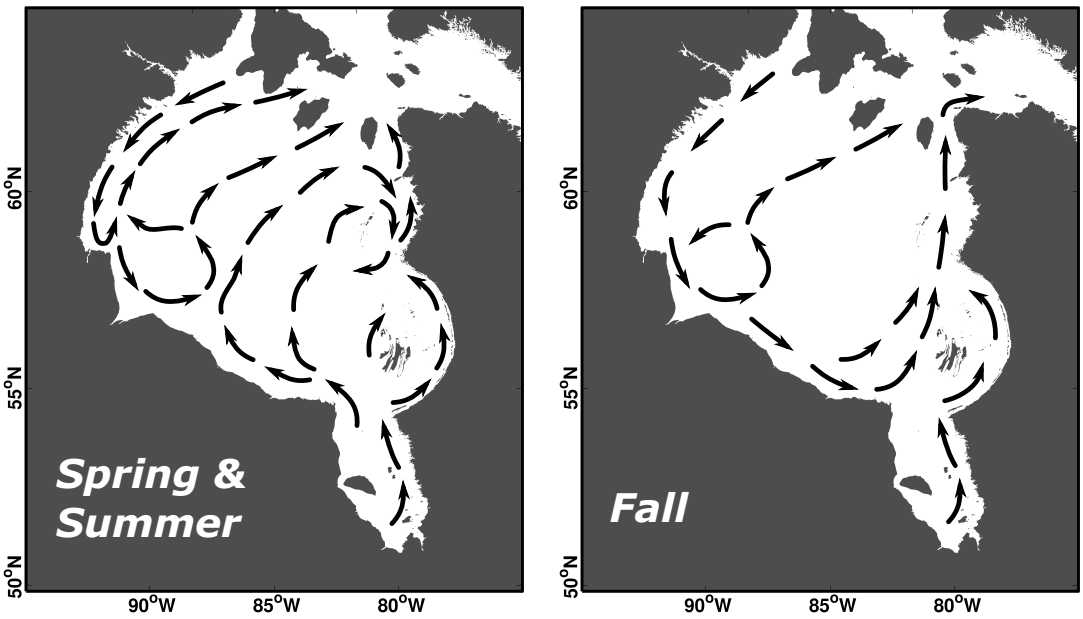

Figure 4.5: Schematics of average spring/summer and fall surface flow patterns that are based on Aviso satellite altimetry data and model output.

Bay. With this seasonal change in circulation, this raises questions regarding the residence time of river discharge in the bay, and how the bay stores and releases freshwater. Additionally, this updated seasonal circulation may provide insights as to the distribution of nutrients and contaminants around the bay. It also highlights the need for increased observations and observing programs in the bay.

Acknowledgments

CGRF forcing fields made available by Environment and Climate Change Canada. We thank the Natural Sciences and Engineering Research Council of Canada and Manitoba Hydro for funding the BaySys project (CRDPJ 470028-14), of which this work is part of. This work could not have been possible without the computational resources provided by Westgrid and Compute Canada. Observational data provided by Aviso are greatly appreciated for model evaluation, as well as the use of surface fields from the ECCO2 project. We thank Dr. J. Bamber for the use of the Greenland melt dataset, and Dr. Gregory Smith for the use of the CGRF atmospheric forcing. Additionally, we are grateful for the use of GLORYS for initializing our model experiments and forcing the model open boundaries.

Appendix 4.A: Supplementary Material

Additional figures shown in the supplementary information use the ¼° version of the ANHA configuration (ANHA4). We note the differences between the 1/12° and ¼° configurations are related to the spatial resolution as well as the time step used. Horizontal resolution in ANHA4 is 10–17 km in the HBC, however the vertical resolution remains the same. The ANHA4 simulations also use a coarser time step of 1080 seconds, though 5-day averaged output is still used for our analysis.

The supplementary figures include three model runs. The first, CTRL is the ¼° twin of the ANHA12 simulation used in the paper, with the only difference being the resolution (and corresponding time step and mixing parameters). This simulation also uses the corrected monthly interannual runoff from Dai and Trenberth (Dai et al., 2009; Dai and Trenberth, 2002). The two other simulations use different river runoff forcing from HYdrological Predictions for the Environment (HYPE; Andersson et al., 2013; Gelfan et al., 2017; Lindström et al., 2010). One of the HYPE datasets uses the uncalibrated version of HYPE which has been integrated with observed stream flow where available, using gap-filled observations from Déry et al. (2016). Observations in this dataset account for 58% of the HBC drainage basin. We note, however, that flow through La Grande Riviere are underestimated in this dataset. We refer to this integrated, uncalibrated HYPE dataset as HIUC (and subsequently the model simulation that uses it). This dataset extends to 2010, so for years after 2010, 2010 discharge is used. The second HYPE dataset used is from the calibrated version of HYPE, and has not been integrated with observations. We will refer to this dataset (and corresponding simulation) as HCAL. This dataset extends to 2013, and as before, years after 2013 are forced with 2013 discharge. Thus, using different runoff datasets can provide information on how sensitive this circulation pattern is to discharge. Averaging the common years of each dataset (2004-2007), the DT dataset has the most runoff entering the HBC throughout the year with 2.99 km^3/day, this is followed by HCAL releasing 2.54 km^3/day into the HBC. The HIUC dataset has the lowest amount of discharge, with 2.45 km^3/day.

To compliment Figure 4.2, Figure S4.1 shows sea surface height (SSH) and calculated model geostrophic velocities for three additional simulations that use different runoff forcing.

In spring, in all three simulations, we see westward flow along the southern coast, west of James Bay, and recirculation around Gilmour and Perley Islands. The largest velocities appear through the center of the bay, though in the case of the HIUC simulation, this flow is shifted to the east compared to the two other simulations. Lower SSH values are also present in HIUC. During summer, the fastest currents are through the center of the bay, but also along the eastern coast. In all three simulations, flow north of James Bay is meandering. In HIUC, the simulation with the least runoff, flow through the bay is stronger around Gilmour and Perley Islands. In fall, all simulations show a strong cyclonic boundary current.

Figure S4.2 shows the spring (May-June) and summer (July-September) barotropic streamfunction for the three ¼° experiments. Given the distribution of the streamfunction values, red colours correspond to anticyclonic while blue colours correspond to cyclonic flow. In all three cases, the gradient of streamfunction values are largest along the southern coast in spring where the largest values are located. Positive values of the streamfunction extend north spanning over the eastern region of the bay. Between simulations we see smaller gradients in the HUIC experiment where we have the least amount of discharge. Larger gradients are seen both in HCAL and CTRL, indicating volume and location of discharge are important. During the summer months streamfunction values are weaker, as seen in the ANHA12 simulation, as well as cover a smaller region in the bay, with positive values remaining only along the southern coast.

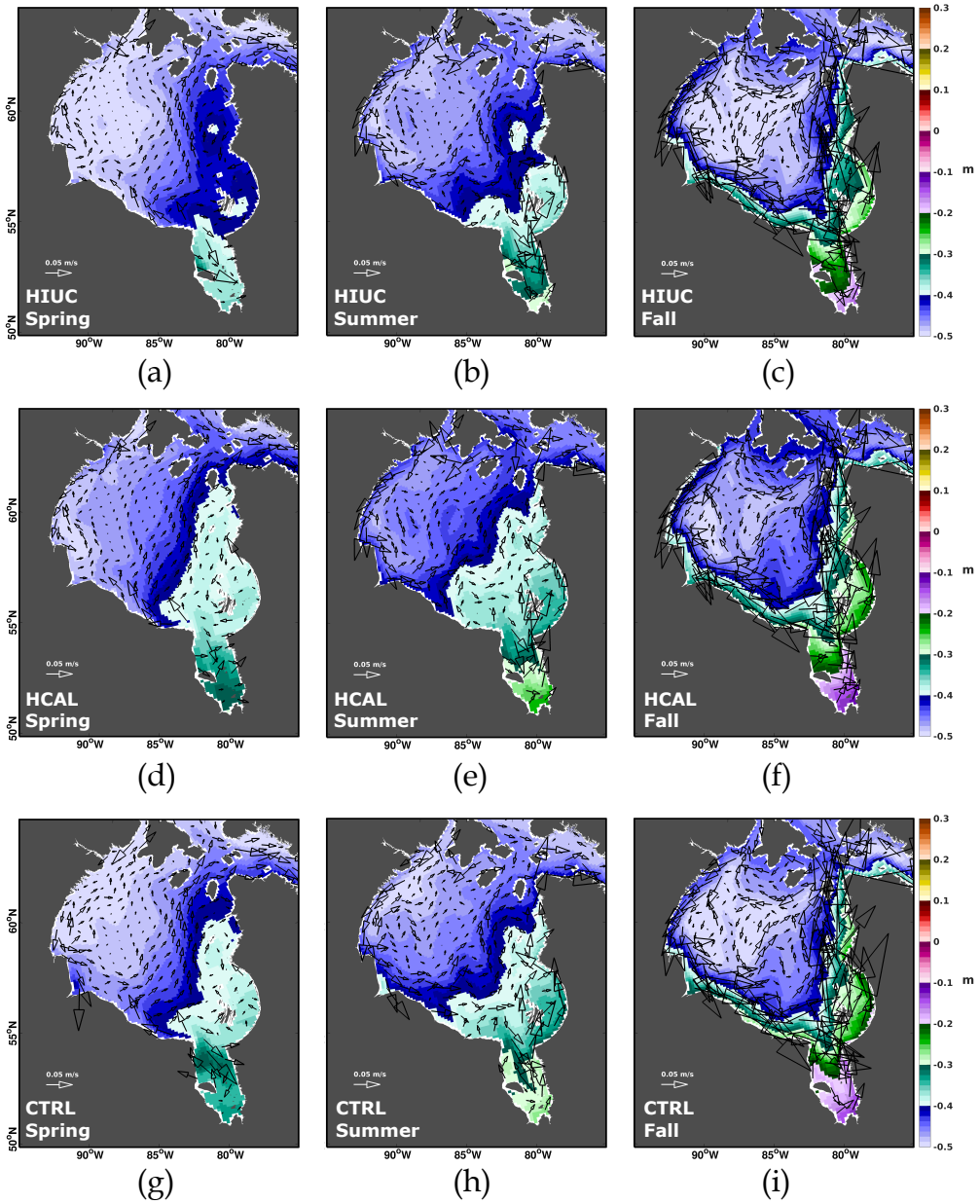

Figure S4.1: Modelled geostrophic velocities and sea surface height (SSH) averaged from 2004-2015 for three ¼° model simulations. Columns show spring (May-June), summer (July-September), and fall (October-December) averages for the HIUC, HCAL, and CTRL simulations described earlier.

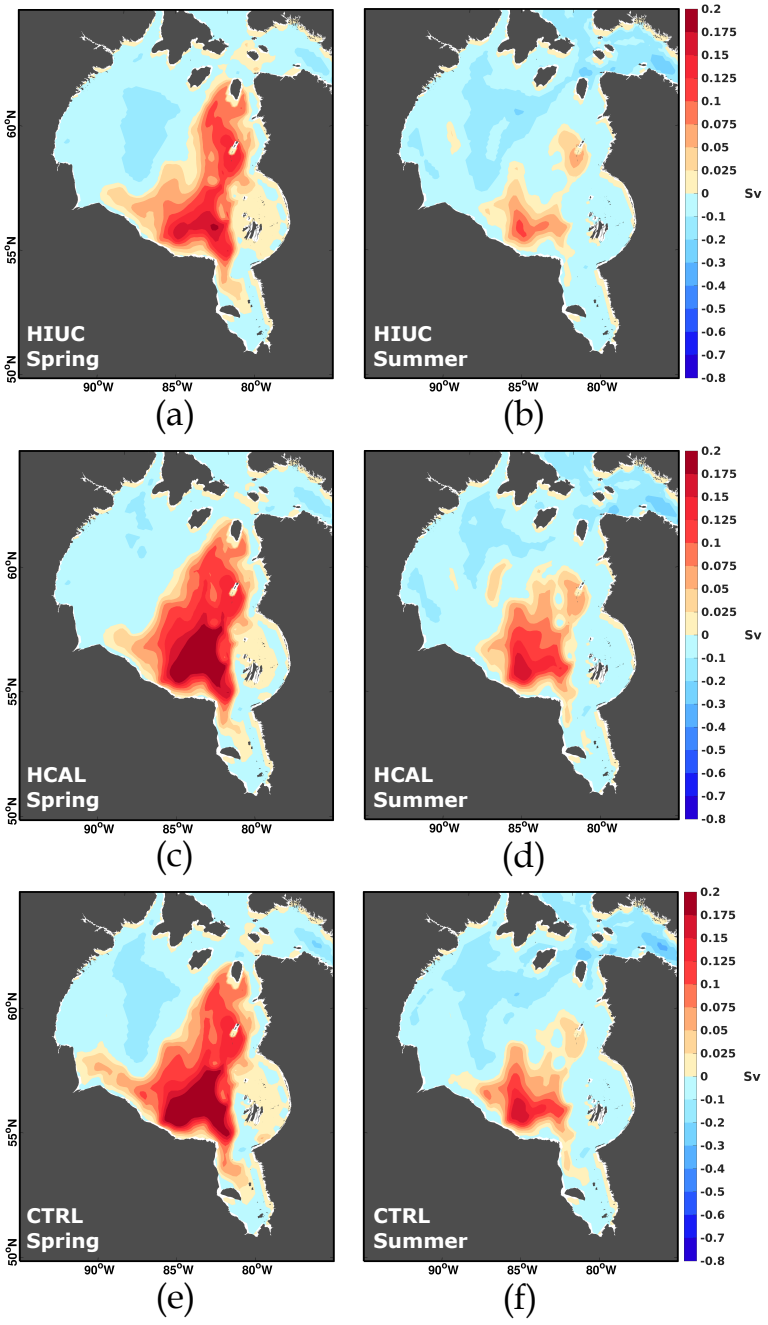

Figure S4.2: Calculated modelled spring (left column) and summer (right column) barotropic streamfunctions (2004-2015) for three ¼° model simulations, HIUC (top), HCAL (middle), and CTRL (bottom).

Bibliography

Andersson, J. C. M., Pechlivanidis, I. G., Gustafsson, D., Donnelly, C., and Arheimer, B. (2013). Key factors for improving large-scale hydrological model performance. In Lekkas, T., editor, *Proceedings of the 13th International Conference on Environmental Science and Technology*, Proceedings of the International Conference on Environmental Science and Technology, pages 77–88, Univ, Aegean, 30, Voulgaroktonou Str, Athens, GR 114 72, Greece. Univ Aegean; Global Network Environm Sci & Technol, Global Nest, Secritariat. 13th International Conference on Environmental Science and Technology (CEST), Athens, Greece, Sep 05-07, 2013.

Bamber, J., van den Broeke, M., Ettema, J., Lenaerts, J., and Rignot, E. (2012). Recent large increases in freshwater fluxes from Greenland into the North Atlantic. *Geophysical Research Letters*, 39(19).

Dai, A., Qian, T., Trenberth, K. E., and Milliman, J. D. (2009). Changes in continental freshwater discharge from 1948 to 2004. *Journal of Climate*, 22(10):2773–2792.

Dai, A. and Trenberth, K. E. (2002). Estimates of Freshwater Discharge from Continents: Latitudinal and Seasonal Variations. *Journal of Hydrometeorology*, 3(6):660–687.

Déry, S. J., Mlynowski, T. J., Hernández-Henríquez, M. A., and Straneo, F. (2011). Interannual variability and interdecadal trends in Hudson Bay streamflow. *Journal of Marine Systems*, 88:341 – 351.

Déry, S. J., Stadnyk, T. A., MacDonald, M. K., and Gauli-Sharma, B. (2016). Recent trends and variability in river discharge across northern Canada. *Hydrology and Earth System Sciences*, 20(12):4801 – 4818.

Déry, S. J., Stieglitz, M., and McKenna, E. C. (2005). Characteristics and Trends of River Discharge into Hudson, James, and Ungava Bays, 1964–2000. *Journal of Climate*, 18(14):2540–2557.

Déry, S. J. and Wood, E. F. (2004). Teleconnection between the Arctic Oscillation and Hudson Bay river discharge. *Geophysical Research Letters*, 31(18).

Dunbar, M. (1982). Oceanographic research in Hudson and James Bays. *Le Naturaliste Canadien*, 109(4):677 – 683.

Fichefet, T. and Maqueda, M. A. M. (1997). Sensitivity of a global sea ice model to the treatment of ice thermodynamics and dynamics. *Journal of Geophysical Research: Oceans*, 102(C6):12609–12646.

Forget, G., Campin, J.-M., Heimbach, P., Hill, C. N., Ponte, R. M., and Wunsch, C. (2015). ECCO version 4: an integrated framework for non-linear inverse modeling and global ocean state estimation. *Geoscientific Model Development*, 8(10):3071–3104.

Fukumori, I., Wang, O., Fenty, I., Forget, G., Heimbach, P., and Ponte, R. M. (2017). ECCO version 4 release 3. Technical report. Available at `ftp://ecco.jpl.nasa.gov/Version4/Release3/doc/v4r3_estimation_synopsis.pdf`.

Gelfan, A., Gustafsson, D., Motovilov, Y., Arheimer, B., Kalugin, A., Krylenko, I., and Lavrenov, A. (2017). Climate change impact on the water regime of two great Arctic rivers: modeling and uncertainty issues. *Climatic Change*, 141(3):499–515.

Gough, W. A., Robinson, C., and Hosseinian, R. (2005). The Influence of James Bay River Discharge on Churchill, Manitoba Sea Level. *Polar Geography*, 29(3):213–223.

Granskog, M. A., Kuzyk, Z. Z. A., Azetsu-Scott, K., and Macdonald, R. W. (2011). Distributions of runoff, sea-ice melt and brine using δ^{18}O and salinity data — A new view on freshwater cycling in Hudson Bay. *Journal of Marine Systems*, 88:362 – 374.

Granskog, M. A., Macdonald, R. W., Kuzyk, Z. Z. A., Senneville, S., Mundy, C.-J., Barber, D. G., Stern, G. A., and Saucier, F. (2009). Coastal conduit in southwestern Hudson Bay (Canada) in summer: Rapid transit of freshwater and significant loss of colored dissolved organic matter. *Journal of Geophysical Research: Oceans*, 114(C8).

Granskog, M. A., Macdonald, R. W., Mundy, C.-J., and Barber, D. G. (2007). Distribution, characteristics and potential impacts of chromophoric dissolved organic matter (CDOM) in Hudson Strait and Hudson Bay, Canada. *Continental Shelf Research*, 27(15):2032 – 2050.

Hachey, H. B. (1935). Circulation of Hudson Bay water as indicated by drift bottles. *Science*, 82:275 – 276.

Hare, F. and Montgomery, M. (1949). Ice, Open Water, and Winter Climate in the Eastern Arctic of North America: Part 2. *Arctic*, 2(3):149–164.

Hu, X., Sun, J., Chan, T. O., and Myers, P. G. (2018). Thermodynamic and dynamic ice thickness contributions in the Canadian Arctic Archipelago in NEMO-LIM2 numerical simulations. *The Cryosphere*, 12(4):1233–1247.

Hunke, E. C. and Dukowicz, J. K. (1997). An elastic–viscous–plastic model for sea ice dynamics. *Journal of Physical Oceanography*, 27(9):1849–1867.

Ingram, R. G. and Larouche, P. (1987). Variability of an under-ice river plume in Hudson Bay. *Journal of Geophysical Research: Oceans*, 92(C9):9541–9547.

Ingram, R. G. and Prinsenberg, S. (1998). *Coastal Oceanography of Hudson Bay and Surrounding Eastern Canadian Arctic Waters Coastal Segment*, volume 11, pages 835–861. John Wiley and Sons, Toronto.

Lindström, G., Pers, C., Rosberg, J., Strömqvist, J., and Arheimer, B. (2010). Development and testing of the HYPE (Hydrological Predictions for the Environment) water quality model for different spatial scales. *Hydrology Research*, 41(3-4):295–319.

Madec, G. and the NEMO team (2008). NEMO ocean engine. *Note du Pole de Modélisation*, (No 27 ISSN No 1288-1619).

Masina, S., Storto, A., Ferry, N., Valdivieso, M., Haines, K., Balmaseda, M., Zuo, H., Drevillon, M., and Parent, L. (2017). An ensemble of eddy-permitting global ocean reanalyses from the MyOcean project. *Climate Dynamics*, 49(3):813–841.

McClelland, J. W., Déry, S. J., Peterson, B. J., Holmes, R. M., and Wood, E. F. (2006). A pan-arctic evaluation of changes in river discharge during the latter half of the 20th century. *Geophysical Research Letters*, 33(6).

Murty, T. S. and Yuen, K. B. (1973). Balanced Versus Geostrophic Wind-Stress for Hudson Bay. *Journal of the Fisheries Research Board of Canada*, 30(1):53–62.

Prinsenberg, S. (1984). Freshwater contents and heat budgets of James Bay and Hudson Bay. *Continental Shelf Research*, 3(2):191 – 200.

Prinsenberg, S. (1986). Chapter 10 The Circulation Pattern and Current Structure of Hudson Bay. *Elsevier Oceanography Series*, 44:187 – 204.

Prinsenberg, S. (1988). Ice-Cover and Ice-Ridge Contributions to the Freshwater Contents of Hudson Bay and Foxe Basin. *Arctic*, 41(1):6–11.

Saucier, F. J., Senneville, S., Prinsenberg, S., Roy, F., Smith, G., Gachon, P., Caya, D., and Laprise, R. (2004). Modelling the sea ice-ocean seasonal cycle in Hudson Bay, Foxe Basin and Hudson Strait, Canada. *Climate Dynamics*, 23(3/4):303 – 326.

Shiklomanov, I. A. and Shiklomanov, A. I. (2003). Climatic Change and the Dynamics of River Runoff into the Arctic Ocean. *Water Resources*, 30(6):593–601.

Smith, G. C., Roy, F., Mann, P., Dupont, F., Brasnett, B., Lemieux, J.-F., Laroche, S., and Bélair, S. (2014). A new atmospheric dataset for forcing ice–ocean models: Evaluation of reforecasts using the Canadian global deterministic prediction system. *Quarterly Journal of the Royal Meteorological Society*, 140(680):881–894.

St-Laurent, P., Straneo, F., and Barber, D. G. (2012). A conceptual model of an Arctic sea. *Journal of Geophysical Research: Oceans*, 117(C6).

St-Laurent, P., Straneo, F., Dumais, J.-F., and Barber, D. (2011). What is the fate of the river waters of Hudson Bay? *Journal of Marine Systems*, 88:352 – 361.

Steele, M. and Ermold, W. (2007). Steric Sea Level Change in the Northern Seas. *Journal of Climate*, 20(3):403–417.

Wang, J., Mysak, L., and Ingram, R. (1994a). A numerical-simulation of sea-ice cover in Hudson Bay. *Journal of Physical Oceanography*, 24(12):2515 – 2533.

Wang, J., Mysak, L. A., and Ingram, R. G. (1994b). Interannual variability of sea–ice cover in Hudson Bay, Baffin Bay and the Labrador Sea. *Atmosphere-Ocean*, 32(2):421–447.

Wang, J., Mysak, L. A., and Ingram, R. G. (1994c). A three-dimensional numerical simulation of Hudson Bay summer ocean circulation: Topographic gyres, separations, and coastal jets. *Journal of Physical Oceanography*, 24(12):2496–2514.

Chapter 5

Hudson Strait Inflow: Structure and Variability

Soon to be submitted for publication to Journal of Geophysical Research: Oceans.

Abstract

Hudson Strait is the main pathway of heat, mass, and freshwater exchange between Hudson Bay and the Arctic and North Atlantic Oceans. Flow along the southern coast, a low saline, baroclinic jet directed towards the North Atlantic, has received more attention due to its potential impact on deep convection in the Labrador Sea. However, details about the westward, barotropic flow along the northern coast of Hudson Strait remain unknown due to a scarcity of observations. This is even though the Hudson Strait inflow waters affect the physical and biogeochemical systems of the bay, as well as the marine ecosystem, which supports the livelihoods of many Indigenous communities surrounding the Hudson Bay Complex. Here, we address this gap by analyzing data from two hydrographic surveys across Hudson Strait from 2008 and 2009, as well as data from four moorings deployed in the strait. Three moorings were deployed on the northern side of the strait to map the inflow, and one was deployed on the southern side of the strait to capture the outflow. Both the mooring data and the summer surveys reveal that the inflow into and outflow from the strait are characterized by two very different flows. Along the southern side, a stratified, fresh outflow is present

(consistent with earlier studies), with the strongest flow in the winter coinciding with the previous year's spring freshet. Variability in the outflow velocities occurs mainly at the surface. Along the northern coast, the inflow is a weakly stratified, saline flow, with seasonality that is distributed throughout the water column. Source waters of the inflow appear to stem mainly from Arctic Water in the Baffin Island Current, with small contributions from Transitional and West Greenland Irminger Waters. Pathways of the Hudson Strait inflow continue to remain an area of speculation, though we suggest that the majority of the inflow enters northern Hudson Bay, with some inflow waters potentially entering into Foxe Basin.

5.1 Introduction

Increased freshwater (low salinity water) transport to the North Atlantic from melting Arctic sea ice, increased discharge from Greenland, as well as an intensified hydrological cycle (Bamber et al., 2018; Haine et al., 2015) is of concern due to its potential impact on deep convection sites, such as the Nordic and Labrador Seas (Aagaard and Carmack, 1989; Bamber et al., 2012; Yang et al., 2016). These deep convection sites play an important role in the Meridional Overturning Circulation (MOC), which helps regulate global temperatures, as well as ventilate the deep ocean and sequester atmospheric carbon dioxide (Kuhlbrodt et al., 2007; McKinley et al., 2017; Stocker et al., 2013). Not only that, increased freshwater from the Arctic also affects the dynamics, heat loss, and biogeochemistry of the North Atlantic, as was the case during the Great Salinity Anomaly (Gelderloos et al., 2012; Jahn and Holland, 2013; Stocker et al., 2013). There are three main gateways where oceanic freshwater enters the North Atlantic from the Arctic Ocean; east of Greenland lies Fram Strait while Davis Strait lies to the west. The third gateway is Hudson Strait, located southwest of Greenland (Figure 5.1). Of these three gateways, the net freshwater flux from Hudson Strait (38 mSv relative to 34.8, where 1 mSv=1000 m^3/s) is about 40% of that from Davis Strait (93 mSv; Curry et al., 2014), both of which flow directly into the Labrador Sea (Straneo and Saucier, 2008a,b).

However, Hudson Strait remains relatively understudied. Present day fluxes and variability through Hudson Strait are based on mooring deployments mapping the southern side of the

strait from 2004-2006, as well as an 8-week deployment (mid-August to mid-October) in 1982 that sought to map the flow across the whole strait (Drinkwater, 1988; Straneo and Saucier, 2008a; Sutherland et al., 2011). Year long data describing the flow on the northern side of the strait has yet to be presented. Meanwhile, flow (including ice fluxes) through Davis Strait has been estimated using data from 1987–1990 and 2004–2010 (Cuny et al., 2005; Curry et al., 2014), and fluxes through Fram Strait have been estimated using moorings located in the deep regions of the strait (spanning 1997 to present day), while shallow regions, specifically along the east Greenland coast, are mapped by hydrographic sections (Beszczynska-Möller et al., 2015; Rabe et al., 2013; Schauer et al., 2008). Regardless of the gate, obtaining data in polar regions, specifically freshwater fluxes, continue to be a challenge in polar research.

The Hudson Bay region is connected to the Arctic Ocean via the Canadian Arctic Archipelago, through Fury and Hecla Strait, a narrow, shallow passage that has a small volume and freshwater flux into northern Foxe Basin (Barber, 1965; Ridenour et al., 2019a; Sadler, 1982), while Hudson Strait connects the region to the North Atlantic. Thus, Hudson Strait is the main gate connecting the Hudson Bay Complex (HBC) with the global ocean, specifically the North Atlantic, providing the Labrador Current with half of its freshwater, and 15% of its volume (Straneo and Saucier, 2008a). Rivers provide the majority of this flux, as nearly 900 km^3/year of river discharge enters the HBC (Déry et al., 2005; Ridenour et al., 2019a), draining over a third of the Canadian land area. Thus the HBC receives an amount of freshwater that is nearly equivalent to the average annual (2007–2016) freshwater flux from Greenland (Bamber et al., 2018). The riverine water laden outflow from Hudson Strait flows along the Labrador coast to Newfoundland, where freshwater signals from Hudson Strait have been detected (Florindo-López et al., 2020; Myers et al., 1990; Sutcliffe Jr. et al., 1983). However, pathways and the role of Hudson Strait and its freshwater outflow in the North Atlantic remain unknown.

Hudson Strait inflow, is the largest source of oceanic water into the HBC, with Fury and Hecla Strait importing a small amount of Arctic Water into northern Foxe Basin. Knowing the waters that enter the bay is key to understanding water mass transformations and other processes occurring in the bay. At the same time, communities surrounding the HBC depend on the region for resupply ships, trade, transport, as well as cultural and social practices

(Babb et al., 2019). Most of these activities revolve around the seasonal ice cover in the region, that is currently undergoing change (Castro de la Guardia et al., 2017), making the future uncertain for some of these activities.

Hudson Strait is about 100 km wide and 400 km long, oriented northwest-southeast (Figure 5.1). Northwestern Hudson Strait is connected to Foxe Basin in the north and Hudson Bay to the south. Depths in this region are around 200-300 m, though depths reach 900 m in eastern Hudson Strait where it connects to the Labrador Sea. Eastern Hudson Strait is under greater influence from the Labrador Sea, with warmer and more saline waters, while in western Hudson Strait, waters are less saline and cooler (Drinkwater, 1988).

Tides in this region are large and semidiurnal, with average amplitudes ranging from 3-10 m depending on location, and are mostly barotropic (Arbic et al., 2007; Easton, 1972; Drinkwater, 1988; O'Reilly et al., 2005). Associated tidal currents can reach up to 1 m/s, and are directed along strait (Drinkwater, 1988; Straneo and Saucier, 2008b). Internal tides are also large in Hudson Strait (Saucier et al., 2004).

The flow in Hudson Strait can be separated into the fresh, baroclinic, eastward outflow along the southern coast, and a more saline, barotropic, westward inflow along the northern coast (Drinkwater, 1988). Riverine sourced water feeds the outflow by flowing into Hudson Strait from Hudson Bay between Southampton Island and northwestern Quebec. It has been estimated that the net flow through Hudson Strait is equal to the flow through Fury and Hecla Strait plus the added river discharge in the HBC (Drinkwater, 1988). The temperature of the outflow is near or at freezing for the majority of the year, with summer time heating leading to maximum temperatures in September (Straneo and Saucier, 2008a). Vertically, the outflow also shows a temperature maximum at depth, due to sheared flow advecting heat below (Straneo and Saucier, 2008a). A cold layer lies between 100-200 m, with warm, saline waters at the bottom of the water column (Drinkwater, 1988). Peak freshwater (or minimum in salinity) occurs between October and December, with maximum salinity from March to May (Straneo and Saucier, 2008a). Salinity in the outflow is largely influenced by the seasonality of river discharge from Hudson and James Bays. Stratification in the outflow is strong and persistent throughout the whole year. The outflow is directed along strait, with the largest velocities at the surface, and strong vertical shear (Straneo and Saucier, 2008a).

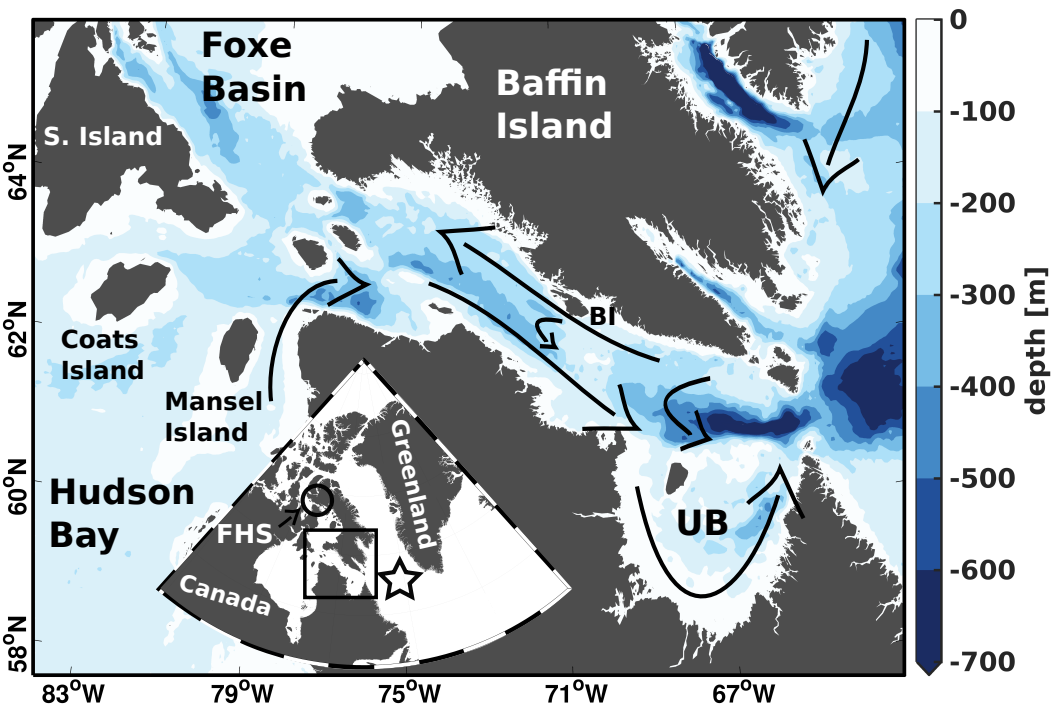

Figure 5.1: Bathymetry of Hudson Strait with known circulation shown. Inset shows location of the strait and its proximity to the Labrador Sea deep convection site indicated by the star in the inset. Fury and Hecla Strait is denoted by FHS and indicated by the black circle. Other geographical features are indicated with S. Island showing Southampton Island, BI indicating Big Island, and UB showing Ungava Bay.

Throughout the year, higher along strait velocities are noted in the fall, with lower velocities in the winter and spring. The width of the outflow is estimated to be about 40 km (Straneo and Saucier, 2008a).

High frequency variability in the outflow is mostly caused by low salinity, anticyclonic eddies, which have an average diameter of 50 km. These eddies are generated by storms passing over Hudson Bay that accelerate flow in the cyclonic boundary current (Sutherland et al., 2011). Buoyancy and rotation forces act on the accelerated flow en route from Hudson Bay to Hudson Strait to generate anticyclonic eddies (Sutherland et al., 2011). These eddies account for 40% of the volume and 50% of the freshwater transport in the outflow (Sutherland et al., 2011).

Less is known about the Hudson Strait inflow. The inflow is barotropic, homogeneous and has been thought to be a continuation of the Baffin Island Current (Drinkwater, 1988). Upstream, around 63°N, the Baffin Island Current separates into two branches. The western

branch enters Hudson Strait, while the eastern branch flows southward to join the Hudson Strait outflow in the Labrador Current south of Hudson Strait (LeBlond et al., 1981). Volume transport in the inflow is estimated to be 0.82-0.84 Sv, with a freshwater transport of 41 mSv (S_{ref} = 34.8; Drinkwater, 1988; Straneo and Saucier, 2008b). Straneo and Saucier (2008a) speculate that about 25% of the Davis Strait volume flux and 35% of its freshwater goes into Hudson Strait. The outflow has a volume transport of 1-1.2 Sv and an associated freshwater flux of 79 mSv (S_{ref} = 34.8; Straneo and Saucier, 2008b).

Exchange between the inflow and outflow occurs with the cross channel flow, where inflow waters are recirculated into the outflow. This cross strait flow has been noted north of Ungava Bay, as well as at mid-strait, near Big Island, and extends throughout the water column (Drinkwater, 1988; LeBlond et al., 1981).

Pathways of Hudson Strait inflow in the HBC are still relatively unknown. Jones and Anderson (1994) describe the pathway of Hudson Strait Bottom Water. It forms by deep Labrador Sea water mixing with other waters in Baffin Bay and Labrador Sea. Along its transit in Hudson Strait, these bottom waters mix with the upper layers in the water column. Once the inflow reaches Hudson Bay, the Hudson Strait Bottom Water forms Hudson Bay Intermediate Water by mixing with Hudson Bay Winter Surface Water. Additionally, current reversals at mid-depth in northeastern Hudson Strait have been noted in St-Laurent et al. (2012), possibly suggesting waters from Hudson Strait can enter the bay between Mansel Island and Quebec as well. From the schematic in Jones and Anderson (1994), Hudson Strait waters do not enter Foxe Basin. However, modelling studies have shown otherwise. Defossez et al. (2012) state that while surface waters from Hudson Strait do not flow into Foxe Basin, a warmer intermediate layer suggests that waters from Hudson Bay or Hudson Strait may enter Foxe Basin at mid-depth, between 100-200 m. Meanwhile, a recent modelling study by Florindo-López et al. (2020) show that Arctic waters from the Baffin Island Current enter Hudson Strait and flow into southern Foxe Basin as well as enter Hudson Bay, west of Mansel Island.

Presently one of the missing elements in understanding processes in Hudson Strait and the HBC is knowing the seasonality of Hudson Strait inflow. From the inflowing waters, one could discern what waters are flowing into Hudson Strait, and their pathways, which would

also help in determining circulation in the region, as observations are limited.

In this study, we present the first year-round observations of the Hudson Strait inflow. We discuss its variability and structure throughout the year, as well as determine its source waters. Hudson Strait inflow pathways within the HBC are also discussed. From four deployed moorings, we show that the inflow has reduced seasonality compared to the outflow. The inflow also shows very little shear in the velocity field, with seasonality occurring at all depths in the flow field. The present work establishes the year-round properties of the inflow with the addition of six months of velocity data. The following section describes the hydrographic surveys. Mooring description and data processing precede an in-depth look at the properties of both the inflow and outflow. Source waters and inflow pathways are presented in Sections 5.5 and 5.6 respectively. We discuss our findings and future work in Section 5.7.

5.2 Hydrographic Section Data

Hydrographic sections were taken during cruises for mooring deployment and recovery on August 26, 2008 and September 25-26, 2009 respectively. The transects are shown in Figure 5.2 along with mooring locations and other geographic features.

Hydrographic sections shown in Figure 5.3 show the main features noted in earlier studies (Drinkwater, 1988; Straneo and Saucier, 2008b):

- a strongly stratified surface
- lowest salinities along the southern coast
- cold temperatures (below -1°C and associated with salinities of 33) at mid-depth along the southern coast
- warm, saline waters at depth

Differences, however, do exist between the two sections. The largest stratification in the August 2008 section is found at the surface, in the center of the strait, while in the September 2009 section, maximum stratification is found on the 1026 kg/m^3 isopycnal, separating the surface waters from the cold mid-depth layer. Similarly, the lowest salinity waters in the

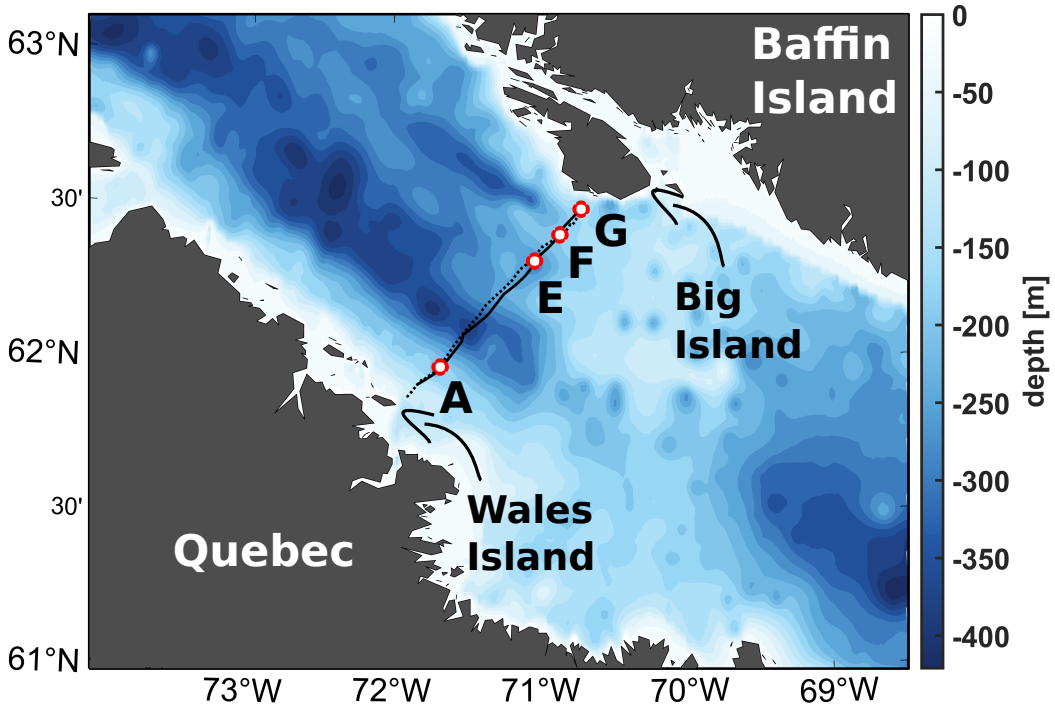

Figure 5.2: Mooring and hydrographic data location. The 2008 and 2009 ship transect is shown in solid and dashed lines respectively, while four mooring locations are indicated with red and white circles and their associated name.

August 2008 section are off shore at the surface. Meanwhile, the lowest salinities in September 2009 remain along the southern coast, extending to nearly 100 m, and have better agreement with earlier studies. The cold mid-depth layer is present in both sections, but extends across the whole strait in the September 2009 section. Finally, near the bottom of the strait, warmer, more saline waters are present compared to the September 2009 section, where bottom waters are cooler and less saline.

Geostrophic velocities for each hydrographic section were obtained by way of the geostrophic streamfunction and referenced to spline interpolated along strait mooring velocities (Figure 5.4; see appendix for more details). The geostrophic velocities show a strong outflow along the southern coast (blue). The largest outflow velocities are located closest to the coast, and decrease northwards. The width of the outflow is about 45 km in both sections. The inflow structure is broad with weaker velocities throughout the water column (red). In the August 2008 section, weak inflow velocities are located at the surface, with a flow reversal at the surface 20 km away from the northern coast. Below 150 m depth weak velocities are

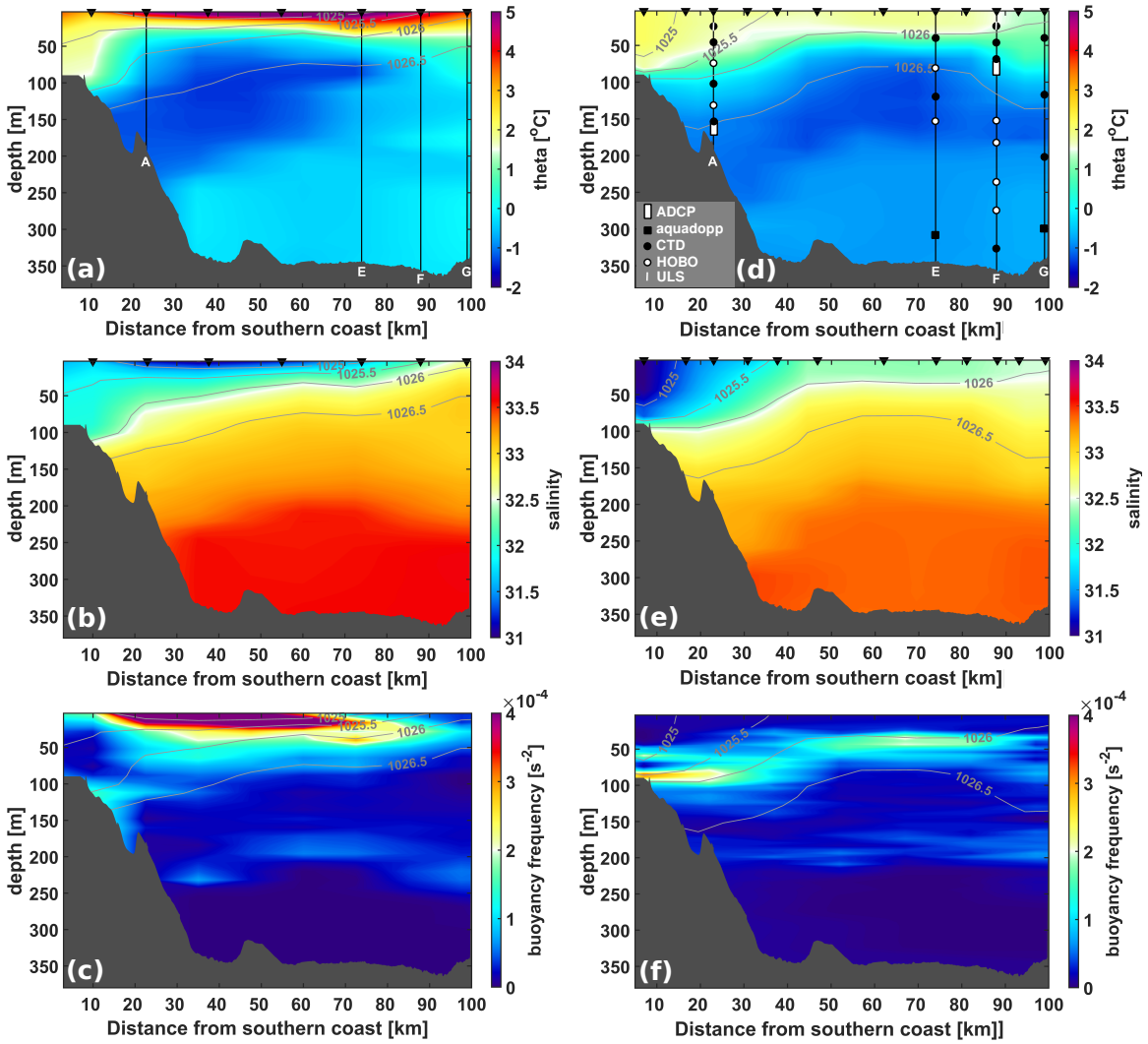

Figure 5.3: Potential temperature (a,d), salinity (b,e), and buoyancy frequency (c,f) for the August 2008 hydrographic section taken upon mooring deployment (left) and the September 2009 hydrographic section (right) taken upon mooring recovery.

present. Comparatively, the 2009 September section shows larger inflow velocities throughout the section, with a maximum below the surface, 20 km from the northern coast.

Transports for the August 2008 section are weaker overall compared to the September 2009 section (Table 5.1), due to the faster velocities in the September section. Transports derived from these synoptic sections are larger than the mean, year-round transports estimated by Straneo and Saucier (2008b) as these sections are snap shots and do not include year-round data. Net heat and salt transports are similar in both sections. The inflow provides more salt than is removed by the fresh outflow, thus the salt budget is net positive into the HBC (as it

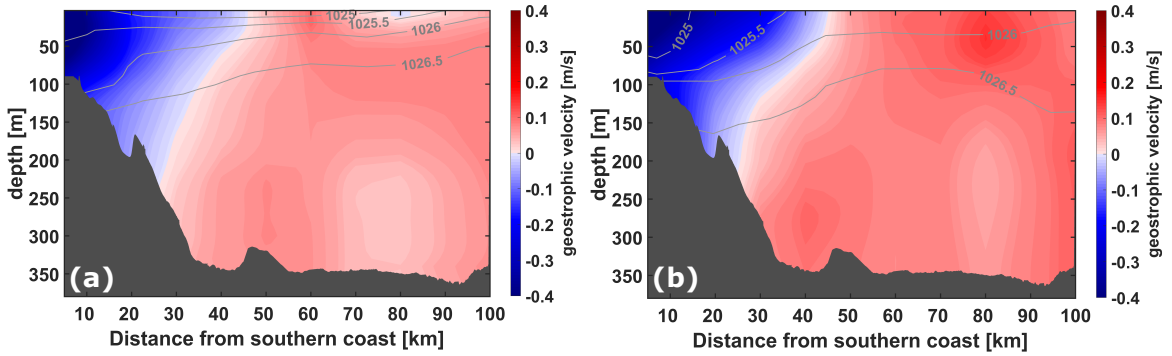

Figure 5.4: Calculated geostrophic velocities for (a) the 2008 hydrographic section, and (b) the 2009 hydrographic section. Both sections are referenced at 100 m to available mooring velocities and use a zero volume transport assumption.

is a salt budget, no reference salinity is used). Overall, a net export of freshwater occurs in Hudson Strait, with the relative contributions of the inflow and outflow depending heavily on the chosen reference salinity. Heat, on the other hand, appears to vary with the properties in the inflow and the position and extent of the cold mid-depth layer. Therefore, we also calculated the transport weighted temperature (TWT) for both the inflow and outflow. In 2008, the TWT for the inflow was -0.06°C, while the outflow was 0.97°C. Comparatively, in 2009 the outflow had a TWT of 0.21°C, while the inflow was -0.54°C. Both the inflow and outflow remove heat from the HBC, however, the main contributor to heat loss in August 2008 was the outflow, while in September 2009, it was the inflow.

The September 2009 section shows the fastest outflowing velocities are associated with the warmest and freshest waters (Figure 5.5) and outflow velocities decrease with decreasing temperatures and increasing salinities. This relation is not as clear in the August 2008 section, as the warmest and freshest waters were located off shore and not along the southern coast. Inflowing waters do not have such a clear relation between water properties and speed, though generally in September 2009, faster velocities are warmer. The cold mid-depth waters are found both in the inflow and outflow, while the warm, saline deep waters are only found in the inflow.

Table 5.1: Volume, freshwater, salt, and heat transports for two hydrographic sections. Freshwater is referenced to a salinity of 33 (34.8) while heat transports are referenced to a temperature of 0°C. Negative values indicate a flux out of the HBC.

	August 2008	**September 2009**
Net Volume	0 Sv	0 Sv
inflow	2.0 Sv	2.9 Sv
outflow	2.0 Sv	2.9 Sv
Net Freshwater	-55 (-52) mSv	-68 (-64) mSv
inflow	-14 (90) mSv	-11 (138) mSv
outflow	-41 (-142) mSv	-57 (-202) mSv
Net Salt	2 kt/s	2.3 kt/s
inflow	68 kt/s	97.6 kt/s
outflow	-66 kt/s	-95.3 kt/s
Net Heat	-8.7 TW	-9.1 TW
inflow	-0.5 TW	-6.5 TW
outflow	-8.2 TW	-2.6 TW

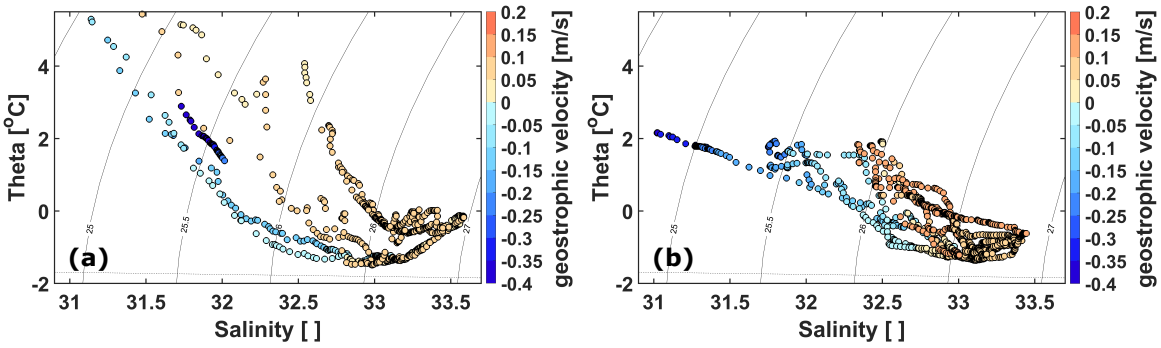

Figure 5.5: Temperature-Salinity plot with associated geostrophic velocities for (a) the 2008 hydrographic section and (b) the 2009 hydrographic section.

5.3 Mooring Data

Four moorings were deployed across Hudson Strait between Big Island and Wales Island from August 2008 to September 2009 to map the seasonal variability in properties and transports across the strait (Figure 5.2). One was deployed on the slope of the southern coast, to capture the center of the outflow, 23 km from Wales Island, while three moorings were deployed on

the northern side of the strait, located 32, 19, and 7 km from Big Island. We assume the flow between Big Island and Baffin Island, as well as between Wales Island and Quebec, is negligible, as the passages are shallow and narrow. Moorings are along the same transect that was used in Straneo and Saucier (2008a) and Sutherland et al. (2011).

5.3.1 Instrumentation

Instrumentation on the four moorings is summarized in Table 5.2. Mooring A, on the southern coast, was deployed on the slope (Figure 5.3d), and was equipped with six instruments sampling temperature and salinity properties, as well as an upward looking Acoustic Doppler Current Profiler (ADCP). The MicroCAT at 25 m was mounted below a 5.8 m aluminum tube meant to sustain hits by icebergs or ice ridges. Blow down of this tube by the current was pronounced but still this set up allowed for more data to be acquired at these shallow depths.

Mooring E was positioned to capture the outer edge of the inflow on the northern side of the strait. The mooring was equipped with a current meter and a 190 kHz Nortek ADCP (at 190 m), but the instrument failed on September 21, 2008.

To capture the center of the inflow, Mooring F had a MicroCAT mounted to the bottom of an aluminum pole at 25 m as on Mooring A. Two ADCPs, one at 80 m and another at 320 m (150 kHz) were located on the mooring. Instrument failure with the deep ADCP meant no recoverable data, and the battery of the ADCP at 80 m was depleted by March 4, 2009.

The northern most mooring, Mooring G (depth 345 m), was set up similarly to Mooring E. A 190 kHz Nortek ADCP was located at 190 m, however the data was unusable (bad data).

5.3.2 Calibration and post-processing

All instruments were calibrated prior to deployment. Standard processing protocols of cross-calibration with instruments above or below, de-spiking and removal of pressure drifts were applied to each instrument.

The magnetic declination was applied to the velocity data from the 11^{th} generation International Geomagnetic Reference Field (IGRF) model, released in December 2009 (Finlay et al., 2010).

Table 5.2: Instrumentation on Moorings A, E, F, and G in Hudson Strait. Instruments that failed early on in deployment were not included. Sampling intervals for each instrument are shown in parentheses. The MicroCATS used were all Seabird SBE MicroCATS, while TidbiTs were all HOBO UTBI-001 TidbiTs. The two ADCPs used were RDI ADCPs. Time periods of data obtained from current meters and ADCPs are shown in the footnotes in day/month/year format.

	A	**E**	**F**	**G**
Latitude [°N]	61.9792	62.3237	62.4087	62.4913
Longitude [°W]	-71.6570	-70.9999	-70.8217	-70.6710
Bottom depth [m]	186	345	357	345
T,S sampling				
MicroCATS (15 min)	25, 45, 100, 160 m	40, 120 m	25, 45, 80, 320 m	40, 120 m
TidbiTs (15 min)	75, 135 m	80, 150 m	150, 180, 230, 270 m	
RBR CTD (15 min)		190 m		200 m
U,V sampling				
ADCP (1 hour)				
Long Ranger 75 kHz	160 m[a]			
Workhorse 300 kHz			80 m[b]	
current meter (20 min)				
Nortek Aquadopp		300 m[c]		300 m[d]
Ice sampling (ULS)	45 m		45 m	

[a] 26/08/2008–24/09/2009 [b] 27/08/2008–04/03/2009 [c] 26/08/2008–24/09/2009 [d] 25/08/2008–24/09/2009

Temperature and salinity data were binned every 6 hours, and linearly interpolated in the vertical. Mooring velocities included in our analysis were from two ADCPs (Moorings A and F) and two Aquadopps (Moorings E and G). Velocities were rotated 33.4° to obtain along and cross strait velocities. This was determined by principal component analysis (88% and 11% explained) when all velocities were combined together. Velocities were then detided with the Matlab t-tide package (Pawlowicz et al., 2002). Velocities were binned in 6 hour increments.

5.3.3 Additional sea ice concentration data

We also use daily 6.25 km resolution AMSR-E sea ice concentration data (Spreen et al., 2008) with our mooring data. We used the location of the moorings to determine the grid point that each mooring was located in.

5.3.4 Additional temperature and salinity data

We supplemented our data with temperature and salinity data both east and west of Hudson Strait from the World Ocean Database (WOD; Boyer et al., 2018) and the Oceanography and Scientific Data–Marine Environmental Data Service (OSD–MEDS; `http://www.meds-sdmm.dfo-mpo.gc.ca/`). Data from the Baffin Island Current was limited to August and September 2008 and 2009, at depths shallower than 400 m, consistent with the time period of the measurements described here. Data located inside the HBC was limited to the years 2000–2010 (August–October), as there was not enough data to limit to 2008 and 2009.

5.4 Overview of Hudson Strait inflow and outflow

5.4.1 Temperature and Salinity

The first year long description of data along the southern side of Hudson Strait was done by Straneo and Saucier (2008a,b), who noted, as we see in our data here, seasonal heating and cooling of the surface. They saw that warming begins in mid-July, and lasts until mid-November. Cold mid-depth waters were also noted by Straneo and Saucier (2008a,b) and Drinkwater (1988). Delayed warming at depth occurs in the fall, with near freezing temperatures throughout the winter and into spring (Straneo and Saucier, 2008a,b). Our data

shows these features noted earlier, while also showing some variability in timing and delayed warming at depth in the spring.

The southern side of Hudson Strait is characterized by the fresh outflow from Hudson and James Bay river input (Drinkwater, 1988; Straneo and Saucier, 2008a). The water column generally has salinities below 33 (lower panel, Figure 5.6), however, near the bottom, salinities can exceed this value, agreeing with Drinkwater (1988) and Sutherland et al. (2011). The first pulse of freshwater passing over the mooring array roughly occurs at the same time as Straneo and Saucier (2008a), with some variability in timing. Our data also shows a secondary, weaker, and more broad freshwater pulse passing over the mooring a few months later, with its peak in March. This second pulse does not appear in the data described by Straneo and Saucier (2008a), as we have more data available at shallower depths (25 m) compared to their mooring set up (shallowest data at 55 m). The pulse is not clearly discernible at the 100 m MicroCAT in our data, implying that it is an event contained at the surface.

High frequency low salinity pulses, described in detail by Sutherland et al. (2011), are seen in green in the first half of our time series. However, in the Sutherland et al. (2011) dataset, sharp increases in salinity separate each low salinity event. Our dataset, on the other hand, especially during the months of December to March, where our low salinity signal is drawn out, makes identifying individual events more difficult.

One interesting feature to note is the timing of the cold, low salinity waters and arrival of sea ice. During this time, the flow on the southern side of the strait is quite strong (Figure 5.10 here; Straneo and Saucier, 2008a; Sutherland et al., 2011), and would thus be exporting ice to the Labrador Sea. The timing indicates that the sea ice is not completely locally grown, and at least some part of it is being transported from upstream.

From the data shown in Figure 5.6, the mean temperature of the outflow is -0.85°C, falling within the two estimates for Mooring A in Straneo and Saucier (2008a). The mean salinity for the outflow we found to be 32.5, which is higher than the value in Straneo and Saucier (2008a).

In contrast to the outflow, panels in Figure 5.7 show a different regime on the northern side of Hudson Strait. Both Moorings G and E did not have salinity measurements at the bottom of the water column. Thus for Mooring E, we used the maximum salinity recorded

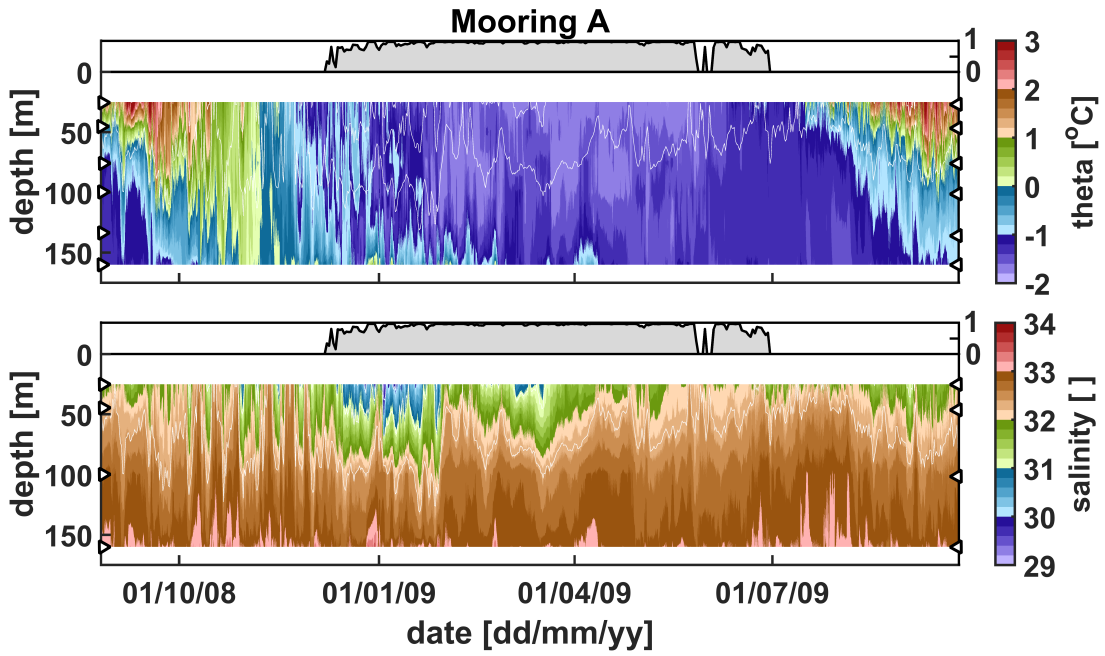

Figure 5.6: Mooring A temperature (top) and salinity (bottom) for the mooring deployment period. Locations where discrete measurements were taken are shown by the black and white triangles. Linear interpolation was used at depths where instruments were not present. White lines denote potential density. Sea ice concentration (in grey) from daily AMSR-E data is also shown for the mooring deployment period with its axis on the right hand side.

in our dataset to linearly extrapolate in the vertical to 305 m. Similarly, at Mooring G we used the maximum salinity recorded in the mooring time series to linearly extrapolate to the bottom level of the salinity profile.

All three inflow moorings show seasonal heating at the surface during the summer months, and cold temperatures that extend from the surface to at least 200 m depth in winter. Cold mid-depth waters on the northern side of the strait fall between 0 – -1°C, and are only present at the beginning of the time series.

Differences between the moorings are also present. Summer heating at the surface is shallower at Mooring E compared to F and G, while cold winter temperatures below -1°C do not penetrate as deep at Mooring F when compared to Moorings E and G.

One major difference when comparing salinity in the inflow to the outflow is the higher salinity values and the reduced seasonal variability in the inflow, which is due to the absence of the seasonal freshwater export from the HBC. The 33 isohaline for all three moorings extends higher up in the water column in early fall and spring (oscillating around 100 m depth), and

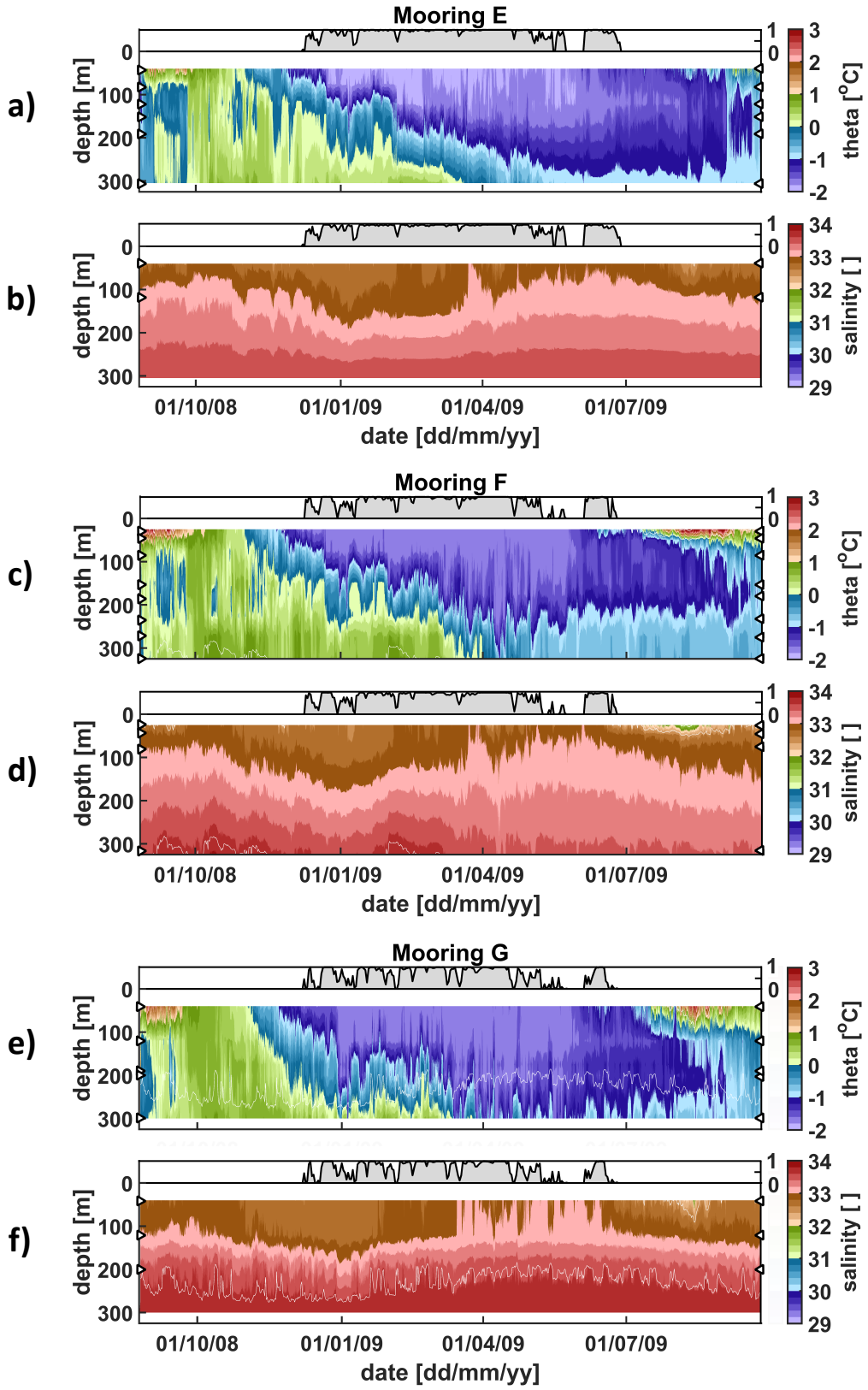

Figure 5.7: Temperature and salinity data for the mooring deployment period for Moorings E (a, b), F (c, d), and G (e, f). Temperature panels are a, c, and e, while salinity panels are b, d, and f. Locations where discrete measurements were taken are shown by the black and white triangles. White lines denote potential density. Sea ice concentration from daily AMSR-E data is also shown for the mooring deployment period with its axis on the right hand side.

is most pronounced at Moorings F and E. At Mooring G, from April–June, the 33 isohaline extends to 50 m depth, which does not occur in the two other moorings. Waters fresher than 32 transit at Moorings F and G in the summer of 2009.

The mean (x-z average) temperature for the inflow from Mooring F, as it is the only inflow mooring with measurements taken throughout the water column, is -0.51°C, with an average salinity of 33.1.

Based on the hydrographic data as well as the mooring data, we can separate the waters in Hudson Strait into three groups, which we have indicated in Figure 5.8, and are as follows:

- surface waters subject to seasonal heating and riverine input (Figure 5.8, dotted line)
- cold waters at mid-depth around salinities of 33 (Figure 5.8, dashed line)
- warmer, saline waters at the bottom (Figure 5.8, solid line)

Figure 5.8 also highlights the differences between the two flows. Inflowing waters tend to be both more saline and dense than their outflowing counterparts. For instance, Figure 5.8 shows that, on average, outflowing waters do not reach salinities greater than 33. Another observation is the migration of data points to the freezing line in winter, while in summer and early fall waters are warm, and not at the freezing point.

Cold mid-depth waters during summer (June–October) are likely from the previous winter and gives Hudson Strait data a 'hockey stick' shape during these months (Figure 5.8). However, the source of these waters remains unknown. A cold core remains along the southern side of the strait, specifically in summer. Due to the depth of winter cooling in Hudson Strait, these cold mid-depth waters are only a summer phenomena.

5.4.2 Velocities in Hudson Strait

5.4.2.1 Tides

Tides in Hudson Strait are some of the largest in the world, with its semidiurnal tide ranging from 3 to over 10 m in the strait (Arbic et al., 2007; O'Reilly et al., 2005), while the associated tidal currents can reach up to 1 m/s. During the mooring deployment cruise, the tidal range near Big Island was 12 m, while across the strait, near Wales Island, the tidal range was 10

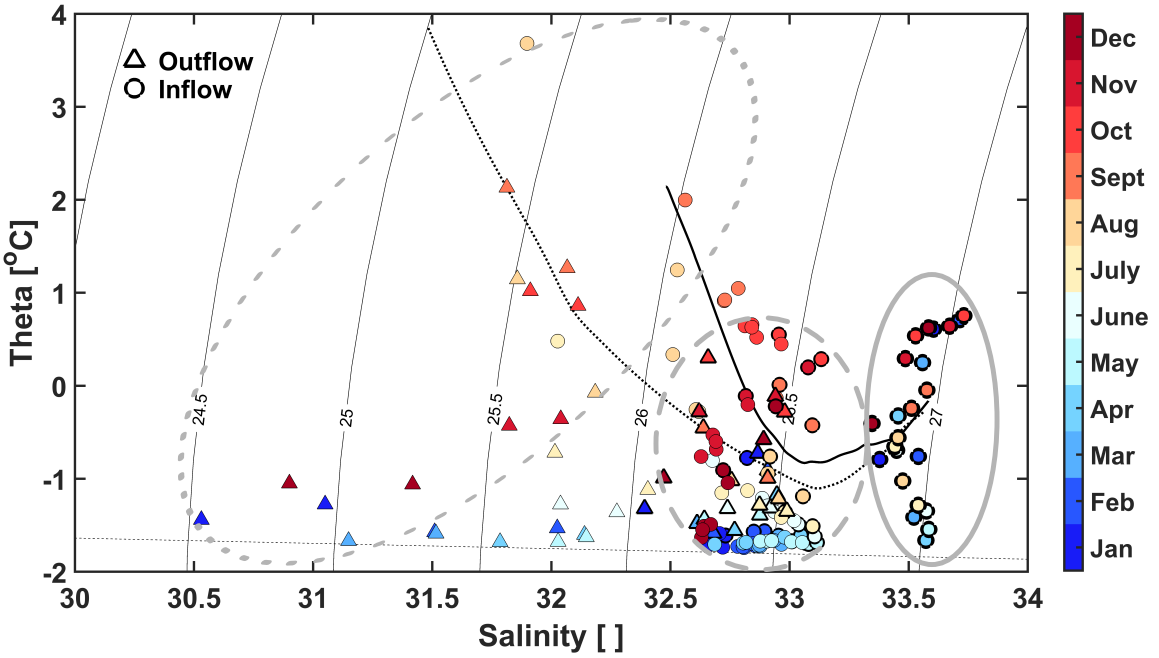

Figure 5.8: Monthly averaged temperature and salinity properties for each instrument in the mooring array. Circles show data from Moorings E, F, and G, while triangles show data from Mooring A. The outline of each shape specifies a depth range, where thin outlines show waters 0-99 m, medium outlines show waters from 100-199 m, and thick outlines show waters 200 m to the bottom. The dotted and solid black lines show a smoothed mean outflow and inflow profile respectively from the 2008 and 2009 CTD data. Finally, grey ellipses indicate the three different types of water observed in the strait (see text for details).

m. The largest tidal component in Hudson Strait is the M2 tide, followed by S2. The M2 constituent accounted for 28–40% of the tidal current signal in our dataset, followed by the S2 constituent, ranging from 8–13%. Tidal ellipses for the M2 tide from the mooring data are shown in Figure 5.9. The orientation of the ellipses indicate that the tide is mainly barotropic, with a small baroclinic influence. The tidal signal at the two deepest locations on Moorings E and G possibly indicate an effect of local bathymetry. Velocity descriptions below use only de-tided data.

5.4.2.2 Velocities in the inflow and outflow

The flow field on the southern side of the strait (Figure 5.10) is directed along strait as noted by both Drinkwater (1988) and Straneo and Saucier (2008a). Our data shows almost no directional shear with depth, similar to Drinkwater (1988) and Straneo and Saucier (2008a). Like Straneo and Saucier (2008a), we also see along strait velocities decrease linearly with

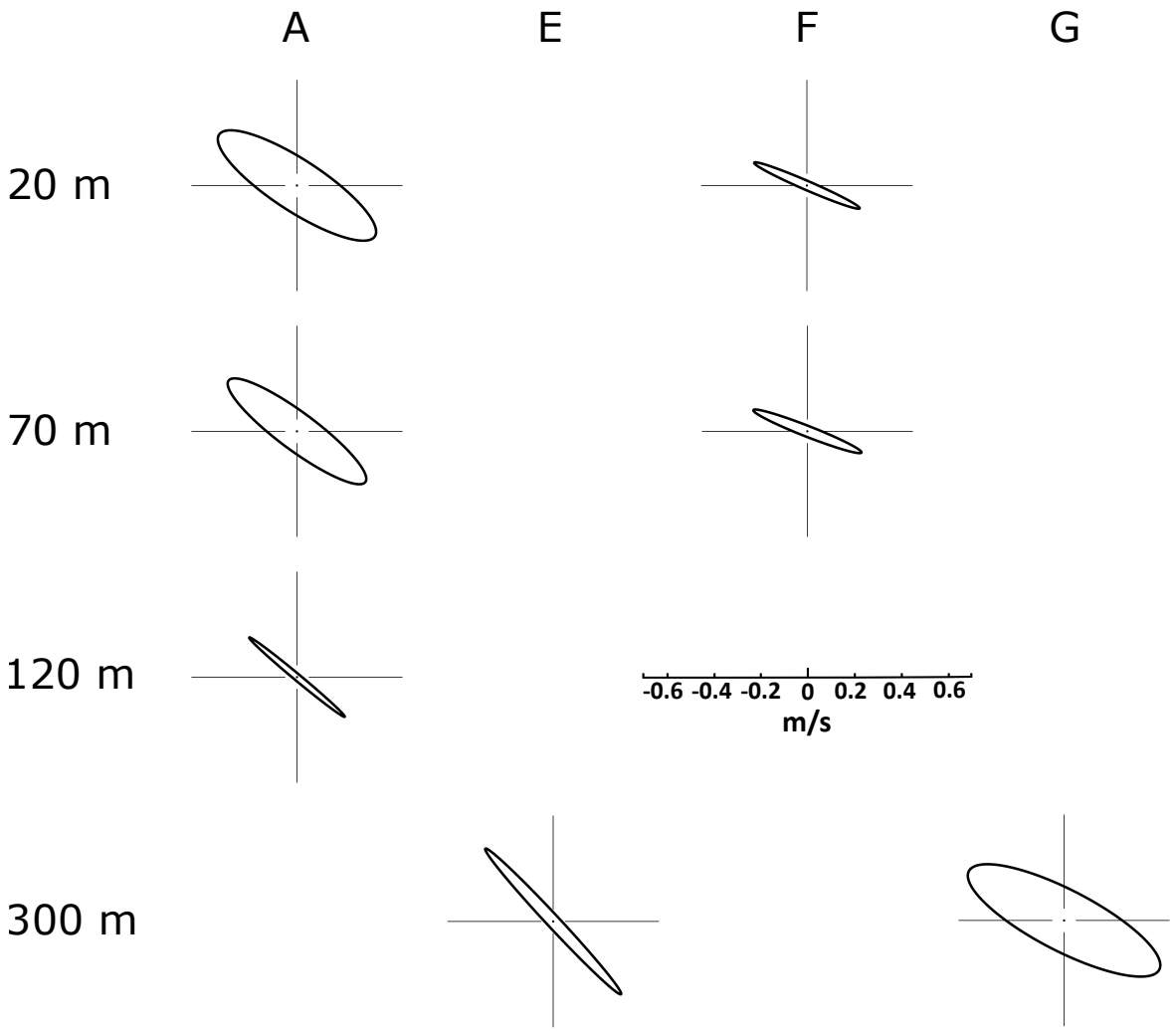

Figure 5.9: Tidal ellipses of the M2 tide for the moorings at four depths. Black lines for each ellipse are drawn from ± 0.05-0.45 m/s.

depth, however only to around 100 m. We see that seasonality in the outflow along strait velocities occurs at the surface, with little seasonality at depth. Our data shows December and January having the fastest surface velocities, and thus the largest shear in the flow, which coincides with the lowest salinity surface waters at this time. This timing is slightly later than Straneo and Saucier (2008a), who found the fastest velocities in the outflow to occur in November, coinciding with the lowest salinity in their dataset, and the weakest velocities between March and June. In our dataset, November is the month with the weakest surface velocities and weakest shear in the vertical. The difference in timing between the two studies is likely explained by variability in the timing of the freshwater coming from Hudson Bay.

On the northern side of the strait, data is more limited due to instrument failure of the deep ADCP, and battery failure of the shallow ADCP on Mooring F, only providing us with six months of data. Thus our description of the flow field focuses on the six months of available data we have, covering 7–67 m depth. Velocities along the northern side of the strait are weaker throughout the water column to 67 m depth compared to the outflow. Our data agrees with Drinkwater (1988) in that vertical shear is also smaller, however, vertical velocity shear in his data is still larger, as our data shows negligible amounts of shear in the vertical. We also find that inflow velocities are not directed along strait, and do contain some component of cross strait flow which differs from the eastern Hudson Strait section occupied by Drinkwater (1988). The largest velocities occur in September, with the weakest flow in February. The seasonality of the inflow along strait velocities does not coincide with that of the outflow.

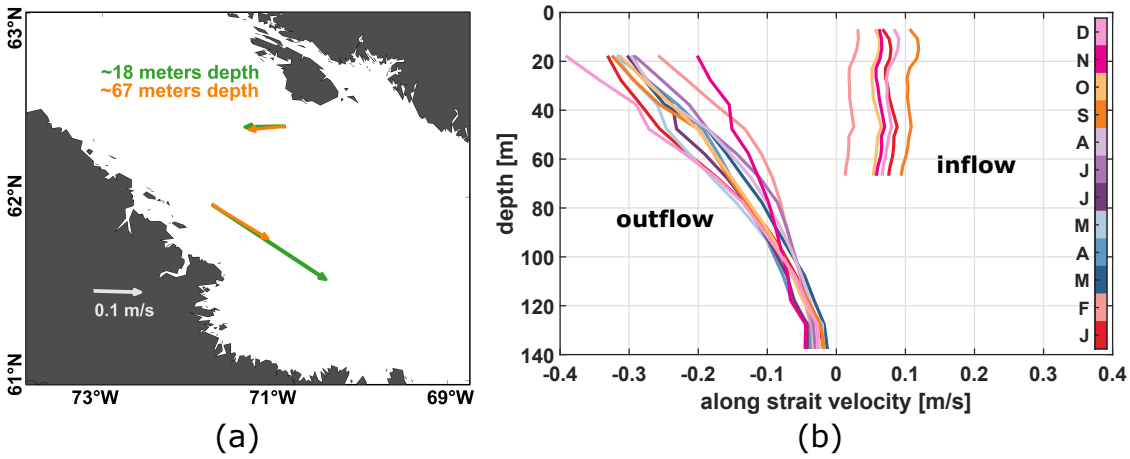

Figure 5.10: (a) Averaged velocities from August 27, 2008 to March 4, 2009 at roughly 18 and 67 m depth (green and orange respectively) for Moorings A and F. (b) Monthly mean along strait velocity profiles for the outflow (Mooring A ADCP) and for the inflow (Mooring F ADCP).

5.5 Hudson Strait inflow source waters

Speculation over what water masses contribute to the Hudson Strait inflow has occurred over the last four decades. We know that the Baffin Island Current (BIC) separates into two branches, with only the western branch entering Hudson Strait (LeBlond et al., 1981). It was

thought that the inflow might contain intermediate Labrador Sea Water or West Greenland Water, even though intermediate Labrador Sea Water has never been observed in the strait (Drinkwater, 1986, 1988). Bailey and Hachey (1950) suggest that deeper waters in Hudson Strait are sourced from the BIC with some contribution from West Greenland Water. More recent work suggests that it is the Davis Strait outflow that contributes most to the Hudson Strait inflow, while stating that warmer waters from West Greenland entering Hudson Strait is unlikely (Straneo and Saucier, 2008a).

Focusing only on August and September data, the majority of Hudson Strait inflow does fall within the Arctic Water (AW) definition (Figure 5.11). The densest waters may have a small contribution from either Transitional Water (TrW) or the West Greenland Irminger Water (WGIW) as described in Curry et al. (2011). We also note that the Hudson Strait inflow waters at mid-depth (salinities around 33) are generally warmer than their BIC AW counterpart. Hudson Strait is an area of intense tidal mixing and could possibly explain this increase in temperature.

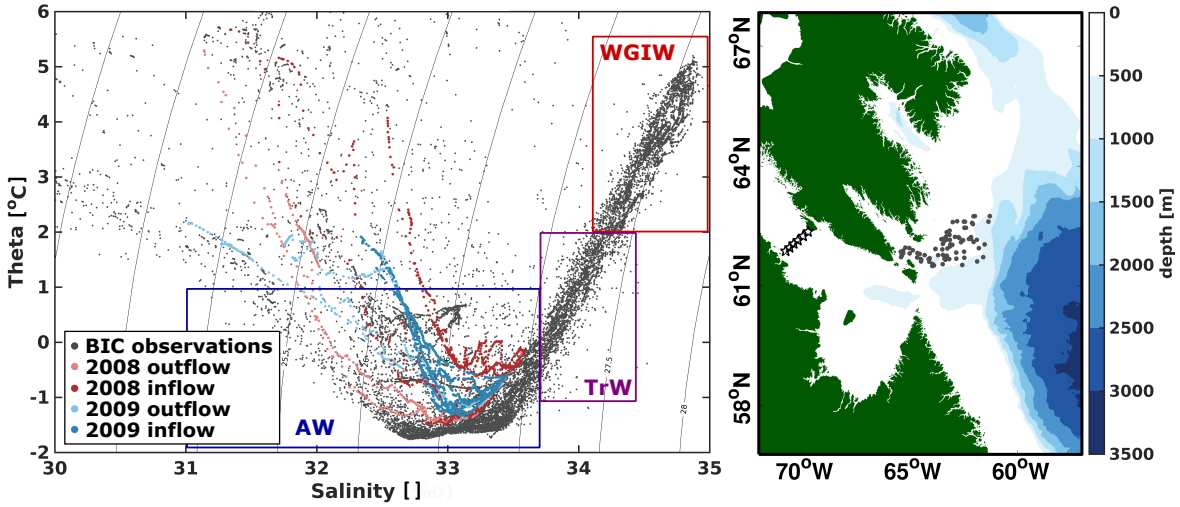

Figure 5.11: Baffin Island Current (BIC) observations (grey) from August–September 2008 and 2009 ($\leq$ 400 m) with Hudson Strait hydrographic data presented earlier. Pink colours show data from August 2008 with light points indicating outflow and dark points indicating inflow. Similarly, blue points show data from September 2009. Boxes defining Arctic Water (AW; blue), Transitional Water (TrW; purple), and West Greenland Irminger Water (WGIW; red) are based on definitions defined in Curry et al. (2011). The map shows locations of the BIC observations with grey points, while the stars indicate the hydrographic section in Hudson Strait.

5.6 Hudson Strait inflow pathways within the HBC

One of the other open questions with regards to Hudson Strait inflow is its pathways within the HBC. Once the inflow enters Hudson Strait, part of it is recirculated to the outflow via the cross strait flow. The remainder however, flows deeper into Hudson Strait. One study determined that inflow did not flow into Foxe Basin, only Hudson Bay, with Hudson Strait bottom water mixing with Hudson Bay winter surface water to form Hudson Bay intermediate water (Jones and Anderson, 1994). It was this resulting water mass that entered Foxe Basin. Conversely, a modelling study noted warmer waters entering Foxe Basin at depth, but could not confirm if this warm water came from Hudson Bay or Hudson Strait (Defossez et al., 2012). They also note that waters from Hudson Strait do not enter Foxe Basin at the surface.

We compare the summer hydrographic data from Hudson Strait to available profiles in western Hudson Strait, Foxe Basin, and northern Hudson Bay (Figure 5.12) so as to shed some light on the pathways of the Hudson Strait inflow. As data is sparse in this region, our analysis may provide additional speculation as to the fate of Hudson Strait inflow waters in the HBC.

Inflowing waters seem to remain along the northern coast, with no evidence of being recirculated to the southern side of the strait in western Hudson Strait (Figure 5.12, top panel). The properties in northwestern Hudson Strait are similar to the properties captured at the hydrographic sections in the middle of the strait, indicating little to no water mass modification or mixing. Farther west, near Southampton Island, advected Hudson Strait waters that have undergone some mixing and modification, appear to form the deep waters in this location. This region is the intersection of Foxe Basin, Hudson Bay, and Hudson Strait, and has the potential for complicated flow dynamics.

It is possible modified inflow waters enter Foxe Basin at mid-depth, as there is some overlap in the TS properties. The presence of AW in Foxe Basin from Fury and Hecla Strait makes determining inflow pathways more challenging. We agree with earlier studies (Campbell, 1959; Prinsenberg, 1986b) that modified inflowing waters at mid-depth might be present around Foxe Peninsula (Figure 5.12, middle panel), however, surface and deep waters that are formed in Foxe Basin could contain Hudson Strait waters that have been transformed.

Deep waters in Foxe Basin likely remain at depth in Foxe Channel until they overflow the sill (at 180 m) east of Southampton Island (Defossez et al., 2010). We also see the potential for Hudson Strait inflow to enter Foxe Basin near Southampton Island as indicated by Florindo-López et al. (2020, Figure 5). However, without velocity data, it is difficult to confirm where the waters are coming from.

The other pathway Hudson Strait inflow can take is flowing into Hudson Bay (Figure 5.12, bottom panel). Eastern Hudson Bay shows cold, fresh waters along the coast, stemming from river discharge. It is possible that deep waters in northeast Hudson Bay might also have a signal from Hudson Strait (or Foxe Basin) as there have been current reversals in this region before (Granskog et al., 2011; Prinsenberg, 1986a; St-Laurent et al., 2012). Northwestern Hudson Bay, however, does show evidence of Hudson Strait inflow. These profiles have been modified due to mixing at the intersection of Foxe Basin, Hudson Bay, and Hudson Strait, with mixing decreasing with depth. The characteristic 'hockey stick' shape of the inflow waters is still intact and has experienced only a slight shift to lower salinities. This route is likely the main pathway for Hudson Strait inflow waters.

This result differs from earlier studies as exchange between Hudson Bay and Foxe Basin was thought to occur between Mansel and Southampton Islands with no contribution from Hudson Strait (Drinkwater, 1986; Prinsenberg, 1986a). Additionally, data presented in Prinsenberg (1986c) and Jones and Anderson (1994) do not show the warmer waters at depth from Hudson Strait that we see in our data. Differences are likely due to different seasonal conditions or long term changes in the circulation.

5.7 Summary

The HBC is a relatively isolated region, with the only connections to the global ocean being FHS to the north and Hudson Strait to the east. As the flow through FHS is small, Hudson Strait is the main gateway exchanging waters between the HBC and the global ocean. Hudson Strait exports riverine laden water to the Labrador Sea along its southern coast, while importing more saline waters along its northern coast to the HBC. In this study we presented the first year-round measurements of the Hudson Strait inflow. This dataset is comprised

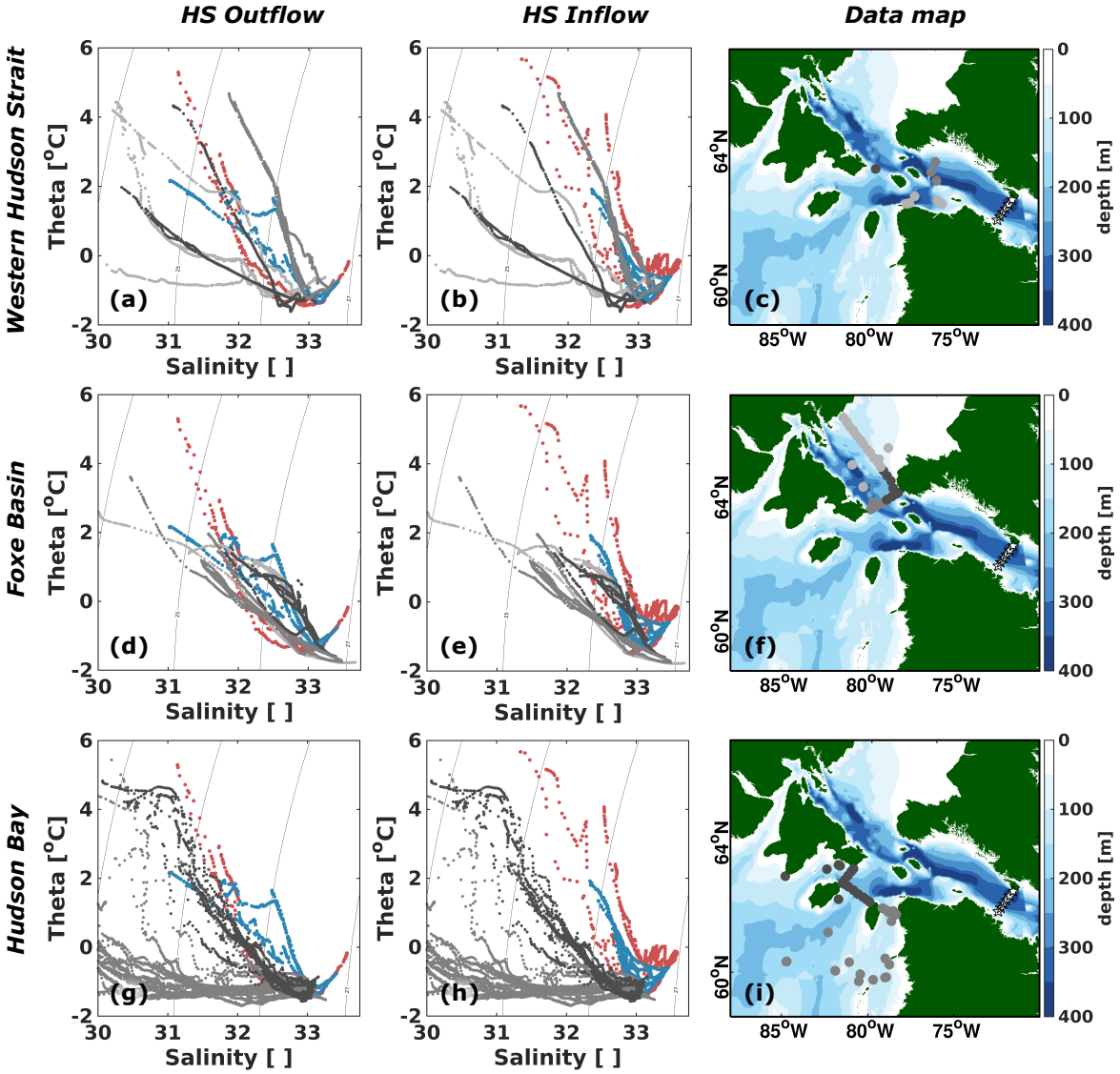

Figure 5.12: Three regions showing potential pathways of Hudson Strait inflow water; Western Hudson Strait (top panels), Foxe Basin (middle panels), and Hudson Bay (bottom panels). Columns show the comparison of Hudson Strait outflow (left) and inflow (center) data with additional data (grey points). Data locations are shown in the corresponding maps (right column). Grey shading indicates different subregions. Pink points show Hudson Strait hydrographic data taken at mid-strait (indicated by stars in the maps), from August 2008, while blue points show data from September 2009.

of 4 moorings across the strait, one on the southern side, and three on the northern side. These data were accompanied by hydrographic data from mooring deployment and recovery cruises in August 2008 and September 2009. Unfortunately instrument failure on the northern moorings limited our ability to estimate transport in the inflow. Nonetheless, we provide a detailed look at the properties of the inflow as well as consider source waters and pathways of the Hudson Strait inflow.

Our hydrographic sections show similar features to previous studies, with fresh waters along the southern coast and more saline waters along the northern coast (Drinkwater, 1988; Straneo and Saucier, 2008a). Cold waters are present at mid-depth, with a cold core along the southern side of the strait. This cold core, which is easily seen in our August 2008 section, as well as Straneo and Saucier (2008a) and Drinkwater (1988), has been classified as Arctic Water (Dunbar, 1951), indicating that the source could either be from Foxe Basin or Hudson Bay, having thought to have been produced during the previous winter (Drinkwater, 1986; Dunbar, 1951). Again, as also seen in previous studies (Drinkwater, 1988; Straneo and Saucier, 2008a), bottom waters in Hudson Strait show a temperature and salinity increase compared to the cold mid-depth waters.

The outflow is comprised primarily of riverine water from Hudson and James Bays. The bulk of which flows through the mooring array in December and January, corresponding to the fastest surface velocities in the outflow as well as the arrival of sea ice. What is more clear in our dataset than earlier work, is the secondary pulse of freshwater in March, due to a second increase in river discharge in Hudson and James Bays in October due to the increased storm and precipitation activity (Déry et al., 2018). Additionally, our dataset also supports the findings in Sutherland et al. (2011), as our data also shows high frequency pulses in salinity in the first half of our time series. These pulses are the result of freshwater, anticyclonic eddies passing over the mooring (Sutherland et al., 2011).

In contrast, the inflow, which does not have a fresh boundary current feeding it, shows reduced variability throughout the year in both salinity and velocities. Salinity ranges between 31.3 – 33.8 throughout the year, with a density range of 1024.8 – 1027.1 kg/m^3. Temperature seasonality is similar across the strait due to ice cover for the majority of the year, but has a range of -1.8 – 5.5°C. We can separate the inflow waters into surface waters, cold mid-depth

waters, and warmer, saline waters at the bottom. Inflow waters at all depths undergo seasonal temperature changes, from -1.8–1.0°C at depth (200 m to bottom) to -1.8–4.7°C at the surface. With regards to salinity, the mid-depth and bottom waters, undergo little change throughout the year, from 32.6–33.8, while surface waters undergo larger seasonal changes (31.3–33.1).

We determined the inflow waters are mainly Arctic Waters, stemming from the Baffin Island Current. We speculate that there might also be small contributions of both Transitional Water and West Greenland Irminger Water. The inflow waters transit along the northern side of the strait, with the majority of the inflow entering northern Hudson Bay, with some modification, to become deep waters in the bay. We suspect that some mid-depth Hudson Strait water may also enter Foxe Basin.

Inflow velocity seasonality does not appear to be impacted by or related to seasonality in the outflow (with the available six months of data shown). There also appears to be no apparent influence on the inflow from the anticyclonic eddies on the southern side of the strait, as was queried by Sutherland et al. (2011). The cross strait flow is still present at mid-strait, recirculating some water to the outflow.

As discussed in Straneo and Saucier (2008a), they estimated that a significant portion of the Davis Strait outflow is recirculated in Hudson Strait and Hudson Bay, before exiting in the Hudson Strait outflow. As the Hudson Strait inflow falls within the classification of Arctic Water, and would contain a large amount of the freshwater exiting Davis Strait, any anomalous freshwater events passing through Davis Strait could be rerouted in Hudson Strait, and delay part of the signal. Unfortunately due to instrumentation failure, we were not able to provide inflow volume measurements with this dataset.

Future work involves the use of a high resolution numerical ocean model. Not only evaluate the model with these new observations, but perhaps to fill in some gaps in the observations. Continued observational efforts, however, are still needed in the strait, as without a long time series of observations we cannot confirm if the HBC is undergoing Atlantification as originally suggested by Bailey and Hachey (1950). If this was occurring, the resulting changes in the local ecosystem would have a direct impact on the communities in this region.

Acknowledgments

Firstly, the authors would like to thank the captains and crews of the RV Knorr (cruise numbers 194-01 and 196-01). Support from NSERC (RGPIN 04357, awarded to PGM) to fund a research stay for NAR at Scripps Institute of Oceanography made this work possible. We appreciate the use of the AMSR-E sea ice concentration data as well as the additional temperature and salinity data from the World Ocean Database and the Oceanography and Scientific Data-Marine Environmental Data Service.

Appendix 5.A: Calculating geostrophic velocities

Geostrophic velocities for each hydrographic section (Figure 5.4) were calculated using the Gibbs SeaWater Oceanographic Toolbox of TEOS-10. Gridded conservative temperature, absolute salinity, and absolute pressure data are used to calculate the geostrophic streamfunction, which involves the difference in velocity between the pressure, P, and the reference pressure. The geostrophic velocities were then calculated using the geostrophic streamfunction relative to the surface pressure.

Calculated geostrophic velocities were referenced to spline interpolated averaged August-September mooring velocities at 100 m. To obtain the reference velocities at 100 m for Mooring A, we linearly interpolated the average August-September velocity profile for each year. On the northern side of the strait, surface velocities at Mooring F are only available until March 2009. We used the mean August-September velocities for each year at Moorings E and G to linearly interpolate a deep velocity value at Mooring F. The average August-September 2008 velocity profile at Mooring F was then linearly interpolated in the vertical to obtain a reference velocity value at 100 m for both 2008 and 2009. We assume that velocities at the surface are horizontally homogeneous, using the average 2008 August-September Mooring F velocity profile in the top 70 m for both Moorings E and G, we linearly interpolated to the mean August-September velocities at these moorings for each year to obtain reference velocities at 100 m for each mooring.

The resulting four reference velocities for each year, were spline interpolated horizontally across the strait. Calculated geostrophic velocities were referenced at 100 m, and then adjusted for net zero volume transport, so as to constrain the outflow.

Bibliography

Aagaard, K. and Carmack, E. C. (1989). The role of sea ice and other fresh water in the Arctic circulation. *Journal of Geophysical Research: Oceans*, 94(C10):14485–14498.

Arbic, B. K., St-Laurent, P., Sutherland, G., and Garrett, C. (2007). On the resonance and influence of the tides in Ungava Bay and Hudson Strait. *Geophysical Research Letters*, 34(17).

Babb, D., Andrews, J., Dawson, J., Landry, D., Mussells, O., and Weber, M. (2019). Transportation and community use of the marine enviroment. In Kuzyk, Z. and L.M. Candlish, L. E., editors, *From Science to Policy in the Greater Hudson Bay Marine Region: An Integrated Regional Impact Study (IRIS) of Climate Change and Modernization*, pages 341–377.

Bailey, W. and Hachey, H. (1950). An increasing Atlantic influence in Hudson Bay. *Proceedings of the Nova Scotia Institute of Science*, 22(4):17–33.

Bamber, J., van den Broeke, M., Ettema, J., Lenaerts, J., and Rignot, E. (2012). Recent large increases in freshwater fluxes from Greenland into the North Atlantic. *Geophysical Research Letters*, 39(19).

Bamber, J. L., Tedstone, A. J., King, M. D., Howat, I. M., Enderlin, E. M., van den Broeke, M. R., and Noel, B. (2018). Land Ice Freshwater Budget of the Arctic and North Atlantic Oceans: 1. data, methods, and results. *Journal of Geophysical Research: Oceans*, 123(3):1827–1837.

Barber, F. G. (1965). Current Observations in Fury and Hecla Strait. *Journal of the Fisheries Research Board of Canada*, 22(1):225–229.

Beszczynska-Möller, A., von Appen, W.-J., and Fahrbach, E. (2015). Physical oceanography and current meter data from moorings F1-F14 and F15/F16 in the Fram Strait, 1997-2012.

Boyer, T., Baranova, O. K., Coleman, C., Garcia, H. E., Grodsky, A., Locarnini, R. A., Mishonov, A. V., O'Brien, T., Paver, C., Reagan, J., Seidov, D., Smolyar, I. V., Weathers, K., , and Zweng, M. M. (in prep.). World ocean database 2018. Technical report, NOAA.

Campbell, N. (1959). Some Oceanographic Features of Northern Hudson Bay, Foxe Channel, and Hudson Strait. Technical Report 46, Fisheries Research Board of Canada.

Castro de la Guardia, L., PG, M., AE, D., NJ, L., and AD, T. v. S. (2017). Sea ice cycle in western Hudson Bay, Canada, from a polar bear perspective. *Marine Ecology Progress Series*, 564:225–233. 10.3354/meps11964.

Cuny, J., Rhines, P. B., and Kwok, R. (2005). Davis Strait volume, freshwater and heat fluxes. *Deep Sea Research Part I: Oceanographic Research Papers*, 52(3):519 – 542.

Curry, B., Lee, C. M., and Petrie, B. (2011). Volume, Freshwater, and Heat Fluxes through Davis Strait, 2004–05. *Journal of Physical Oceanography*, 41(3):429–436.

Curry, B., Lee, C. M., Petrie, B., Moritz, R. E., and Kwok, R. (2014). Multiyear Volume, Liquid Freshwater, and Sea Ice Transports through Davis Strait, 2004–10. *Journal of Physical Oceanography*, 44(4):1244–1266.

Defossez, M., Saucier, F., Myers, P., Caya, D., and Dumais, J. (2012). Comparing Winter and Summer Simulated Estuarine Circulations in Foxe Basin, Canada. *Atmosphere-Ocean*, 50(3):386–401.

Defossez, M., Saucier, F., Myers, P., Caya, D., and Dumais, J.-F. (2010). Analysis of a dense water pulse following mid-winter opening of polynyas in western Foxe Basin, Canada. *Dynamics of Atmospheres and Oceans*, 49:54–74.

Déry, S. J., Stadnyk, T. A., MacDonald, M. K., Koenig, K. A., and Guay, C. (2018). Flow alteration impacts on Hudson Bay river discharge. *Hydrological Processes*, 32(24):3576–3587.

Déry, S. J., Stieglitz, M., and McKenna, E. C. (2005). Characteristics and Trends of River Discharge into Hudson, James, and Ungava Bays, 1964–2000. *Journal of Climate*, 18(14):2540–2557.

Drinkwater, K. (1986). Chapter 13 Physical Oceanography of Hudson Strait and Ungava Bay. *Elsevier Oceanography Series*, 44(Canadian Inland Seas):237–264.

Drinkwater, K. F. (1988). On the Mean and Tidal Currents in Hudson Strait. *Atmosphere–Ocean (Canadian Meteorological and Oceanographic Society)*, 26(2):252 – 266.

Dunbar, M. (1951). Eastern Arctic Waters. Technical Report 88, Fisheries Research Board of Canada.

Easton, A. K. (1972). Tides of Hudson Strait. Technical Report BI-R-72-6, Bedford Institute of Oceanography.

Finlay, C. C., Maus, S., Beggan, C. D., Hamoudi, M., Lowes, F. J., Olsen, N., and Thébault, E. (2010). Evaluation of candidate geomagnetic field models for IGRF-11. *Earth, Planets and Space*, 62(8):787–804.

Florindo-López, C., Bacon, S., Aksenov, Y., Chafik, L., Colbourne, E., and Holliday, N. P. (2020). Arctic Ocean and Hudson Bay Freshwater Exports: New Estimates from 7 Decades of Hydrographic Surveys on the Labrador Shelf. *Journal of Climate*.

Gelderloos, R., Straneo, F., and Katsman, C. A. (2012). Mechanisms behind the Temporary Shutdown of Deep Convection in the Labrador Sea: Lessons from the Great Salinity Anomaly Years 1968–71. *Journal of Climate*, 25(19):6743–6755.

Granskog, M. A., Kuzyk, Z. Z. A., Azetsu-Scott, K., and Macdonald, R. W. (2011). Distributions of runoff, sea-ice melt and brine using δ18O and salinity data – A new view on freshwater cycling in Hudson Bay. *Journal of Marine Systems*, 88(The Hudson Bay System):362–374.

Haine, T. W., Curry, B., Gerdes, R., Hansen, E., Karcher, M., Lee, C., Rudels, B., Spreen, G., de Steur, L., Stewart, K. D., and Woodgate, R. (2015). Arctic freshwater export: Status, mechanisms, and prospects. *Global and Planetary Change*, 125:13 – 35.

Jahn, A. and Holland, M. M. (2013). Implications of Arctic sea ice changes for North Atlantic deep convection and the meridional overturning circulation in CCSM4-CMIP5 simulations. *Geophysical Research Letters*, 40(6):1206–1211.

Jones, E. P. and Anderson, L. G. (1994). Northern Hudson Bay and Foxe Basin: Water masses, circulation and productivity. *Atmosphere-Ocean*, 32(2):361–374.

Kuhlbrodt, T., Griesel, A., Montoya, M., Levermann, A., Hofmann, M., and Rahmstorf, S. (2007). On the driving processes of the Atlantic meridional overturning circulation. *Reviews of Geophysics*, 45(2).

LeBlond, P. H., Osborn, T., Hodgins, D., Goodman, R., and Metge, M. (1981). Surface circulation in the Western Labrador Sea. *Deep Sea Research Part A. Oceanographic Research Papers*, 28(7):683 – 693.

McKinley, G. A., Fay, A. R., Lovenduski, N. S., and Pilcher, D. J. (2017). Natural variability and anthropogenic trends in the ocean carbon sink. *Annual Review of Marine Science*, 9(1):125–150.

Myers, R. A., Akenhead, S. A., and Drinkwater, K. (1990). The influence of Hudson Bay runoff and ice–melt on the salinity of the inner Newfoundland Shelf. *Atmosphere-Ocean*, 28(2):241–256.

O'Reilly, C. T., Solvason, R., and Solomon, C. (2005). Where are the world's largest tides? In Ryan, J., editor, *BIO Annual Report "2004 in Review"*, pages 44–46.

Pawlowicz, R., Beardsley, B., and Lentz, S. (2002). Classical tidal harmonic analysis including error estimates in MATLAB using T_TIDE. *Computers & Geosciences*, 28(8):929 – 937.

Prinsenberg, S. (1986a). Chapter 10 The Circulation Pattern and Current Structure of Hudson Bay. *Elsevier Oceanography Series*, 44:187 – 204.

Prinsenberg, S. (1986b). Chapter 12 On the Physical Oceanography of Foxe Basin. *Elsevier Oceanography Series*, 44(Canadian Inland Seas):217–236.

Prinsenberg, S. (1986c). Chapter 9 Salinity and Temperature Distributions of Hudson Bay and James Bay. *Elsevier Oceanography Series*, 44:163 – 186.

Rabe, B., Dodd, P. A., Hansen, E., Falck, E., Schauer, U., Mackensen, A., Beszczynska-Möller, A., Kattner, G., Rohling, E. J., and Cox, K. (2013). Liquid export of Arctic freshwater components through the Fram Strait 1998–2011. *Ocean Science*, 9(1):91–109.

Ridenour, N. A., Hu, X., Jafarikhasragh, S., Landy, J. C., Lukovich, J. V., Stadnyk, T. A., Sydor, K., Myers, P. G., and Barber, D. G. (2019). Sensitivity of freshwater dynamics to ocean model resolution and river discharge forcing in the Hudson Bay Complex. *Journal of Marine Systems*, 196:48 – 64.

Sadler, H. E. (1982). Water flow into Foxe Basin through Fury and Hecla Strait. *Naturaliste Canadien*, pages 701 – 707.

Saucier, F. J., Senneville, S., Prinsenberg, S., Roy, F., Smith, G., Gachon, P., Caya, D., and Laprise, R. (2004). Modelling the sea ice-ocean seasonal cycle in Hudson Bay, Foxe Basin and Hudson Strait, Canada. *Climate Dynamics*, 23(3/4):303–326.

Schauer, U., Beszczynska-Möller, A., Walczowski, W., Fahrbach, E., Piechura, J., and Hansen, E. (2008). *Variation of Measured Heat Flow Through the Fram Strait Between 1997 and 2006*, chapter 3, pages 65–85. Springer Netherlands, Dordrecht.

Spreen, G., Kaleschke, L., and Heygster, G. (2008). Sea ice remote sensing using AMSR-E 89-GHz channels. *Journal of Geophysical Research: Oceans*, 113(C2). C02S03.

St-Laurent, P., Straneo, F., and Barber, D. G. (2012). A conceptual model of an Arctic sea. *Journal of Geophysical Research: Oceans*, 117(C6). C06010.

Stocker, T., Qin, D., Plattner, G.-K., Tignor, M., Allen, S., Boschung, J., Nauels, A., Xia, Y., Bex, V., and (eds.), P. M. (2013). Ipcc, 2013: Climate Change 2013: The Physical Science Basis. Contribution of Working Group I to the Fifth Assessment Report of the Intergovernmental Panel on Climate Change. Technical report, Cambridge University Press, Cambridge, United Kingdom and New York, NY, USA.

Straneo, F. and Saucier, F. (2008a). The outflow from Hudson Strait and its contribution to the Labrador Current. *Deep Sea Research Part I: Oceanographic Research Papers*, 55(8):926 – 946.

Straneo, F. and Saucier, F. J. (2008b). *The Arctic–Subarctic Exchange Through Hudson Strait*, chapter 10, pages 249–261. Springer Netherlands, Dordrecht.

Sutcliffe Jr., W. H., Loucks, R. H., Drinkwater, K. F., and Coote, A. R. (1983). Nutrient Flux onto the Labrador Shelf from Hudson Strait and its Biological Consequences. *Canadian Journal of Fisheries and Aquatic Sciences*, 40(10):1692–1701.

Sutherland, D. A., Straneo, F., Lentz, S. J., and Saint-Laurent, P. (2011). Observations of fresh, anticyclonic eddies in the Hudson Strait outflow. *Journal of Marine Systems*, 88(The Hudson Bay System):375–384.

Yang, Q., Dixon, T. H., Myers, P. G., Bonin, J., Chambers, D., van den Broeke, M. R., Ribergaard, M. H., and Mortensen, J. (2016). Recent increases in Arctic freshwater flux affects Labrador Sea convection and Atlantic overturning circulation. *Nature Communications*, 7(1).

Chapter 6

Conclusion

The Hudson Bay Complex (HBC) is a unique region, nearly isolated from open ocean circulation. It experiences a full cryogenic cycle, and also receives a significant amount of continental runoff. The full sea ice cover is beneficial to the locals in the region who depend on sea ice for their livelihoods. However, it limits the shipping season, which brings supplies to these remote regions, to the ice free times of year. The other industry interested in the region is the hydroelectric industry, exploiting the large number of rivers for power generation. One of the big unknowns is the impact this industry has on the bay. Unfortunately, due to its challenging environment, collecting data is difficult, and mostly occurs in the summer and fall. This means that there are still many unanswered questions about oceanic processes in this region. Using models to answer these questions, specifically questions involving impact or sensitivity, has the benefit of not being limited in space or in time.

However, using numerical models do come with their own set of simplifications, and while practical, are potential sources of error. These simplifications include the six model assumptions outlined in Chapter 2, parametrizations of small scale processes, and truncation errors from the numerical schemes used. Other sources of error can come from the atmosphere or runoff forcing used for the model simulations. For instance, discharge forcing from the HYPE hydrological model has the largest uncertainties in Foxe Basin, where there are no observational measurements, while in the prairie catchment regions, features such as prairie pot-holes are difficult to simulate (Stadnyk et al., 2020). Additionally, other simplifications when using discharge forcing include prescribing the river waters to have the same temperature as

the surrounding seawater, and only mixing river discharge in the top 10 m when it enters the ocean. Finally, because forcing datasets use observations or reanalysis to constrain the output, natural climate variability would also have some signal in the forcing data. However, while these limitations in the forcing and model output may impact small scale oceanographic features, processes on larger space and time scales would be correct.

6.1 Main Findings

6.1.1 Sensitivity of freshwater dynamics to ocean model resolution and river discharge forcing in the Hudson Bay Complex

The primary goal of Chapter 3 was to evaluate the sensitivity of the HBC to changes in river discharge for the BaySys project. I used a regional ocean model with three different river discharge datasets and two model resolutions to evaluate the sensitivity to freshwater changes for present day conditions. Firstly, I showed that the model was appropriate for simulating the HBC by comparing a range of variables to the available observations. Sea surface temperatures in winter were simulated well, while summer temperatures were cooler than observations. Salinity was also simulated well by the model. Ice thickness and concentration were underestimated in the fall, however, the freshwater contained in sea ice was captured by all model simulations.

The second component of Chapter 3 was to calculate a multi-year freshwater budget, as only freshwater budgets for individual years had been published. I presented both annual and seasonal multi-year freshwater budgets for the HBC and its subregions. In the HBC as a whole, Hudson Bay, and Foxe Basin, freshwater contained in sea ice was the dominant term throughout the year. Whereas in Hudson Strait and James Bay, river discharge and advection played larger roles in the freshwater budget.

The final component of this chapter was to investigate how river discharge impacted the ocean. Due to the limited number of river discharge datasets, sensitivity studies to these datasets have not been done. Generally, increased river discharge lead to increased exchange between regions while also leading to stronger circulation patterns in Hudson Bay. Overall, I found that changes in river discharge impacted the annual mean cyclonic circulation pattern

in the bay.

First and foremost, the results in this chapter indicate that the BaySys project can move to the next phase, which involves running future scenarios in the HBC. From this chapter, I have provided a present day freshwater budget and evaluated how this budget is impacted by river discharge. This allows for a base on which future studies can be built, not only in the HBC, but the Arctic as well. Additionally, this study identified the role of river discharge in the bay, and its impact on ocean dynamics in the region. The wide spread differences in ocean dynamics showed the impact that seemingly small changes in river discharge can have.

6.1.2 Revisiting the Circulation of Hudson Bay: Evidence for a Seasonal Pattern

From Chapter 3, I showed that the barotropic streamfunction was not as stable as previously thought. With the different river discharge datasets, I saw differences in the main processes exchanging water between the interior and boundary region. The mean component of the flow (which also includes Ekman transport) was transporting waters to the interior in the summer months. This observation was unexpected, and lead to the research question for Chapter 4, "is there a seasonal circulation pattern in Hudson Bay?"

Using a high resolution model, in combination with Absolute Dynamic Topography observations from satellite, I found that in summer, geostrophic currents, generated by halosteric height gradients, were not cyclonic as was expected. These currents were anticyclonic in eastern Hudson Bay, with flow directed through the center of the bay. Meanwhile, western Hudson Bay still showed cyclonic flow, with small cyclonic and anticyclonic features. This new result explains previous observations of current reversals in moored data (Granskog et al., 2011; St-Laurent et al., 2012), as well as provide more context to an earlier study linking Churchill sea surface height with river discharge in James Bay (Gough et al., 2005).

This seasonal circulation pattern has changed the way we think about Hudson Bay, and that it is more complex than originally thought. This work will be used by observationalists working in the bay, for placing instruments to capture this flow reversal. Hopefully, in situ measurements will give us a better idea of its timing, frequency, and strength.

6.1.3 Hudson Strait Inflow: Structure and Variability

Chapter 5, while also focused on the HBC, used observational data instead of an ocean model. Year long data for the southern side of Hudson Strait has been presented by Straneo and Saucier (2008a) and Sutherland et al. (2011), who investigated the seasonal cycle as well as the high frequency variability in the outflow. In Chapter 5, I presented the first year-round observations for the Hudson Strait inflow on the northern side of the strait. It is also the first time that year long measurements on both sides of the strait have been taken at the same time.

From the hydrographic data, the data agreed with previous studies, which showed on the southern coast the presence of a highly stratified, fresh outflow, while on the northern side, a weakly stratified, more saline inflow. Our calculated geostrophic velocities show a net freshwater outflow of 55-68 mSv (S_{ref}=33) and net heat loss of around 9 TW.

The mooring data showed more seasonality along the southern coast compared to the northern coast, specifically with regards to salinity, as the seasonality in the outflow is driven by the riverine waters that feed it. Summer time warming transitions to near freezing temperatures in winter across the strait. Regarding velocity, instrument failure on the northern moorings prevented an estimate of volume transport for the Hudson Strait inflow. Nonetheless, the available inflow data shows very little shear, but seasonality occurs throughout the water column, while the outflow shows seasonal changes at the surface, with strong shear throughout the year. Using additional data both up and down stream, the source waters to the inflow stem from Arctic Water in the Baffin Island Current, with deeper waters potentially having some contribution from Transitional or West Greenland Irminger Water. Inflow waters flow into Hudson Bay, and possibly into Foxe Basin.

Year long inflow data has been a missing piece of the Hudson Strait puzzle for over a decade. As the Hudson Strait inflow is the largest source of oceanic water to the HBC, we now know the properties of waters entering the region before they are transformed. This will help in identifying water mass transformation processes before the waters are exported in the Hudson Strait outflow. This data also shows that the inflow and outflow have different driving mechanisms with regards to their variability. Even though there are still missing pieces, such

as transport in the inflow, this work has increased our understanding of the strait, while also providing a base on which future studies can compare and build upon.

6.2 The Big Picture

The work in this thesis focused on ocean dynamics in the HBC. Results from Chapter 3 show that changes in river discharge, from hydroelectric development, climate change, or a mix of both, will have an impact on processes in the bay. If hydroelectric production is to increase as a form of renewable energy in the future, we should know the impact the industry has on the HBC.

The seasonal circulation changes presented in Chapter 4 gives us a better idea of what the currents are doing, as well as where the riverine waters are going within the bay. This will help in tracking nutrients or pollutants, as the bay provides sustenance to the locals in this region, and in the case of pollutants, adverse effects could be severe.

Finally, in Chapter 5, I presented the first year-round measurements of the Hudson Strait inflow. Understanding the properties of waters entering Hudson Strait, as well as where these waters are sourced from, allows us to see the connection between Hudson Strait and the global ocean. Not only that, this data will help to identify the role of Hudson Strait in potentially damping freshwater events from the Arctic.

In summary, the HBC continues to be a region with many unknowns. The work in this thesis answered some of the questions, some decades old. The oceanic system is highly influenced by the river discharge draining into it, of which the local population and industry depend for survival. Additionally, the role of the HBC in the climate system is still not clear, however, speculation suggests that its role could be underestimated, with the key being Hudson Strait.

Bibliography

Gough, W. A., Robinson, C., and Hosseinian, R. (2005). The Influence of James Bay River Discharge on Churchill, Manitoba Sea Level. *Polar Geography*, 29(3):213–223.

Granskog, M. A., Kuzyk, Z. Z. A., Azetsu-Scott, K., and Macdonald, R. W. (2011). Distributions of runoff, sea-ice melt and brine using δ18O and salinity data – A new view on freshwater cycling in Hudson Bay. *Journal of Marine Systems*, 88(The Hudson Bay System):362–374.

St-Laurent, P., Straneo, F., and Barber, D. G. (2012). A conceptual model of an Arctic sea. *Journal of Geophysical Research: Oceans*, 117(C6). C06010.

Stadnyk, T., MacDonald, M., Tefs, A., Déry, S., Koenig, K., Gustafsson, D., Isberg, K., and Arheimer, B. (2020). Hydrological modeling of freshwater discharge into Hudson Bay using HYPE. *Elementa Science of the Anthropocene*, 8(1).

Straneo, F. and Saucier, F. (2008). The outflow from Hudson Strait and its contribution to the Labrador Current. *Deep Sea Research Part I: Oceanographic Research Papers*, 55(8):926 – 946.

Sutherland, D. A., Straneo, F., Lentz, S. J., and Saint-Laurent, P. (2011). Observations of fresh, anticyclonic eddies in the Hudson Strait outflow. *Journal of Marine Systems*, 88(The Hudson Bay System):375–384.

Bibliography

Aagaard, K. and Carmack, E. C. (1989). The role of sea ice and other fresh water in the Arctic circulation. *Journal of Geophysical Research: Oceans*, 94(C10):14485–14498.

Andersson, J. C. M., Pechlivanidis, I. G., Gustafsson, D., Donnelly, C., and Arheimer, B. (2013). Key factors for improving large-scale hydrological model performance. In Lekkas, T., editor, *Proceedings of the 13th International Conference on Environmental Science and Technology*, Proceedings of the International Conference on Environmental Science and Technology, pages 77–88, Univ, Aegean, 30, Voulgaroktonou Str, Athens, GR 114 72, Greece. Univ Aegean; Global Network Environm Sci & Technol, Global Nest, Secritariat. 13th International Conference on Environmental Science and Technology (CEST), Athens, Greece, Sep 05-07, 2013.

Asselin, R. (1972). Frequency Filter for Time Integrations. *Monthly Weather Review*, 100(6):487–490.

Babb, D., Andrews, J., Dawson, J., Landry, D., Mussells, O., and Weber, M. (2019). Transportation and community use of the marine environment. In Kuzyk, Z. and L.M. Candlish, L. E., editors, *From Science to Policy in the Greater Hudson Bay Marine Region: An Integrated Regional Impact Study (IRIS) of Climate Change and Modernization*, pages 341–377.

Bamber, J., van den Broeke, M., Ettema, J., Lenaerts, J., and Rignot, E. (2012). Recent large increases in freshwater fluxes from Greenland into the North Atlantic. *Geophysical Research Letters*, 39(19).

Barber, F. G. (1965). Current Observations in Fury and Hecla Strait. *Journal of the Fisheries Research Board of Canada*, 22(1):225–229.

Bernard, B., Madec, G., Penduff, T., Molines, J.-M., Treguier, A.-M., Le Sommer, J., Beckmann, A., Biastoch, A., Böning, C., Dengg, J., Derval, C., Durand, E., Gulev, S., Remy, E., Talandier, C., Theetten, S., Maltrud, M., McClean, J., and De Cuevas, B. (2006). Impact of partial steps and momentum advection schemes in a global ocean circulation model at eddy-permitting resolution. *Ocean Dynamics*, 56(5/6):543 – 567.

Blanke, B., Arhan, M., Madec, G., and Roche, S. (1999). Warm Water Paths in the Equatorial Atlantic as Diagnosed with a General Circulation Model. *Journal of Physical Oceanography*, 29(11):2753–2768.

Blanke, B. and Delecluse, P. (1993). Variability of the Tropical Atlantic Ocean Simulated by a General Circulation Model with Two Different Mixed-Layer Physics. *Journal of Physical Oceanography*, 23(7):1363–1388.

Blanke, B. and Raynaud, S. (1997). Kinematics of the Pacific Equatorial Undercurrent: An Eulerian and Lagrangian Approach from GCM Results. *Journal of Physical Oceanography*, 27(6):1038–1053.

Bougeault, P. and Lacarrere, P. (1989). Parameterization of orography-induced turbulence in a mesobeta-scale model. *Monthly Weather Review*, 117(8):1872 – 1890.

Brown, N. J., Nilsson, J., and Pemberton, P. (2019). Arctic Ocean Freshwater Dynamics: Transient Response to Increasing River Runoff and Precipitation. *Journal of Geophysical Research: Oceans*, 124(7):5205–5219.

Castro de la Guardia, L., Derocher, A. E., Myers, P. G., Terwisscha van Scheltinga, A. D., and Lunn, N. J. (2013). Future sea ice conditions in Western Hudson Bay and consequences for polar bears in the 21st century. *Global Change Biology*, 19(9):2675–2687.

Castro de la Guardia, L., PG, M., AE, D., NJ, L., and AD, T. v. S. (2017). Sea ice cycle in western Hudson Bay, Canada, from a polar bear perspective. *Marine Ecology Progress Series*, 564:225–233. 10.3354/meps11964.

Dai, A., Qian, T., Trenberth, K. E., and Milliman, J. D. (2009). Changes in continental freshwater discharge from 1948 to 2004. *Journal of Climate*, 22(10):2773–2792.

Dai, A. and Trenberth, K. E. (2002). Estimates of Freshwater Discharge from Continents: Latitudinal and Seasonal Variations. *Journal of Hydrometeorology*, 3(6):660–687.

de Boisséson, E., Thierry, V., Mercier, H., Caniaux, G., and Desbruyères, D. (2012). Origin, formation and variability of the Subpolar Mode Water located over the Reykjanes Ridge. *Journal of Geophysical Research: Oceans*, 117(C12).

Defossez, M., Saucier, F., Myers, P., Caya, D., and Dumais, J. (2012). Comparing Winter and Summer Simulated Estuarine Circulations in Foxe Basin, Canada. *Atmosphere-Ocean*, 50(3):386–401.

Deremble, B., Hogg, A. M., Berloff, P., and Dewar, W. (2011). On the application of no-slip lateral boundary conditions to 'coarsely' resolved ocean models. *Ocean Modelling*, 39(3/4):411 – 415.

Déry, S. J., Stadnyk, T. A., MacDonald, M. K., Koenig, K. A., and Guay, C. (2018). Flow alteration impacts on Hudson Bay river discharge. *Hydrological Processes*, 32(24):3576–3587.

Déry, S. J., Hernández-Henríquez, M. A., Burford, J. E., and Wood, E. F. (2009). Observational evidence of an intensifying hydrological cycle in northern Canada. *Geophysical Research Letters*, 36(13). L13402.

Déry, S. J., Mlynowski, T. J., Hernández-Henríquez, M. A., and Straneo, F. (2011). Interannual variability and interdecadal trends in Hudson Bay streamflow. *Journal of Marine Systems*, 88(The Hudson Bay System):341–351.

Déry, S. J., Stadnyk, T. A., MacDonald, M. K., and Gauli-Sharma, B. (2016). Recent trends and variability in river discharge across northern Canada. *Hydrology and Earth System Sciences*, 20(12):4801 – 4818.

Déry, S. J., Stieglitz, M., and McKenna, E. C. (2005). Characteristics and Trends of River Discharge into Hudson, James, and Ungava Bays, 1964–2000. *Journal of Climate*, 18(14):2540–2557.

Déry, S. J. and Wood, E. F. (2004). Teleconnection between the Arctic Oscillation and Hudson Bay river discharge. *Geophysical Research Letters*, 31(18). L18205.

Drinkwater, K. F. (1988). On the Mean and Tidal Currents in Hudson Strait. *Atmosphere–Ocean (Canadian Meteorological and Oceanographic Society)*, 26(2):252 – 266.

Dukhovskoy, D. S., Myers, P. G., Platov, G., Timmermans, M.-L., Curry, B., Proshutinsky, A., Bamber, J. L., Chassignet, E., Hu, X., Lee, C. M., and Somavilla, R. (2016). Greenland freshwater pathways in the sub-Arctic seas from model experiments with passive tracers. *Journal of Geophysical Research: Oceans*, 121(1):877–907.

Dunbar, M. (1982). Oceanographic research in Hudson and James bays. *Le Naturaliste Canadien*, 109(4):677 – 683.

Eby, M. and Holloway, G. (1994). Grid transformation for incorporating the Arctic in a global ocean model. *Climate Dynamics*, (4-5):241.

Fichefet, T. and Maqueda, M. A. M. (1997). Sensitivity of a global sea ice model to the treatment of ice thermodynamics and dynamics. *Journal of Geophysical Research: Oceans*, 102(C6):12609–12646.

Florindo-López, C., Bacon, S., Aksenov, Y., Chafik, L., Colbourne, E., and Holliday, N. P. (2020). Arctic Ocean and Hudson Bay Freshwater Exports: New Estimates from 7 Decades of Hydrographic Surveys on the Labrador Shelf. *Journal of Climate*.

Forget, G., Campin, J.-M., Heimbach, P., Hill, C. N., Ponte, R. M., and Wunsch, C. (2015). ECCO version 4: an integrated framework for non-linear inverse modeling and global ocean state estimation. *Geoscientific Model Development*, 8(10):3071–3104.

Fukumori, I., Wang, O., Fenty, I., Forget, G., Heimbach, P., and Ponte, R. M. (2017). ECCO version 4 release 3. Technical report. Available at `ftp://ecco.jpl.nasa.gov/Version4/Release3/doc/v4r3_estimation_synopsis.pdf`.

Gaden, A., Chételat, J., Heath, J., Kuzyk, Z., Stern, G., and Wang, F. (2019). Contaminant cycling, ecosystem pathways, and wildlif trends in a changing climate. In Kuzyk, Z. and L.M. Candlish, L. E., editors, *From Science to Policy in the Greater Hudson Bay Marine Region: An Integrated Regional Impact Study (IRIS) of Climate Change and Modernization*, pages 311–339.

Gagnon, A. S. and Gough, W. A. (2002). Hydro-Climatic trends in the Hudson Bay Region, Canada. *Canadian Water Resources Journal / Revue canadienne des ressources hydriques*, 27(3):245–262.

Gagnon, A. S. and Gough, W. A. (2005). Trends in the Dates of Ice Freeze-up and Breakup over Hudson Bay, Canada. *Arctic*, (4):370.

Gagnon, A. S. and Gough, W. A. (2006). East-west asymmetry in long-term trends of landfast ice thickness in the Hudson Bay region, Canada. *Climate Research*, 32:177–186.

Galbraith, P. S. and Larouche, P. (2011). Reprint of "Sea-surface temperature in Hudson Bay and Hudson Strait in relation to air temperature and ice cover breakup, 1985–2009". *Journal of Marine Systems*, 88(The Hudson Bay System):463–475.

Gaspar, P., Gregoris, Y., and Lefevre, J. (1990). A simple eddy kinetic-energy model for simulations of the oceanic vertical mixing - Tests at station Papa and long-term upper ocean study site. *Journal of Geophysical Research: Oceans*, 95(C9):16179 – 16193.

Gelfan, A., Gustafsson, D., Motovilov, Y., Arheimer, B., Kalugin, A., Krylenko, I., and Lavrenov, A. (2017). Climate change impact on the water regime of two great Arctic rivers: modeling and uncertainty issues. *Climatic Change*, 141(3):499–515.

Gillard, L. C., Hu, X., Myers, P. G., and Bamber, J. L. (2016). Meltwater pathways from marine terminating glaciers of the Greenland ice sheet. *Geophysical Research Letters*, 43(20):10,873–10,882. 2016GL070969.

Gough, W., Cornwell, A., and Tsuji, L. (2004a). Trends in Seasonal Sea Ice Duration in Southwestern Hudson Bay. *Arctic*, 57(3):299–305.

Gough, W. A., Gagnon, A. S., and Lau, H. P. (2004b). Interannual Variability of Hudson Bay Ice Thickness. *Polar Geography*, 28(3):222–238.

Gough, W. A., Robinson, C., and Hosseinian, R. (2005). The Influence of James Bay River Discharge on Churchill, Manitoba Sea Level. *Polar Geography*, 29(3):213–223.

Granskog, M. A., Kuzyk, Z. Z. A., Azetsu-Scott, K., and Macdonald, R. W. (2011). Distributions of runoff, sea-ice melt and brine using δ18O and salinity data – A new view on freshwater cycling in Hudson Bay. *Journal of Marine Systems*, 88(The Hudson Bay System):362–374.

Granskog, M. A., Macdonald, R. W., Kuzyk, Z. Z. A., Senneville, S., Mundy, C.-J., Barber, D. G., Stern, G. A., and Saucier, F. (2009). Coastal conduit in southwestern Hudson Bay (Canada) in summer: Rapid transit of freshwater and significant loss of colored dissolved organic matter. *Journal of Geophysical Research: Oceans*, 114(C8). C08012.

Granskog, M. A., Macdonald, R. W., Mundy, C.-J., and Barber, D. G. (2007). Distribution, characteristics and potential impacts of chromophoric dissolved organic matter (CDOM) in Hudson Strait and Hudson Bay, Canada. *Continental Shelf Research*, 27(15):2032 – 2050.

Griffies, S. M. (2004). *Fundamentals of ocean climate models.* Princeton, N.J. : Princeton University Press.

Hachey, H. B. (1935). Circulation of Hudson Bay water as indicated by drift bottles. *Science*, 82:275 – 276.

Hare, A. A., Stern, G. A., Kuzyk, Z. Z. A., Macdonald, R. W., Johannessen, S. C., and Wang, F. (2010). Natural and Anthropogenic Mercury Distribution in Marine Sediments from Hudson Bay, Canada. *Environmental Science & Technology*, 44(15):5805–5811. PMID: 20617840.

Hare, F. and Montgomery, M. (1949). Ice, Open Water, and Winter Climate in the Eastern Arctic of North America: Part 2. *Arctic*, 2(3):149–164.

Hochheim, K. P. and Barber, D. G. (2010). Atmospheric forcing of sea ice in Hudson Bay during the fall period, 1980–2005. *Journal of Geophysical Research: Oceans*, 115(C5).

Hochheim, K. P. and Barber, D. G. (2014). An Update on the Ice Climatology of the Hudson Bay System. *Arctic, Antarctic, and Alpine Research*, 46(1):66–83.

Holdsworth, A. M. and Myers, P. G. (2015). The Influence of High-Frequency Atmospheric Forcing on the Circulation and Deep Convection of the Labrador Sea. *Journal of Climate*, 28(12):4980–4996.

Holmes, R. M., McClelland, J. W., Peterson, B. J., Tank, S. E., Bulygina, E., Eglinton, T. I., Gordeev, V. V., Gurtovaya, T. Y., Raymond, P. A., Repeta, D. J., Staples, R., Striegl, R. G., Zhulidov, A. V., and Zimov, S. A. (2012). Seasonal and Annual Fluxes of Nutrients and Organic Matter from Large Rivers to the Arctic Ocean and Surrounding Seas. *Estuaries and Coasts*, 35(2):369–382.

Hu, X. and Myers, P. G. (2013). A Lagrangian view of Pacific water inflow pathways in the Arctic Ocean during model spin-up. *Ocean Modelling*, 71:66 – 80.

Hu, X., Sun, J., Chan, T. O., and Myers, P. G. (2018). Thermodynamic and dynamic ice thickness contributions in the Canadian Arctic Archipelago in NEMO-LIM2 numerical simulations. *The Cryosphere*, 12(4):1233–1247.

Hunke, E. C. (2001). Viscous–plastic sea ice dynamics with the EVP model: Linearization issues. *Journal of Computational Physics*, 170(1):18 – 38.

Hunke, E. C. and Dukowicz, J. K. (1997). An Elastic–Viscous–Plastic Model for Sea Ice Dynamics. *Journal of Physical Oceanography*, 27(9):1849–1867.

Ingram, R. G. and Larouche, P. (1987). Variability of an under-ice river plume in Hudson Bay. *Journal Of Geophysical Research*, pages 9541 – 9547.

Ingram, R. G. and Prinsenberg, S. (1998). *Coastal Oceanography of Hudson Bay and Surrounding Eastern Canadian Arctic Waters Coastal Segment*, volume 11, pages 835–861. John Wiley and Sons, Toronto.

Joly, S., Senneville, S., Caya, D., and Saucier, F. (2011). Sensitivity of Hudson Bay sea ice and ocean climate to atmospheric temperature forcing. *Climate Dynamics*, 36(9/10):1835–1849.

Jones, E. P. and Anderson, L. G. (1994). Northern Hudson Bay and Foxe Basin: Water masses, circulation and productivity. *Atmosphere-Ocean*, 32(2):361–374.

Kirillov, S., Babb, D., Dmitrenko, I., Landy, J., Lukovich, J., Ehn, J., Sydor, K., Barber, D., and Stroeve, J. (2020). Atmospheric Forcing Drives the Winter Sea Ice Thickness Asymmetry of Hudson Bay. *Journal of Geophysical Research: Oceans*, 125(2).

Kowal, S., Gough, W. A., and Butler, K. (2017). Temporal evolution of Hudson Bay Sea Ice (1971–2011). *Theoretical and Applied Climatology*, 127(3):753–760.

Landy, J. C., Ehn, J. K., Babb, D. G., Thériault, N., and Barber, D. G. (2017). Sea ice thickness in the Eastern Canadian Arctic: Hudson Bay Complex & Baffin Bay. *Remote Sensing of Environment*, 200(Supplement C):281 – 294.

Large, W. and Yeager, S. (2004). Diurnal to Decadal Global Forcing For Ocean and Sea-Ice Models: The Data Sets and Flux Climatologies. NCAR/TN-460+STR NCARr technical note, National Center for Atmospheric Research.

Lavergne, T., Eastwood, S., Teffah, Z., Schyberg, H., and Breivik, L.-A. (2015). Sea ice motion from low-resolution satellite sensors: An alternative method and its validation in the Arctic. *Journal of Geophysical Research: Oceans*, 115(C10).

Lazier, J., Hendry, R., Clarke, A., Yashayaev, I., and Rhines, P. (2002). Convection and restratification in the Labrador Sea, 1990–2000. *Deep Sea Research Part I: Oceanographic Research Papers*, 49(10):1819 – 1835.

LeBlond, P. H., Osborn, T., Hodgins, D., Goodman, R., and Metge, M. (1981). Surface Circulation in the Western Labrador Sea. *Deep Sea Research Part A. Oceanographic Research Papers*, 28(7):683 – 693.

Lindström, G., Pers, C., Rosberg, J., Strömqvist, J., and Arheimer, B. (2010). Development and testing of the HYPE (Hydrological Predictions for the Environment) water quality model for different spatial scales. *Hydrology Research*, 41(3-4):295–319.

Lique, C., Treguier, A. M., Blanke, B., and Grima, N. (2010). On the origins of water

masses exported along both sides of Greenland: A Lagrangian model analysis. *Journal of Geophysical Research: Oceans*, 115(C5).

Lozier, M. S., Li, F., Bacon, S., Bahr, F., Bower, A. S., Cunningham, S. A., de Jong, M. F., de Steur, L., deYoung, B., Fischer, J., Gary, S. F., Greenan, B. J. W., Holliday, N. P., Houk, A., Houpert, L., Inall, M. E., Johns, W. E., Johnson, H. L., Johnson, C., Karstensen, J., Koman, G., Le Bras, I. A., Lin, X., Mackay, N., Marshall, D. P., Mercier, H., Oltmanns, M., Pickart, R. S., Ramsey, A. L., Rayner, D., Straneo, F., Thierry, V., Torres, D. J., Williams, R. G., Wilson, C., Yang, J., Yashayaev, I., and Zhao, J. (2019). A sea change in our view of overturning in the subpolar North Atlantic. *Science*, 363(6426):516–521.

MacDonald, M. K., Stadnyk, T. A., Déry, S. J., Braun, M., Gustafsson, D., Isberg, K., and Arheimer, B. (2018). Impacts of 1.5 and 2.0°C Warming on Pan-Arctic River Discharge Into the Hudson Bay Complex Through 2070. *Geophysical Research Letters*, 0(0).

Madec, G., Delécluse, P., Imbard, M., and Lévy, C. (1998). OPA 8.1 Ocean General Circulation Model reference manual. *Note du Pole de Modélisation*, 11:91p.

Madec, G. and the NEMO team (2008). NEMO ocean engine. *Note du Pole de Modélisation*, (No 27 ISSN No 1288-1619).

Masina, S., Storto, A., Ferry, N., Valdivieso, M., Haines, K., Balmaseda, M., Zuo, H., Drevillon, M., and Parent, L. (2015). An ensemble of eddy-permitting global ocean reanalyses from the MyOcean project. *Climate Dynamics*, pages 1–29.

McClelland, J. W., Dery, S. J., Peterson, B. J., Holmes, R. M., and Wood, E. F. (2006). A pan-arctic evaluation of changes in river discharge during the latter half of the 20th century.

McGovern, P. and Gough, W. (2015). East-West Asymmetry in Coastal Temperatures of Hudson Bay as a Proxy for Sea Ice. *Arctic*, 68(4):445–452.

Mesinger, F., Arakawa, A., and Global Atmospheric Research Programme, G. (1976). *Numerical Methods Used in Atmospheric Model*, volume 17 of *GARP publications series*. Global Atmospheric Research Programme, GARP.

Müller, V., Kieke, D., Myers, P. G., Pennelly, C., and Mertens, C. (2017). Temperature flux carried by individual eddies across 47°N in the Atlantic Ocean. *Journal of Geophysical Research: Oceans*.

Murray, R. (1996). Explicit generation of orthogonal grids for ocean models. *Journal of Computational Physics*, (2):251.

Murty, T. S. and Yuen, K. B. (1973). Balanced Versus Geostrophic Wind-Stress for Hudson Bay. *Journal of the Fisheries Research Board of Canada*, 30(1):53–62.

Myers, R. A., Akenhead, S. A., and Drinkwater, K. (1990). The influence of Hudson Bay runoff and ice–melt on the salinity of the inner Newfoundland Shelf. *Atmosphere-Ocean*, 28(2):241–256.

Pett, R., Roff, J., and I.P., M. (1982). Some observations and deductions concerning the deep waters of Hudson Bay. *Naturaliste Canadien*, pages 767 – 774.

Prinsenberg, S. (1984). Freshwater contents and heat budgets of James Bay and Hudson Bay. *Continental Shelf Research*, 3(2):191 – 200.

Prinsenberg, S. (1986a). Chapter 10 The Circulation Pattern and Current Structure of Hudson Bay. *Elsevier Oceanography Series*, 44:187 – 204.

Prinsenberg, S. (1986c). Chapter 12 On the Physical Oceanography of Foxe Basin. *Elsevier Oceanography Series*, 44(Canadian Inland Seas):217–236.

Prinsenberg, S. (1986e). Chapter 9 Salinity and Temperature Distributions of Hudson Bay and James Bay. *Elsevier Oceanography Series*, 44:163 – 186.

Prinsenberg, S. (1988). Ice-Cover and Ice-Ridge Contributions to the Freshwater Contents of Hudson Bay and Foxe Basin. *Arctic*, 41(1):6–11.

Rawlins, M. A., Steele, M., Holland, M. M., Adam, J. C., Cherry, J. E., Francis, J. A., Groisman, P. Y., Hinzman, L. D., Huntington, T. G., Kane, D. L., Kimball, J. S., Kwok, R., Lammers, R. B., Lee, C. M., Lettenmaier, D. P., McDonald, K. C., Podest, E., Pundsack, J. W., Rudels, B., Serreze, M. C., Shiklomanov, A., Øystein Skagseth, Troy, T. J.,

Vörösmarty, C. J., Wensnahan, M., Wood, E. F., Woodgate, R., Yang, D., Zhang, K., and Zhang, T. (2010). Analysis of the arctic system for freshwater cycle intensification: Observations and expectations. *Journal of Climate*, 23(21):5715–5737.

Reynolds, R. W., Smith, T. M., Liu, C., Chelton, D. B., Casey, K. S., and Schlax, M. G. (2007). Daily High-Resolution-Blended Analyses for Sea Surface Temperature. *Journal of Climate*, 20(22):5473–5496.

Ridenour, N. A., Hu, X., Jafarikhasragh, S., Landy, J. C., Lukovich, J. V., Stadnyk, T. A., Sydor, K., Myers, P. G., and Barber, D. G. (2019a). Sensitivity of freshwater dynamics to ocean model resolution and river discharge forcing in the Hudson Bay Complex. *Journal of Marine Systems*, 196:48 – 64.

Ridenour, N. A., Hu, X., Sydor, K., Myers, P. G., and Barber, D. G. (2019b). Revisiting the Circulation of Hudson Bay: Evidence for a Seasonal Pattern. *Geophysical Research Letters*, 46(7):3891–3899.

Robert, A. J. (1966). The Integration of a Low Order Spectral Form of the Primitive Meteorological Equations. *Journal of the Meteorological Society of Japan. Ser. II*, 44(5):237–245.

Roberts, J. L., Heil, P., Murray, R. J., Holloway, D. S., and Bindoff, N. L. (2006). Pole relocation for an orthogonal grid: An analytic method. *Ocean Modelling*, 12(1/2):16 – 31.

Roullet, G. and Madec, G. (2000). Salt conservation, free surface, and varying levels; a new formulation for ocean general circulation models. *Journal of Geophysical Research*, 105(C10):23.

Sadler, H. E. (1982). Water flow into Foxe Basin through Fury and Hecla Strait. *Naturaliste Canadien*, pages 701 – 707.

Saucier, F. and Dionne, J. (1998). A 3-D coupled ice-ocean model applied to Hudson Bay, Canada: The seasonal cycle and time-dependent climate response to atmospheric forcing and runoff. *Journal of Geophysical Research: Oceans*, 103(C12):27689–27705.

Saucier, F. J., Senneville, S., Prinsenberg, S., Roy, F., Smith, G., Gachon, P., Caya, D., and

Laprise, R. (2004). Modelling the sea ice-ocean seasonal cycle in Hudson Bay, Foxe Basin and Hudson Strait, Canada. *Climate Dynamics*, 23(3/4):303–326.

Semtner, A. (1976). A model for the thermodynamic growth of sea ice in numerical investigations of climate. *Journal of Physical Oceanography*, pages 379 – 389.

Shiklomanov, I. A. and Shiklomanov, A. I. (2003). Climatic Change and the Dynamics of River Runoff into the Arctic Ocean. *Water Resources*, 30(6):593–601.

Smith, G. C., Roy, F., Mann, P., Dupont, F., Brasnett, B., Lemieux, J.-F., Laroche, S., and Bélair, S. (2014). A new atmospheric dataset for forcing ice–ocean models: Evaluation of reforecasts using the Canadian global deterministic prediction system. *Quarterly Journal of the Royal Meteorological Society*, 140(680):881–894.

Spreen, G., Kaleschke, L., and Heygster, G. (2008). Sea ice remote sensing using AMSR-E 89-GHz channels. *Journal of Geophysical Research: Oceans*, 113(C2). C02S03.

St-Laurent, P., Straneo, F., and Barber, D. G. (2012). A conceptual model of an Arctic sea. *Journal of Geophysical Research: Oceans*, 117(C6). C06010.

St-Laurent, P., Straneo, F., Dumais, J.-F., and Barber, D. (2011). What is the fate of the river waters of Hudson Bay?. *Journal of Marine Systems*, 88(The Hudson Bay System):352–361.

Stadnyk, T., MacDonald, M., Tefs, A., Déry, S., Koenig, K., Gustafsson, D., Isberg, K., and Arheimer, B. (2020). Hydrological modeling of freshwater discharge into Hudson Bay using HYPE. *Elementa Science of the Anthropocene*, 8(1).

Steele, M. and Ermold, W. (2007). Steric Sea Level Change in the Northern Seas. *Journal of Climate*, 20(3):403–417.

Straneo, F. (2006). Heat and Freshwater Transport through the Central Labrador Sea. *Journal of Physical Oceanography*, 36(4):606–628.

Straneo, F. and Saucier, F. (2008a). The outflow from Hudson Strait and its contribution to the Labrador Current. *Deep Sea Research Part I: Oceanographic Research Papers*, 55(8):926 – 946.

Straneo, F. and Saucier, F. J. (2008b). *The Arctic–Subarctic Exchange Through Hudson Strait*, pages 249–261. Springer Netherlands, Dordrecht.

Stull, R. B. (1988). *An Introduction to Boundary Layer Meteorology.* Dordrecht: Kluwer Academic Publishers.

Sutcliffe Jr., W. H., Loucks, R. H., Drinkwater, K. F., and Coote, A. R. (1983). Nutrient Flux onto the Labrador Shelf from Hudson Strait and its Biological Consequences. *Canadian Journal of Fisheries and Aquatic Sciences*, 40(10):1692–1701.

Sutherland, D. A., Straneo, F., Lentz, S. J., and Saint-Laurent, P. (2011). Observations of fresh, anticyclonic eddies in the Hudson Strait outflow. *Journal of Marine Systems*, 88(The Hudson Bay System):375–384.

Tao, R. and Myers, P. (to be submitted). Modelling the Advection of Pollutants in the Hudson Bay Complex. *Journal of Marine Systems.*

Thorndike, A. S. (1986). *Kinematics of Sea Ice*, pages 489–549. Springer US, Boston, MA.

Wang, F. and Zhang, J. (2013). Mercury contamination in aquatic ecosystems under a changing environment: Implications for the Three Gorges Reservoir. *Chinese Science Bulletin*, 58(2):141–149.

Wang, J., Mysak, L., and Ingram, R. (1994a). A numerical-simulation of sea-ice cover in Hudson Bay. *Journal of Physical Oceanography*, 24(12):2515 – 2533.

Wang, J., Mysak, L. A., and Ingram, R. G. (1994b). Interannual variability of sea–ice cover in Hudson Bay, Baffin Bay and the Labrador Sea. *Atmosphere-Ocean*, 32(2):421–447.

Wang, J., Mysak, L. A., and Ingram, R. G. (1994c). A Three-Dimensional Numerical Simulation of Hudson Bay Summer Ocean Circulation: Topographic Gyres, Separations, and Coastal Jets. *Journal of Physical Oceanography*, 24(12):2496–2514.

Yang, J. (2006). The Seasonal Variability of the Arctic Ocean Ekman Transport and Its Role in the Mixed Layer Heat and Salt Fluxes. *Journal of Climate*, 19(20):5366–5387.

Zhang, X., He, J., Zhang, J., Polyakov, I., Gerdes, R., Inoue, J., and Wu, P. (2012). Enhanced poleward moisture transport and amplified northern high-latitude wetting trend. *Nature Climate Change*, 3(1):47 – 51.